Modeling the Mechanical Behavior of Amorphous Metals by Shear Transformation Zone Dynamics

by

Eric R. Homer

B.S. Mechanical Engineering
Brigham Young University, 2006

M.S. Mechanical Engineering
Brigham Young University, 2006

SUBMITTED TO THE DEPARTMENT OF MATERIALS SCIENCE & ENGINEERING IN PARTIAL FULFILLMENT OF THE REQUIREMENTS FOR THE DEGREE OF

DOCTOR OF PHILOSOPHY IN MATERIALS SCIENCE & ENGINEERING
AT THE
MASSACHUSETTS INSTITUTE OF TECHNOLOGY

JUNE 2010

Signature of Author: _____
Department of Materials Science & Engineering
May 17, 2010

Certified by: _____
Christopher A. Schuh
Danae and Vasilios Salapatas Associate Professor of Materials Science & Engineering
Thesis Supervisor

Accepted by: _____
Christine Ortiz
Associate Professor of Materials Science and Engineering
Chair, Department Committee on Graduate Students

Modeling the Mechanical Behavior of Amorphous Metals by Shear Transformation Zone Dynamics

by

Eric R. Homer

Submitted to the Department of Materials Science & Engineering
on May 17, 2010 in Partial Fulfillment of the Requirements
for the Degree of Doctor of Philosophy in
Materials Science & Engineering

ABSTRACT

A new mesoscale modeling technique for the thermo-mechanical behavior of amorphous metals is proposed. The modeling framework considers the shear transformation zone (STZ) as the fundamental unit of deformation, and coarse-grains an amorphous collection of atoms into an ensemble of STZs on a mesh. By employing finite element analysis and a kinetic Monte Carlo algorithm, the modeling technique is capable of simulating processing and deformation on time and length scales relevant to those used for experimental testing of an amorphous metal. The framework is developed in two and three dimensions and validated in both cases over a range of temperatures and stresses. The model is shown to capture the basic behaviors of amorphous metals, including high-temperature homogeneous flow following the expected constitutive law, and low-temperature strain localization into shear bands. Construction of deformation maps from the response of models, in both two and three dimensions, match well with the experimental behaviors of amorphous metals. Examination of the trends between STZ activations elucidates some important spatio-temporal correlations which are shown to be the cause of the different macroscopic modes of deformation. The value of the mesoscale modeling framework is also shown in two specific applications to investigate phenomena observed in amorphous metals. First, simulated nanoindentation is used to explore the recently revealed phenomenon of nanoscale cyclic strengthening, in order to provide insight into the mechanisms behind the strengthening. Second, a detailed investigation of shear localization provides insight into the nucleation and propagation of a shear band in an amorphous metal. Given these applications and the broad range of conditions over which the model captures the expected behaviors, this modeling framework is anticipated to be a valuable tool in the study of amorphous metals.

Thesis Supervisor: Christopher A. Schuh

Title: Danae and Vasilios Salapatas Associate Professor of Materials Science & Engineering

Table of Contents

List of Figures

List of Tables

1. Mechanical behavior of a metallic glass

1.1. Introduction

While amorphous materials have existed for a long time, amorphous metals, also known as metallic glasses, were discovered about a half-century ago by Klement et al., who rapidly quenched a mixture of gold and silicon to form an alloy with amorphous structure [1]. This rapid quenching caused the melt to kinetically bypass crystallization through limited atomic mobility, thereby freezing the system into a meta-stable configuration with no long range order. Since this time, the formability of metallic glasses has been improved through complex alloying compositions to form larger samples or bulk metallic glasses (BMGs) at slower cooling rates [2, 3]. BMGs have sparked scientific interest for many reasons, but a significant portion of this interest originates from the impressive suite of mechanical properties they possess [4].

For example, BMGs often exhibit yield strengths and elastic limits in excess of their polycrystalline counter-parts of similar composition, as illustrated in Figure 1.1. These properties, among others, would suggest that metallic glasses might be good candidates for use as structural materials, but at ambient temperatures they exhibit very little plasticity before failure through shear localization [5, 6]. While this poor ductility precludes their immediate application as a structural material, their high temperature response, which is homogeneous in nature, suggests the possibility of using BMGs in certain shape-forming operations.

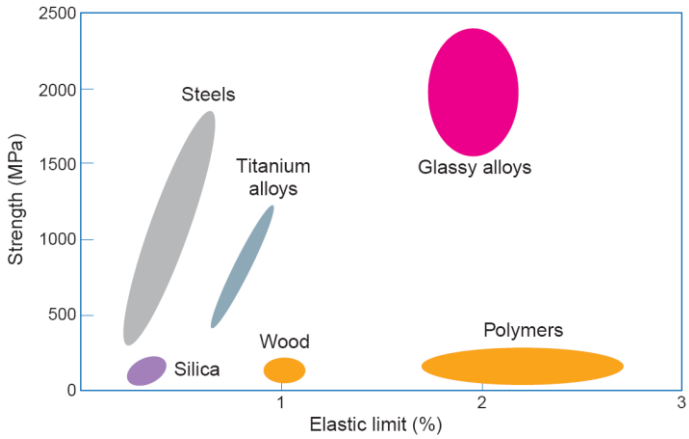

Figure 1.1 Ashby plot comparing several materials classes

The range of strength and elastic limit for several materials classes are compared where glassy alloys, or metallic glasses, exceed the properties of other structural metals. Figure taken from [4].

1.2. Deformation Mechanisms

Central to understanding the diverse modes of deformation observed in amorphous metals are the microstructural mechanisms whose collective action yield the responses measured on a macroscopic level. In spite of the large body of literature devoted to studying metallic glasses, no single unifying theory or microscopic mechanism has been identified and confirmed to be 'the' unit of deformation [7, 8]. In contrast, polycrystalline materials benefit from the well established theory of dislocation motion to describe atomic behavior, a theory which becomes useless in BMGs where no long range order exists. This lack of long range order makes it difficult to define a unique unit process across an extensive range of metallic glass alloying compositions where local environments can vary significantly. The difficulty in identifying a unit process is magnified by the fact that the nature of metallic bonding allows bonds to be so easily broken and reformed.

Although the exact nature of the microscopic mechanisms that lead to deformation in metallic glasses are not known, two proposed mechanisms have received general acceptance as suitable pictures of the atomic motion. The first is known as the shear transformation zone (STZ) of Argon [9] where several dozen atoms deform inelastically in response to an applied shear stress, which is illustrated in Figure 1.2(a). The second mechanism involves the redistribution of free volume as proposed by Spaepen [10] where a single atom jumps from an area of low free volume

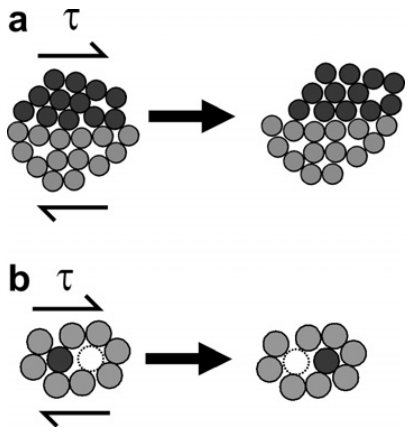

Figure 1.2 Microscopic mechanisms for deformation in a metallic glass
Schematic of mechanisms proposed by (a) Argon, where atoms shear inelastically in response to an applied shear, and (b) Spaepen, where an atom jumps from an area of low free volume to an area of higher free volume. Figure taken from [7].

to an area of higher free volume, as illustrated in Figure 1.2(b). Both of these events are viewed as stress-biased, thermally activated events, permitting simple rate laws for activation to be written in terms of state variables, including stress, temperature, and local structural order parameters such as free volume. To give an adequate description of each, both of these mechanisms are discussed in more detail in the paragraphs that follow.

Argon originally proposed the STZ after observing collective motion in amorphous bubble-raft experiments which were placed under shear [11]. This initial model proposed a high temperature STZ mechanism where the shear was accommodated in a more diffuse fashion over several dozen atoms, while a low temperature STZ mechanism would operate by concentrating the shear into a small disc which can be imagined to include only the atoms which touch and are of differing color in Figure 1.2(a) [9, 12]. Although the high and low temperature mechanisms were proposed differently, later work by Argon, and Bulatov, employed the high temperature mechanism to model and simulate deformation at both low and high temperatures [13-15]. In general, STZs have been modeled and expected to behave much like the diffuse high temperature mechanism where the shear strain is uniformly applied to the STZ, with typical values of the shear strain of ~10% [7, 13].

As a result of the elusive nature of the STZ, the measurement of the volume of an STZ has proven difficult. In one case however, researchers fitted data from several different studies in order to come up with STZ volumes in the range from 0.5-3.7 nm^3 [16]. These STZ volumes are in line with that predicted and observed by Argon [11, 12], and others [17]. An important distinction of the STZ, however, is that it is not a permanent feature of any glass structure, which stands in stark contrast to easily identifiable dislocations in a crystalline material. STZs are in fact a transient event which can only be observed by comparing atomic positions before and after microscopic deformation. This transient property of STZs makes it difficult to confirm their existence because in almost all cases, imaging at atomic length-scales typically precludes in-situ measurement, thus preventing a before and after atomic picture of microscopic behavior.

Argon's model of the STZ is treated in the context of an Eshelby inclusion problem [18]. In fact, Argon used the Eshelby solution to determine part of the activation energy barrier for an STZ to move from the unsheared state to the sheared state [9, 12], as illustrated in Figure 1.2(a). In the Eshelby solution, an STZ undergoes a stress-free strain transformation, after which both the STZ

and surrounding matrix are forced to elastically accommodate the transformation strain. The entire activation energy barrier for this event, as determined by Argon [9, 12], is

$$\Delta F = \left[\frac{7-5\nu}{30(1-\nu)} - \frac{2(1+\nu)}{9(1-\nu)}\beta^2 + \frac{1}{2\gamma_o} \cdot \frac{\hat{\tau}}{\mu(T)} \right] \cdot \mu(T) \cdot \gamma_o^2 \cdot \Omega_o . \qquad (1.1)$$

where the first term in the solution represents the strain energy of an STZ sheared by the characteristic shear strain, γ_o (~0.1). The second term represents the strain energy for a temporary dilatation to allow the atoms to rearrange into the sheared position where β (~1) represents the ratio of STZ dilatation during transformation to the characteristic shear strain γ_o. The third term represents the energy required to freely shear an STZ, with $\hat{\tau}$ equal to the peak interatomic shear resistance between atoms. The material properties ν and $\mu(T)$ represent Poisson's ratio and the temperature-dependent shear modulus, respectively, of both the STZ and surrounding matrix. Finally, the STZ volume is given by Ω_o with the product $\gamma_o \cdot \Omega_o$ equal to the activation volume of the STZ.

A contrast to the STZ picture of deformation in metallic glasses is Spaepen's model which describes deformation in terms of the redistribution of free volume in the glass through atomic jumps [10]. Spaepen's model is an application of the "free volume" model of Turnbull and Cohen [19, 20] and provides a convenient way to incorporate free volume as a state variable [21] to define the deformation behavior of a glass. While the derivation proved useful in developing a deformation map for metallic glasses, a single atomic jump cannot relax local shear stress. Furthermore, as will be discussed in section 1.4, atomistic simulations observe the concurrent and collective motions of several dozen atoms, not successive atomic jumps. For these reasons, the author prefers the use of the STZ model to represent the microscopic motion of a metallic glass.

In either case, both of these microscopic deformation mechanisms are two-state models with associated rate laws and provide a convenient simplistic picture of deformation. Thus, while the exact picture of atomic motion is not resolved, these two generally accepted microscopic mechanisms can be used to describe a range of observed deformation behaviors in metallic glasses [7].

1.3. Deformation Behavior

The deformation behavior of metallic glasses, as alluded to previously, can be separated into a homogeneous response observed at high temperatures and an inhomogeneous response observed at low temperatures and high stresses. Because of the very different nature of these modes of deformation, they will be discussed separately.

At temperatures above approximately 80% of the glass transition temperature, or 0.8 T_g, glasses behave as super-cooled liquids and display homogeneous deformation that is Newtonian at low stresses, but becomes Non-Newtonian at higher stresses [22]. This response can be described in terms of the microscopic STZ mechanism if one assumes that STZs are activated independently of one another. This results from the fact that the thermal energy is sufficient to bias the random activation of STZs above any localization that might occur from localized internal stresses. A simple analytical solution to this situation exists, with the assumption of a two-state STZ that shears forward or backward to contribute to the overall shear deformation. In this case, the shear strain rate yields the following hyperbolic-sine stress dependent function

$$\dot{\gamma} = 2 \cdot \gamma_o \cdot \nu_o \cdot \exp\left(-\frac{\Delta F}{kT}\right) \cdot \sinh\left(\frac{\tau \cdot \gamma_o \cdot \Omega_0}{2kT}\right). \qquad (1.2)$$

This equation provides remarkably good agreement with experimental results shown in Figure 1.3 for data obtained by Lu et. al. over several decades of strain rates and stresses and a range of temperatures spanning the glass transition temperature [22]. In this figure, the data are plotted as points and the solid lines are fitted in a form similar to Equation 1.2. The fitting of these data

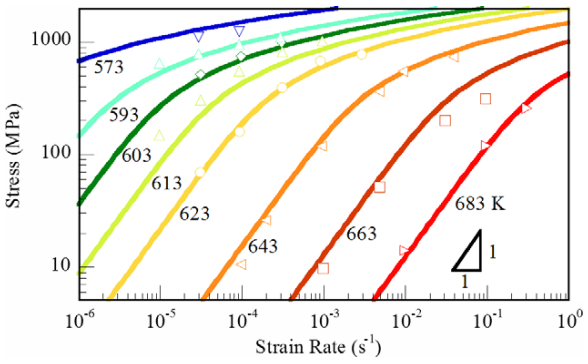

Figure 1.3 Rheological data for a metallic glass

Data taken from Lu et. al. [22] for the glass $Zr_{41.2}Ti_{13.8}Cu_{12.5}Ni_{10}Be_{22.5}$ deformed at various temperatures over several decades of strain rates and stresses. Figure taken from [7].

with Equation 1.2 are a convenient way to determine the activation energy and activation volume for STZ operations. In the case of this data for the glass $Zr_{41.2}Ti_{13.8}Cu_{12.5}Ni_{10}Be_{22.5}$ the activation volume was determined to be ~0.75 nm^3 and the activation energy was determined to be ~4.6 eV [7].

While the data from Lu et. al. [22] represent the steady-state response of a metallic glass to a given load, BMGs also exhibit a transient portion to a given applied loading or unloading condition. For example, when loading from an a unloaded state, a glass will often exhibit a peak stress where it deviates from elastic behavior and then "soften" or drop off to a lower stress where it reaches a steady-state strain rate [22].

BMGs, in most cases, behave very predictably when deformed at high temperatures; the more interesting behavior and considerable scientific interest lies in the low temperature regime where deformation is inhomogeneous in nature. This inhomogeneity stems from the fact that nearly all the plastic strain is localized into nano-scale "shear bands" that are only tens of nanometers in thickness [23, 24]. While thin, the shear bands can have offsets, also known as slip steps, that measure on the micrometer scale when the shear bands exit the material [25, 26]. Both of these features, the shear band thickness and slip steps, can be observed in Figure 1.4(a) where a BMG has been subjected to bending and the shear bands are clearly observable in the scanning electron microscope (SEM) micrograph [26].

While it is believed that STZs are still the fundamental unit of deformation at low temperatures [27], it is more difficult to attempt to postulate how these STZs interact to cause the observed localization. This again stems from the transient nature of the STZs and lack of long range order, which make it difficult to identify any microstructural changes resulting from the operation of a shear band. Current microscopy capabilities cannot provide the necessary techniques to image or track the flow in the highly localized shear band. In addition, mechanical testing methods don't have the resolution to capture shear band propagation. For example, in the nanoindentation of a BMG one will observe sudden accelerations of the indenter into the sample, called pop-ins, which are associated with the appearance of individual shear bands which surround the indentation [28]. These pop-ins appear in a single measurement step, meaning that the entire shear band forms and propagates faster than can be measured [28]. Additional studies confirm the formation of shear bands on timescales of 10^{-5}-10^{-3} s [5, 29]. Thus with the disparity

(a) 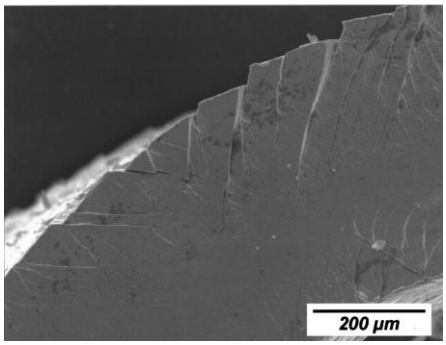

(b) 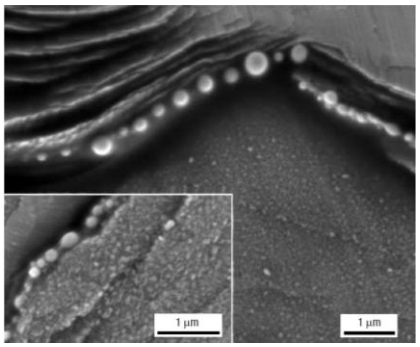

Figure 1.4 SEM micrographs of localization phenomena

Part (a) shows a BMG after bend test, illustrating the high degree of localization or shear banding that occurs in confined volumes, taken from [26] and part (b) shows beading of a tin coating on slip steps of shear bands indicating that the temperature rise present in shear band operations was sufficient to cause the coating to melt, taken from [30].

in the length-scales of the shear band width and slip step, and the appearance of a shear band on timescales below the resolution of the measurement tool, it is not currently possible to measure how shear bands nucleate or propagate. This unanswered question of localization remains one of the most important problems to be solved in order to understand the low-temperature mechanics of BMGs.

While the localization of shear bands is obviously affected by the local stresses and available thermal energy, numerous other factors can affect localization in BMGs as well. A study by Schuh et al. showed the effect of temperature and loading rate on the shear banding behavior in a metallic glass [31]. Their study showed that lower loading rates lead to a higher degree of flow serration than the higher loading rates, while higher temperatures produced more flow serration than low temperatures during the indentation tests. The reduction of the flow serration in both cases indicates a shift toward a higher density of shear bands that carry less plasticity [31]. So, while still inhomogeneous, this behavior trends toward a homogeneous region in the deformation map at low temperatures with little to no flow serration [31]. A pressure and normal-stress dependence have also been reported in metallic glasses [32, 33], indicating a possible need to modify the STZ model to incorporate the normal stress or pressure dependence of the local environment during STZ activation.

Another interesting behavior which has been observed in some BMGs is that during the propagation of a shear band, what is believed to be the internal friction between atoms can lead

to a rise in temperature of several hundred degrees. While simulated [34] and measured by other means [35], one study measured this temperature rise by coating the glass $Zr_{41.2}Ti_{13.8}Cu_{12.5}Ni_{10}Be_{22.5}$ with tin and observing that the tin beaded up on the slip steps of the shear bands following deformation. A micrograph of these tests can be seen in Figure 1.4(b), where the temperature rise was a minimum of 200 °C in order to melt the tin [30].

Also demonstrated in recent nanoindentation experiments is an apparent strengthening of a metallic glass at the nanoscale when cycled under spherical contact at very low loads [36]. This nanoscale strengthening contrasts the macroscopic behavior of a metallic glass where the elastic-viscoplastic nature of metallic glasses usually leads to softening of a glass under a load [7]. Of primary scientific interest in this case is the fact that the cyclic loading which leads to this strengthening occurs well below the load typically required to initiate a shear band. Furthermore, if the indenter were to be removed following the cyclic loading, no visible remnant of the cycling would be visible on the surface of the sample. Because this strengthening occurs in the regime corresponding to the elastic material response, it indicates that the strengthening must occur through some microscopic mechanism for plasticity which is not measureable by the current limitations of nanoindentation equipment [36].

All these different temperature, pressure, strengthening and heat evolution effects that alter the low temperature deformation behavior of a metallic glass are of fundamental scientific interest because each has a significant and very different effect on the nature of shear localization. Resolving the microscopic details of these behaviors is essential to their clear understanding and in properly characterizing the entire range of deformation behaviors observed in glasses.

1.4. Modeling and Simulating Deformation in Metallic Glasses

In an effort to better understand and predict the deformation behavior in metallic glasses, the scientific community has developed and applied a number of different modeling and simulation techniques. One of these methods, which was already mentioned and played a key role in the development of the STZ model, is the bubble raft experiments of Argon and coworkers [11, 37]. Argon created an amorphous raft of bubbles with two different bubble sizes atop a supporting solution, and then subjected the cell of bubbles to shear. By imaging these bubbles Argon was able to watch the individual bubble motions and used this information to develop his picture of the fundamental nature of the STZ. In his development of the STZ, Argon also developed

several analytical expressions to predict the different forms of observed behaviors in amorphous materials [9, 12].

Since this time numerous atomistic simulations have been developed to test a wide range of responses, conditions and properties of amorphous metals. One of the primary reasons for using atomistic simulations is that they provide exquisite tracking of individual atomic motions in order to properly study the microscopic mechanisms. In addition, no preconceived notion of the collective motion of the atoms is required; the simulation of atomic motion proceeds as determined by the model and the behavior can be analyzed subsequently. The development of accurate atomistic simulations is not easy, however, and much thought must be put into selecting the interatomic potentials, boundary and initial conditions, and step size of the simulations, among other important parameters, in order to provide a realistic outcome. The costs for being able to observe atomic motions are the limited length and time scales which are characteristic for atomic simulations. Simulation sizes vary widely, but don't usually exceed hundreds of nanometers, and with times that are typically around the nanosecond scale, strain rates are generally very high at 10^6-10^9 s^{-1} [38-40].

To date, the majority of atomistic simulations are performed on monoatomic glasses or binary alloys of glasses, many with very similar potential functions. This simplified structure is in stark contrast to the many complex BMGs that are studied experimentally. This is indicative of the difficulty in accurately and efficiently modeling the atomistic behavior of metallic glasses.

One of the major emphases in atomistic simulations has been on molecular statics or atomic interactions at zero-temperature, quasi-static conditions. This approach permits the study of the system as it moves through different states, always relaxing the atoms between each step to allow the system to reach an energy minimum. This removes all thermal energy from the system so that thermal fluctuations don't move the system between states. The reason this is advantageous is that one can study the structure of a glass as it moves through the different states driven by external conditions.

In these static simulations, small increments of strain are often imposed on the system in steps, with relaxations between each step. The system initially behaves in an elastic fashion with a linear relation between the stresses and the imposed strain. During some strain increments however, large drops in the stress are accompanied by significant changes in the glass structure

(a) 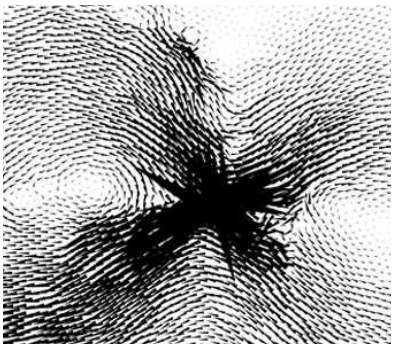 (b) 

Figure 1.5 Non-Affine displacement fields of atomic simulations

These displacement fields are associated with large stress drops in a statically strain atomic simulation, taken from [41]. (a) Displacement field similar to that expected from an individual STZ operation and (b) a displacement field for a less localized event spanning a larger distance.

[41]. When these stress drops are observed, two different trends are observed in the non-affine displacement fields of the atomic motions, as shown in Figure 1.5. First, rearrangements in atoms occur that are quadrupolar in nature [27, 41-44], which is what would be expected from the Eshelby solution [18] for a sheared STZ. The second trend which is observed is that in a single strain increment, a large number of atoms, usually spanning the entire simulation cell, will displace to form an elementary shear band with little to no indication of individual STZ operations [41].

In contrast to the zero-temperature simulations are finite temperature molecular dynamics (MD) simulations which incorporate thermal fluctuations to allow the system to access more states. These MD simulations are an important addition to the analysis techniques because they not only incorporate thermal fluctuations but can track elapsed time as well, allowing one to study the evolution of a system at finite temperatures on real time scales.

One MD study by Deng et al. focused on several features of the glass behavior including the melting, glass transition, structural relaxations, kinetics of structural relations and most importantly, plastic deformation via STZ-like operations [38, 45-47]. These STZ operations always lowered the free energy in the system regardless of the direction in which the atoms sheared, and in many cases retained a shear-induced dilatation [38]. These studies by Deng et al. are complimented by several other early studies where localized atomic motions are linked to measures of the stress distributions [48-51].

Falk and Langer saw similar STZ operations in an amorphous MD simulation deformed at low temperatures, and developed a theoretical model with state variables to aid in explaining the history dependence of loading in metallic glasses [21, 52]. By incorporating the local free volume as a state variable, Falk and Langer were able to show how the creation and destruction of free volume along with the activation of STZ operations can predict a wide range of phenomena observed in metallic glasses [21].

While many of the simulations discussed thus far focus on the microscopic mechanisms associated with metallic glass deformations, additional MD simulations have studied localization on larger scales through simulated nanoindentation [39, 53], as seen in Figure 1.6(a), and shearing of the simulation cell [41], among other techniques [54-57]. One nanoindentation study by Shi and Falk [53] shows the same type of rate dependence observed in experimental tests by Schuh et. al. [31]. While Shi and Falk observe the formation of the shear bands, their study focuses more on the changes in structure upon shear banding while providing little discussion on the path taken by different shear bands [53], although they do suggest that the path could be a percolating backbone of clusters of short-range order [58]. Simulations also indicate a change to the structure in the region where localization has occurred, or that the nature of the deformation changes based on the structure that results from solidification from the melt at different rates [39, 58, 59]. The pressure dependence of atomistic motions have also been shown to match the Mohr-Coulomb yield criterion [60], to which the failure criterion of metallic glasses conforms.

Over the past 30 years, the ability to perform faster and larger atomic simulations has increased, and a wealth of knowledge has been obtained. Yet, the exact fundamentals of the microscopic mechanisms of deformation in amorphous metals remain elusive, which is a testament to the difficulty of the problem to be solved, and indicates that different approaches may provide answers that atomic simulations aren't currently able to provide.

If one chooses to ignore atomistics altogether, one can treat the material as a continuum and thereby access significantly longer time and length scales. In this case, the material's mechanical behavior can be governed by constitutive relations that are designed to specifically model the deformation. While metallic glasses have an elastic-viscoplastic response, the localized nature of the plasticity at low temperatures precludes the use of typical constitutive metal plasticity models, requiring the derivation of a new constitutive model for metallic glasses. In any case,

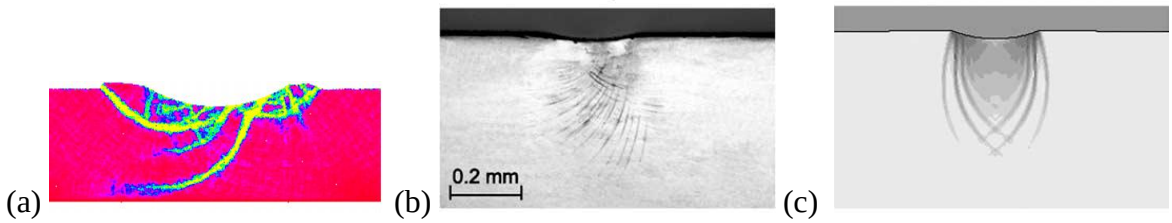

Figure 1.6 Comparison of simulated and experimental indentation

Results from (a) MD simulation of indentation in a metallic glass with high regions of localized strain highlighted, illustrating the shear bands, taken from [53]. (b) Micrograph and (c) continuum simulation of plane strain cylindrical indentation of a metallic glass, showing the resultant shear bands, taken from [61]

the implementation of any constitutive relation means that it can only model the behavior that it has been designed to capture. Thus, every time a new deformation behavior is to be captured, the constitutive equations must be altered or reworked to include the desired effect.

In spite of this, continuum simulations are able to accurately simulate the behavior of very large systems on experimental timescales. Some examples of these successful implementations are continuum simulations in which the material behavior has been modeled at low temperatures, in indentation [61, 62], at high temperatures [63, 64], in thermoplastic forming [64] and other applications [62, 65]. Other simulations even incorporate local structural changes to more accurately model the behavior [66, 67], or derive and apply constitutive laws for the local motions observed in atomic simulations [68-70]. Complementary constitutive-based phase-field models have also been employed to examine localization through the use of an order parameter to represent structural relaxation [71]. In the few cases where finite element results have been compared to experimental results, the simulated results show good agreement with the experimental data [61, 72]. This agreement is shown for indentation of a metallic glass where the experimental response, Figure 1.6(b), can be compared to the simulated response, Figure 1.6(c). Thus, while continuum simulations may miss the microscopic physics of deformation, they do have the advantage of simulating at time and length scales that would otherwise be unattainable through atomistics.

Another approach to modeling which is intermediate to atomistic and constitutive-based continuum simulations is a coarse-grained approach of mesoscale simulations. In this approach, one takes a characteristic event, such as an STZ, and uses this as the fundamental unit of

deformation. The reason that mesoscale models are so appealing is that they can resolve the time and length scales larger than atomistic modeling while still capturing the fundamental physics of deformation with the characteristic event, which constitutive based continuum simulations miss [8].

Bulatov and Argon performed simulations of this nature in the early nineties and observed good agreement with the expected modes of deformation of a metallic glass [13-15]. By creating a fixed lattice of potential STZs and using Green's function to solve the stress and strain distributions in the system they were able to calculate the rate of STZ activations. A kinetic Monte Carlo (KMC) algorithm was then used to determine which STZ to activate and to increment time in the simulation based on the current rate of STZ activation. In this manner, an ensemble of STZs was used to evolve a system on significant length and time scales. This approach observed both the homogeneous deformation at high temperature and inhomogeneous deformation at low temperatures solely by changing the temperature or thermal energy available to move between states [13]. In addition this model was used to study the kinetic behavior of the glass transition and structural relaxation that occurs during cooling [14]. Lastly, they studied the effects of structure on the plastic response of the system which leads to strain softening and other strain rate, pressure and temperature effects [15].

Lastly, numerous numerical models have also been developed to predict the macroscopic response of a material based on general conditions, and as such they cannot all be listed here. The most notable of these numerical models include the original STZ model by Argon [9, 12], the redistribution of free volume by Spaepen [10], the STZ model of Falk and Langer using free volume as a state variable [21], the cooperative shear model by Johnson [73, 74], and lastly, the two-state STZ dependent shear strain rate given in Equation 1.2. These have all been created to predict the response of the glass, given general state parameters and testing conditions. While many of these models accurately capture and predict some specific features of the mechanical behavior of metallic glasses, they only provide a general picture of the microscopic deformation, if at all, making it difficult to link the expected microscopic deformation to that observed on a macroscopic level.

1.5. Open areas of research in modeling

While a great deal of insight into the mechanical behavior of metallic glasses has been gained through the different modeling techniques described above, there is a significant lack in the capabilities of the methods described above. Specifically, none of the techniques preserve the fundamental physics of deformation at a microscopic level while modeling experimentally relevant conditions. Atomistics are too limited in their time and length scales and represent very driven systems, continuum simulations miss the fundamental physics of microscopic deformation and the current implementations of the mesoscale techniques, such as that by Bulatov and Argon [13], cannot explore the spatial evolution of deformation nor the complex loading conditions through which metallic glasses are actually tested. As such, the field is in need of a method with these capabilities.

A method with the capability to model experimentally relevant conditions that retains the fundamental mechanism for microscopic deformation would also allow the resolution of some important questions regarding the mesoscopic details of deformation in amorphous metals. For example, if the fundamental deformation mechanism in amorphous metals is the rearrangement of dozens or hundreds of atoms, as seen in atomistic simulations [41, 42, 44], how do these individual events interact to effect macroscopic deformation? What spatial and temporal correlations exist between these individual events? How are these correlations affected by the local environment (*e.g.* stress, temperature, free volume)? Do STZs interact at all at high temperatures where metallic glasses exhibit stable viscous flow and common constitutive laws assume independent STZ activation [7, 22]? More importantly, what sequence of events leads to shear localization, where the micrometer material displacements develop over millisecond time scales in the confined nanometer-sized shear bands [5, 23-26, 29]? Is this localization the result of cascades of correlated STZ activity or do smaller pockets of localized shear connect in a percolative fashion to form the shear bands [55, 58]?

Additionally, the application of a modeling framework with the ability to model the relevant time and length scales could provide significant insight into behaviors without a clear mechanistic understanding, such as the apparent nanoscale strengthening observed under cyclic nanoindentation [36]. Specifically, one could verify whether the conditions of the cycling in the

elastic regime are sufficient to induce local deformation immeasurable be current nanoindentation techniques, such that the glass could be strengthened.

Finally, proper connection with the experimental literature requires models that accurately capture the complexities of the experiments by which metallic glasses are actually tested. While three-dimensional models are better suited to account for the complexities of the experimental tests, their computational costs often limit their applications. This limited application is illustrated by the small number of studies which employ a fully three-dimensional (3D) framework in atomistics [53, 54, 56, 58, 59, 75] and continuum simulations [72, 76]. Yet, these 3D studies still have the same limitations discussed in section 1.4, and we are unaware of any mesoscale model for glass deformation in 3D. Therefore, a method which can access the appropriate time and length-scales and resolve the complexities of stress, strain and deformation in 3D would be extremely valuable in studying the mechanics of a glass under realistic conditions.

1.6. Layout of this thesis

As revealed in Section 1.5, there are a number of questions about the behavior of metallic glasses at the mesoscale that can be addressed uniquely with a new modeling technique based on the STZ and controlled through a kinetic Monte Carlo algorithm.

Chapter 2 addresses the development and validation of such a mesoscale model in two dimensions (2D) and then provides comparison of results of the technique with the behaviors observed in experimental testing of a metallic glass.

While chapter 2 focuses on the macroscopic model response, chapter 3 provides an in-depth analysis of the connection between the microscopic STZ activity and the macroscopic response of the system under different conditions. Specifically, this analysis details the energetics of the STZs selected through the KMC algorithm as well as the spatio-temporal correlations between STZ activations that lead to different modes of macroscopic deformation.

In chapter 4 the modeling framework is then applied to the phenomenon of nanoscale strengthening of a metallic glass under cyclic contact to provide insight into the mechanisms leading to the strengthening.

Finally, the modeling framework is extended to three dimensions in chapter 5 and the 3D framework is tested under experimentally relevant test conditions to once again validate the model against the observed behaviors of a metallic glass.

The thesis is then closed in chapter 6, with remarks on the modeling framework and its applications, along with recommendations for future work.

2. Development and validation of STZ Dynamics framework[1]

2.1. Introduction

As discussed in sections 1.4 and 1.5 a great deal of insight into the behavior of amorphous metals has been gained through a combined approach of different modeling techniques. However, the limitations of the atomistic and continuum techniques suggest that the addition of a mesoscale model may provide new insight into the mesoscopic details of deformation in a metallic glass.

The purpose of this chapter is to develop a new mesoscale modeling technique that we term "STZ Dynamics" modeling. In this approach, STZ activation is considered as a stochastic, stress-biased, thermally activated event which obeys a specific rate law, and the kinetic Monte Carlo algorithm is employed to control the evolution of the system. FEA is used to solve the elastic strain distribution in the system, by which the STZs communicate with one another. In this manner, we are able to access longer time and length scales than those associated with atomic motions. Our model takes its inspiration from the lattice model of Bulatov and Argon [13], but expands upon it in the sense that our use of FEA permits arbitrary shape changes, complex geometries and boundary conditions, greater freedom in the definition and activation of STZs, and a close connection to experimental conditions. This contrasts the model of Bulatov and Argon [13], where the fixed lattice and Green's functions limited the ability of their model to explore both the spatial evolution of the system and complex loading conditions. In this chapter, we present our basic methodology, and then proceed to develop a specific two-dimensional implementation as a demonstration of the method. We explore the thermal response and effects of processing, the rheological nature of deformation at high temperatures, and shear localization at low temperatures. Lastly, a compilation of data from many simulations is used to construct a deformation map for a model metallic glass.

2.2. Modeling Framework

2.2.1. Shear Transformation Zones

We model an amorphous material as an elastic continuum consisting of an ensemble of potential STZs defined on a mesh. In essence, we substitute a continuum mesh, shown schematically in Figure 2.1, for a collections of atoms, shown schematically in Figure 1.2(a). We treat the shearing of an STZ as an Eshelby inclusion problem [18], as proposed by Argon in his

[1] The contents of this chapter have been published previously as Ref. [77]

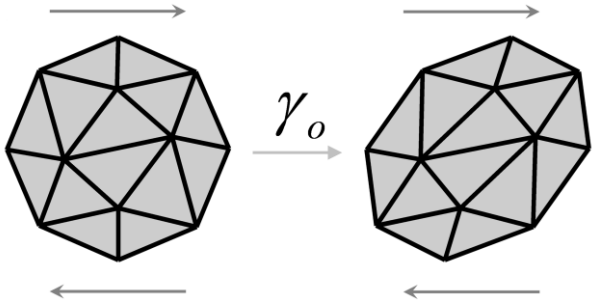

Figure 2.1 Schematic representation of finite element STZ
Shows the schematic motion of a finite element mesh associated with the atomic motions of an STZ.

calculation of the activation energy barrier for shearing of an STZ [9, 12]. In this approach, an STZ undergoes a stress-free strain transformation, after which both the STZ and surrounding matrix elastically accommodate the transformation strain. The activation energy barrier as determined by Argon [9, 12] is given in Eqn. 1.1, but for the purposes of these simulations, we choose to represent the intrinsic activation energy barrier solely as a function of the temperature-dependent shear modulus by combining all the other terms into a constant

$$\Delta F(T) = \Delta F_o \cdot \mu(T). \tag{2.1}$$

In our approach, the finite element mesh and the definition of the STZs on the mesh are selected with the following characteristics in mind:

- The geometrical shape of the STZ in the mesh should resemble that observed in simulations and models, roughly spherical in three dimensions or circular in two [9, 11, 17, 27, 60].
- Each individual STZ should be represented by a sufficient number of elements to accurately resolve the stress and strain distributions in the mesh.
- Elements that belong to one STZ should be able to participate in other potential STZs, just as atoms may participate in various different STZs.

One simple implementation that achieves these criteria in two dimensions is a triangular mesh with STZs bound to the nodes and elements of the mesh. For example, STZs may be centered on nodes of the mesh, and incorporate a number of surrounding elements extending radially outwards. This is illustrated in Figure 2.2(a) where 6, 24 and 54 element STZs are defined on a central node and include respectively, one, two and three elements extending radially outwards.

Alternatively, STZs may be centered on a single element and incorporate elements extending radially outwards. An example is shown in Figure 2.2(a) for a 13 element STZ extending one element radially outwards to include elements which share common nodes. The details of the STZ definition become important in the accuracy of stress and strain field calculations, and will be discussed in a later section. Finally, while in principle one might define an ensemble of STZs with different characteristic volumes, Ω_o, based on the local size of the elements included in each potential STZ, the simplest approach is to assign a single value of Ω_o to all the STZs in the mesh, as we shall do in the present implementation.

The last desired STZ characteristic that is satisfied by the STZs defined on the triangular mesh is that elements in the mesh will be able to participate in multiple STZs. Provided that STZs comprise more than a single element, this condition is naturally achieved, as illustrated in Figure

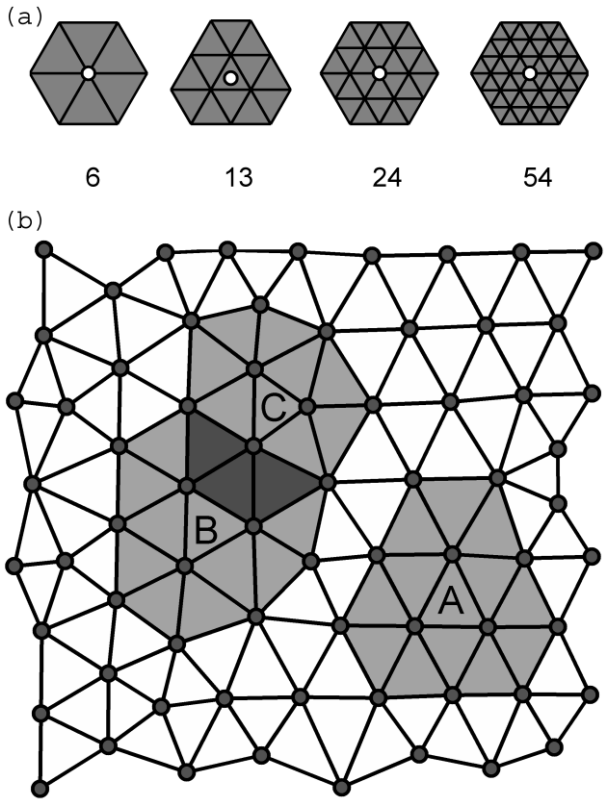

Figure 2.2 Representation of STZ defined on a finite element mesh
Part (a) shows several possible STZ definitions on a triangular lattice. Part (b) shows an irregular triangular mesh with 13-element potential STZs highlighted and denoted by A,B and C; B and C show how individual elements in the mesh can be activated by different STZs.

2.2(b), where 3 potential STZs, each of 13 elements, are highlighted on an irregular triangular mesh. At any given time step, the elements in the overlap region between potential STZs B and C can participate in either event (and others not shown).

2.2.2. Kinetic Monte Carlo

The activation rate law of a single potential STZ is given by

$$\dot{s} = \nu_o \cdot \exp\left(-\frac{\Delta F - \frac{1}{2}\tau \cdot \gamma_o \cdot \Omega_o}{kT} \right) \tag{2.2}$$

where $\dot{s}$ is the STZ activation rate, ΔF is the local energy given in Equation 2.1 for an STZ shearing in the fashion shown in Figure 2.1. The local shear stress and temperature are represented by τ and T, respectively. Boltzmann's constant is given by k and ν_o represents the attempt frequency along the reaction pathway, which is of the order of the Debye Frequency.

The activation rate defined in Equation 2.2, however, only gives the rate for an STZ attempting to shear in one direction. In two dimensions, the rate for an STZ attempting to shear in N different directions around a circle is given by

$$\dot{s} = \frac{\nu_o}{N} \cdot \sum_{n=1}^{N} \exp\left(-\frac{\Delta F - \frac{1}{2}\tau_{\max} \cdot \sin\left(\phi + 2\pi \frac{n}{N}\right) \cdot \gamma_o \cdot \Omega_0}{kT} \right) \tag{2.3}$$

where $\tau_{\max}$ is the maximum in-plane shear stress and ϕ is the angle to the current stress state in Mohr space for the given STZ. If Equation 2.3 is simplified and the discrete summation is converted to a continuous integral by letting N go to infinity, we have

$$\dot{s} = \frac{\nu_o}{2\pi} \cdot \exp\left(-\frac{\Delta F}{kT} \right) \cdot \int_0^{2\pi} \exp\left(\frac{\tau_{\max} \cdot \sin(\theta) \cdot \gamma_o \cdot \Omega_0}{2kT} \right) d\theta \tag{2.4}$$

which evaluates to a modified Bessel function of the first kind, of order zero

$$\dot{s} = \nu_o \cdot \exp\left(-\frac{\Delta F}{kT} \right) \cdot \mathrm{I}_0\left(\frac{\tau_{\max} \cdot \gamma_o \cdot \Omega_0}{2kT} \right). \tag{2.5}$$

Equations 2.4 and 2.5 integrate the value of the shear stress as we traverse the circle in Mohr space for the given value of the shear stress as defined by $\exp(\tau_{\max} \cdot \sin(\theta))$ for θ on the interval [0°, 360°). Thus, Equations 2.4 and 2.5 are able to determine the rate for shearing a single STZ in a continuum of directions around a circle, based upon the local stress and temperature of the

STZ. The form of Equation 2.5 is especially convenient for evaluating the integral computationally.

The kinetic Monte Carlo (KMC) algorithm [13, 78, 79] can be used to evolve an ensemble of STZs governed by Equations 2.1 and 2.5, where each STZ may experience a different local temperature and stress state, by repeating the following steps:

1. Calculate and form a list of activation rates, $\dot{s}_i$, for each of the i = 1…N STZs in the ensemble, based on the current state of the system.
2. Calculate the cumulative activation rate, $\dot{s}_T$, for all STZs and normalize each individual rate by $\dot{s}_T$,

   $$\eta_i = \dot{s}_i / \dot{s}_T \tag{2.6}$$

   such that

   $$\sum_i \eta_i = 1. \tag{2.7}$$

3. Generate two random numbers, ξ_1 and ξ_2, uniformly distributed on the interval [0,1).
4. Update the elapsed system time with the residence time for the current configuration calculated according to

   $$\Delta t = -\ln \xi_1 / \dot{s}_T \ . \tag{2.8}$$

5. Select a single STZ by first defining the cumulative fraction of STZ rates up to and including the rate of STZ *j* by

   $$\mathrm{H}_j = \sum_{i=1}^{j} \eta_i \ , \tag{2.9}$$

   and then using the random number, ξ_2, to find the STZ which satisfies

   $$\mathrm{H}_{k-1} < \xi_2 \le \mathrm{H}_k . \tag{2.10}$$

   When listed in a successive fashion, ξ_2 falls on the subinterval η_k in the list of normalized STZ rates, as illustrated in Figure 2.3(a).

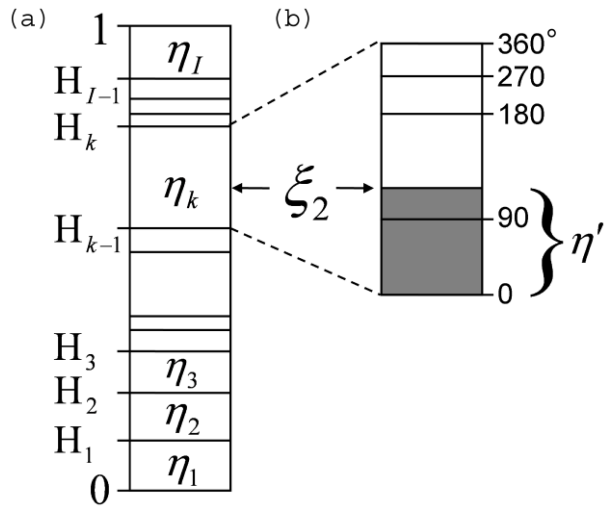

Figure 2.3 Schematic of the kinetic Monte Carlo STZ selection procedure
Part (a) shows how the random number ξ_2 can be used to select a single STZ for activation from a list of normalized individual STZ rates, $\eta_1, \eta_2, \eta_3 .. \eta_I$ and part (b) illustrates the determination of the overlap, η', between ξ_2 and η_j (as defined in Equation 2.11), which selects the angle of shear of the STZ.

6. To select the angle at which to shear the STZ, we first define the value η', which represents the magnitude by which ξ_2 overlaps the subinterval of the selected STZ, η_k, as illustrated in Figure 2.3(b),

$$\eta' = \xi_2 - \mathrm{H}_{k-1}. \tag{2.11}$$

The overlap, η', is then used to determine the integration limit which satisfies the equality

$$\eta' = \frac{1}{\dot{s}_k} \cdot \frac{\nu_o}{2\pi} \exp\left(-\frac{\Delta F}{kT}\right) \int_0^{\theta'} \exp\left(\frac{\tau_{\max} \cdot \sin(\theta) \cdot \gamma_o \cdot \Omega_0}{2kT}\right) d\theta . \tag{2.12}$$

7. The integration limit θ' from Equation 2.12 and the angle to the current stress state ϕ can then be used to define the angle of shear in real space, relative to a state of pure shear, by

$$\omega = (\phi - \theta')/2 . \tag{2.13}$$

8. Apply a shear shape distortion to the selected STZ of the form

$$\begin{bmatrix} \varepsilon_{11} \\ \varepsilon_{22} \\ \gamma_{12} \end{bmatrix} = \begin{bmatrix} \frac{1}{2}\gamma_o \sin(2\omega) \\ -\frac{1}{2}\gamma_o \sin(2\omega) \\ \gamma_o \cos(2\omega) \end{bmatrix} \tag{2.14}$$

and subsequently calculate the stress and strain distributions of the new configuration.

The KMC algorithm can be repeated for an arbitrary number of STZ operations and is efficient because every iteration guarantees a transition. The stochastic nature of the processes will produce a realistic outcome if the rates governing the individual events are correct.

While most of the steps listed above are standard to any KMC algorithm, steps five and six deserve further explanation. In the list of normalized STZ rates of Figure 2.3(a), some subintervals are larger than others, since some STZs experience higher stress than others. Strictly speaking, such STZs experience higher values of λ:

$$\lambda = \frac{\tau_{\max} \cdot \gamma_o \cdot \Omega_0}{2kT}, \tag{2.15}$$

which governs the STZ activation rate (cf. Equation 2.5) and dictates the width of the subinterval η_i. Thus, when selecting the STZ with the random number ξ_2, the larger subintervals have a higher probability of being selected, giving preference to events that occur on shorter time scales.

The value of λ also impacts the choice of the STZ shearing angle, as a result of the exponential dependence of λ in Equation 2.4. This is illustrated by the non-uniform subintervals in Figure 2.3(b). A more accurate representation of this effect can be seen by calculating the values of η' as determined for different ratios of λ where the integral Equation 2.12 is evaluated from 0 to θ' for a range of θ' on the interval [0°, 360°). The result is plotted as a function of the integration limit θ' in Figure 2.4(a), where the arrows on the plot point from smaller to larger values of λ (i.e., from states of lower stress/higher temperature to states of higher stress/lower temperature). It can be seen that for small values of λ the curve is linear, meaning that a random number will uniformly select the angle θ'; at high temperatures or low stress levels there is no preference for the shearing direction of the STZ. For large values of λ, however, the trend in Figure 2.4(a) is sigmoidal, and most randomly selected numbers will preferentially select shearing angles near 90°— the angle of maximum shear in Mohr space. Thus, at low temperatures and/or high stresses, the local stress state biases the STZ into shearing in the

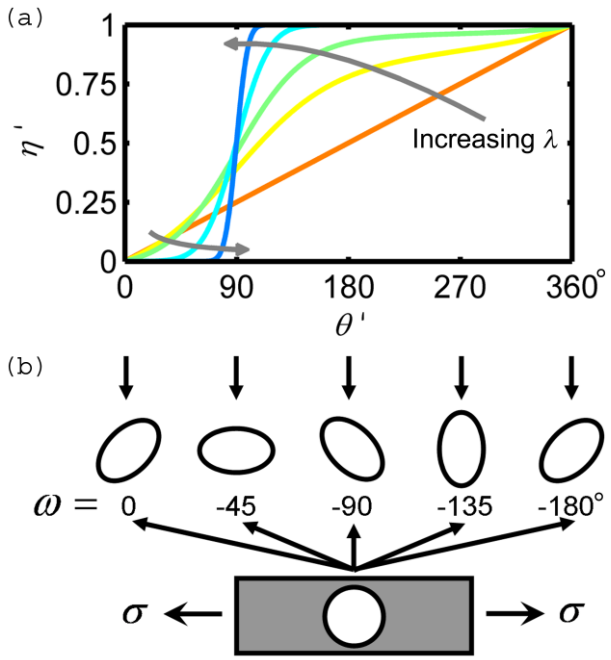

Figure 2.4 Representative selection of STZ shearing angle

Part (a) shows the evaluation of Equation 2.12 as a function of θ', in degrees, for several different values of λ. The arrows point from smaller to larger values of λ, illustrating the drive for the system to shear at the angle of maximum shear for large values of λ. Part (b) illustrates the shearing of an STZ for different values of ω for a state of pure tension, where the different STZs have been lined up under part (a) to illustrate how the value of λ influences the probability of observing each type of shear event.

direction of maximum shear. This is illustrated for the case of uniaxial tension in Figure 2.4(b), where $\omega = -\theta'/2$ because ϕ is zero. Several potential shear shape distortions are shown beneath Figure 2.4(a) to illustrate how the integration limits relate to each distortion. At very high values of λ the preferred shear shape distortion is in the direction of the uniaxial tension (shear at 45° to the tensile axis) providing maximum extension for a single STZ activation.

2.2.3. Finite Element Analysis

With an ensemble of STZs defined on the mesh and the KMC algorithm to evolve the system, there remains only the matter of identifying the local states of these potential STZs, i.e., the local stress and temperature that will govern their activation. In our model, FEA is used to determine the stress and strain distributions in the system at every KMC step. When an STZ is to be activated or sheared, an increment of strain, as given in Equation 2.14, can be applied to the

elements belonging to that STZ and the FEA solver can then recalculate the stress and strain distributions.

For all the simulations discussed in this paper, we employ the commercial finite element package ABAQUS as our FEA solver, with plane-strain quadratic triangular elements. We apply the STZ shearing strains through the use of ABAQUS User Subroutines, and since all plasticity occurs through these local STZ shape change events, we only require a linear elastic solver to determine the stress and strain fields. For simplicity in this paper, we require the entire system to have a uniform temperature distribution.

We explore the issue of mesh resolution by considering the shearing of a single STZ located in the center of a triangular mesh. The analysis is performed with eight different STZ definitions, seven centered on a node and including from one to seven elements along the STZ radius, as well as a 13 element STZ centered on an element; some of these STZ definitions are shown in Figure 2.2(a). In each of the eight cases, the STZ is sheared in a variety of different directions to obtain a measure of error on the calculation. As this situation closely resembles the Eshelby inclusion problem [9, 18], we use the analytical solution obtained by Eshelby for shearing of a circular long fiber in a matrix (plane strain) as a point of comparison. The percent error of the calculation relative to the Eshelby solution (based on the total system strain energy) is plotted in Figure 2.5 as a function of the size of the STZ relative to the mesh. As these data show, convergence is achieved quite quickly, with STZs containing 13 or more elements exhibiting

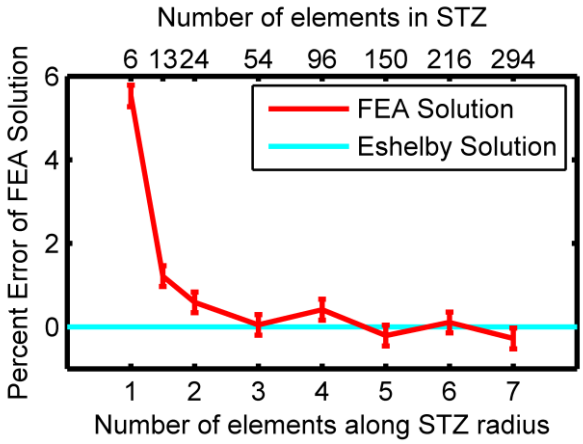

Figure 2.5 Convergence of FEA solution with refinement of mesh
Plot of the percent error between the strain energy determined by FEA methods and the Eshelby solution, as a function of the size of the STZ.

about 1.5% error or less. However, each time the number of elements along the STZ radius is doubled, it quadruples the number of elements required to simulate the same system size, and thus roughly quadruples the computational time; accordingly, we identify the 13 element STZ as a reasonable compromise between accuracy and computational speed. All the computations described in the remainder of this paper are carried out with 13-element STZs defined on an irregular triangular mesh, as schematically illustrated in Figure 2.2(b). For comparison, we also conducted many simulations using the 6-element STZs as well as a number of simulations involving a perfect triangular mesh, both of which give similar results in qualitative and quantitative sense.

It is important at this point to discuss mesh distortion that can occur through severe deformation, which leads to errors in the solutions of the stress and strain distributions. This problem can be circumvented by periodically checking for distortion of the mesh and remeshing if necessary, which requires mapping the elastic fields onto the new mesh. Solution mapping can contribute to error accumulation as well, so it is important to take care that the error accumulated by solution mapping is smaller than that accumulated by simply ignoring the mesh distortion. In this paper, we limit our discussion to cases in which the mesh distortion was sufficiently low that there is no concern about the solution accuracy. However, remeshing is, in general, an important aspect of our modeling approach, especially for situations involving localization.

2.2.4. Material Properties

Our model requires several material properties including Poisson's ratio, ν, and the temperature dependent shear modulus, $\mu(T)$ which is defined relative to its value, μ_o, at T = 0 K as

$$\mu(T) = \mu_o + \frac{d\mu}{dT} T \,. \tag{2.16}$$

For the sake of simplicity, we neglect the abrupt changes in modulus which are experimentally observed near the glass transition temperature, and assume the linear relationship above to be valid over the range of temperatures considered in this paper. The Debye temperature, θ_D, of the material, which is related to the Debye frequency, is required for the rate calculations. Finally, two geometrical properties of the STZs are required; the STZ volume Ω_o and the number of atoms in that volume based upon the material chemistry. In this paper we have used material properties derived from experiments on Vitreloy 1, $Zr_{41.2}Ti_{13.8}Cu_{12.5}Ni_{10}Be_{22.5}$, as listed in Table

Table 1 List of material properties for Vitreloy 1, $Zr_{41.2}Ti_{13.8}Cu_{12.5}Ni_{10}Be_{22.5}$

Property	Value	Reference
μ_o	$37\,[\mathrm{GPa}]$	[80]
$d\mu/dT$	$-4.0\times10^{-3}\,[\mathrm{GPa/K}]$	[80]
ν	0.352	[80]
θ_D	$327\,[\mathrm{K}]$	[81]
Ω_o	$1.6\,[\mathrm{nm}^3]$	Adjusted from [16]
ΔF_o	$1.175\times10^{-29}\,[\mathrm{J/Pa}]$	

1. In addition, we take the value of $\hat{\tau}$, from Equation 2.1, to be equal to the athermal shear stress.

2.3. Model Output

To demonstrate the ability of this modeling framework to simulate the wide range of behaviors exhibited by glasses, we perform a series of simulations on a plane strain 2-D irregular triangular mesh based on 13-element STZs. Using the material properties from Table I, this domain has approximate dimensions of 34.8 nm wide by 57.7 nm tall. In all cases the mesh is subjected to boundary conditions in which top and bottom surfaces are constrained in the y-direction and the bottom left node is fixed.

In order to implement the framework in a computationally efficient manner, we have integrated several different software packages and coding languages. MATLAB is used as a wrapper to control and call the different packages and processes; MySQL is used for efficient data storage and data recall; Python is used to interact with ABAQUS CAE; Fortran is used to code the User Subroutines in ABAQUS; and C++ is used to post process the ABAQUS output files. Finally, the parallel processing capabilities of ABAQUS are employed to reduce the computation time of the simulations.

2.3.1. Thermal Response and Processing

We begin by first studying the effects of processing of a metallic glass by applying various thermal loads in the absence of external forces, and allowing the system to relax through sequential STZ operations. Two types of thermal response tests are performed: (i) equilibration (relaxation of the glass) at a fixed temperature, and (ii) cooling simulations where the glass is relaxed over a finite time determined by an applied cooling rate in the range 10^1 to 10^4 K/s. All

the thermal response simulations are started from a system which is first equilibrated at a temperature of 1000 K which is just above the melting temperature of Vitreloy 1 at 993 K [22].

We begin by first examining the results of our equilibration simulations. Figure 2.6(a) shows the characteristic relaxation curves obtained in these simulations, where the instantaneous elastic strain energy density in the system is plotted as a function of time. The use of a semi-log scale permits all the equilibration curves to be presented on a single figure, but renders it difficult to

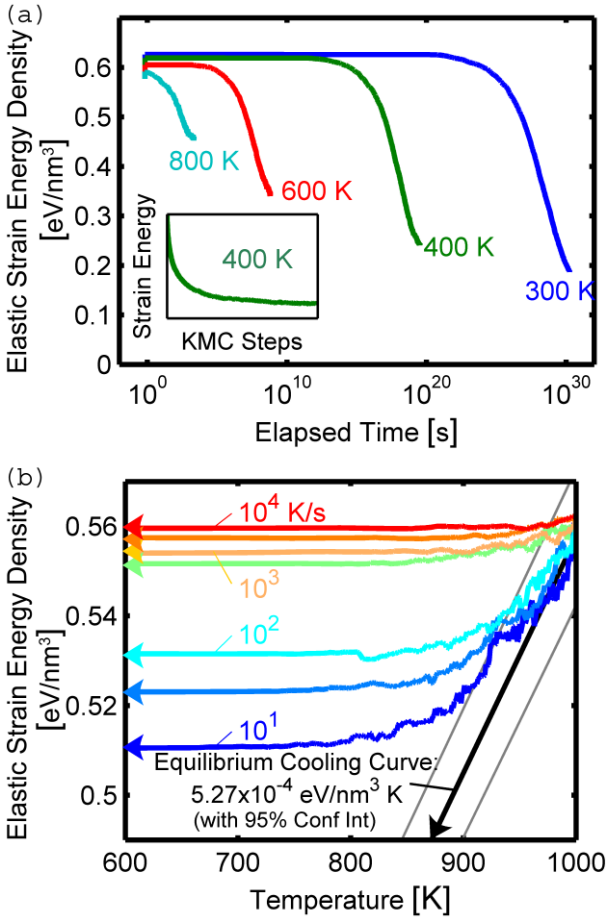

Figure 2.6 Simulated thermal processing of a metallic glass

(a) Plot of elastic strain energy density as a function of elapsed time for simulated equilibration of a metallic glass at different temperatures. The semi-log scale allows comparison of the different simulations but obscures the convergence of the value to a steady-state, which is shown in the inset for linear axes. (b) Plot of elastic strain energy denstiy as a function of temperature for simulated cooling of a metallic glass at different rates (10^1, 5×10^1, 10^2, 5×10^2, 10^3, 5×10^3, 10^4 K/s), where each curve represents the average of three simulations. In addition, the equilibrium cooling curve is plotted for comparison, which remains linear to room temperature and in principle to 0 K.

clearly observe that each of the systems has actually reached an equilibrated state. An example demonstrating the convergence to a steady-state value is shown in the inset of Figure 2.6(a), for the simulation at 400 K; all of these simulations show a similar convergence when plotted on linear time scales or as a function of the KMC time steps.

In Figure 2.6(a), all of the data shown are for equilibration at temperatures below the 1000 K starting state, and thus all the simulations shown involve an energy reduction. However, the steady-state is independent of prior history, and the equilibrated elastic strain energy density is in fact a simple function of temperature. We find that the elastic strain energy density is proportional to the temperature with a slope of 5.27×10^{-4} eV/nm^3·K. This linear trend is shown over a small range of temperatures in Figure 2.6(b), but remains linear for the range of temperatures simulated in this paper, and in principle remains linear to 0 K.

We now turn to the data obtained in the fixed cooling rate simulations, which are shown in Figure 2.6(b). Here each curve represents the average of three simulations at the same cooling rate, and plots the average elastic strain energy of the system as a function of temperature. As expected, the cooling experiments tend to track the equilibrium condition reasonably closely at first, until the temperature falls below a certain point; with further cooling the elapsed time of each KMC step rises quickly, and the system becomes kinetically trapped. The magnitude of relaxation achieved is greater for the slower cooling rates, in which a larger number of STZ operations are allowed.

It is interesting to note that the KMC approach, by permitting arbitrarily long time scales, can yield states not seen in experiments or other simulations. For example, our equilibrium elastic strain energy density trend in Figure 2.6(b) differs from prior suggestions that the energy associated with the fluctuations of atomic level stresses should depart from linearity for values below the glass transition temperature, T_g [48, 50, 82]. While such a departure from linearity is clearly possible when short time scales produce kinetically metastable structures (as in our cooling simulations in Figure 2.6(b)), the KMC algorithm allows the system to visit states that wouldn't be accessible on reasonable time scales, e.g. 10^{30} s (cf. Figure 2.6(a)). Thus, in our equilibrated structures we observe a linear reduction of system energy as temperature decreases well below T_g.

2.3.2. High Temperature Rheology

The high-temperature deformation of a metallic glass provides a convenient validation point for our model, since at sufficiently high temperatures (small λ), thermal energy dominates STZ activation, the local stress state becomes less important, and STZs are expected to act essentially independently of one another. Under such conditions, an analytical expression for the glass rheology is possible.

In the classical one-dimensional model, as described in section 1.3, STZs may shear either forward or backward, and combining the rates of these two processes yields the hyperbolic-sine stress dependent phenomenology in the steady state given in Eqn. 1.2 [9, 10]. This approach is readily expanded to a two-dimensional case where STZs can shear in any direction in the plane, which is more relevant for comparison with our model. In this situation the average strain rate is found by considering the contribution of strain from shear in STZ in any direction around the orientation circle. The derivation is very similar to that used to obtain Equation 2.4, and yields:

$$\dot{\gamma} = 2\pi \cdot \gamma_o \cdot \nu_o \cdot \exp\left(-\frac{\Delta F}{kT}\right) \cdot I_1\left(\frac{\tau \cdot \gamma_o \cdot \Omega_0}{2kT}\right). \tag{2.17}$$

where I_1 is a modified Bessel function of the first kind, of order one. Equations 1.2 and 2.17 predict remarkably similar strain rates for the same temperature and stress, with only subtle differences between them. For example, at low stresses, Equation 2.17 predicts a slightly faster strain rate (by a factor of ~2.2 at 50 MPa and T_g) because the extra degrees of freedom allow STZs that shear at off-angles to contribute to the forward strain rate. At high stresses, however, the extra degrees of freedom in Equation 2.17 actually predict a slower strain rate (by a factor of ~0.27 at 1 GPa and T_g) than Equation 1.2 because the off-angle STZ shearing events predict a slower strain rate than having all forward flips as in the one-dimensional model.

We study the rheological behavior of our simulated glass over a range of stresses at different constant temperatures near and above 623 K, the glass transition temperature of Vitreloy 1 [22]. We explore deformation in three different classes of structures:

- *Equilibrated structures* which are first equilibrated without an applied load at the test temperature, followed by application of a load at the same temperature.

- *Cooled structures* which are cooled from the equilibrated structure at 1000 K at a rate of 10 K/s to 300 K (cf. Figure 2.6(b)), prior to the application of a load at a different temperature.
- *Unequilibrated structures* which comprise an undeformed mesh, free from any prior STZ operations, with no internal stress distribution prior to loading at the test temperature.

In all cases, temperature and stress (in a loading state of pure shear, with displacement along the x-axis) are fixed at constant values, and the KMC algorithm evolves the system through sequential STZ operations.

Typical shear strain-time data for the three different structures are shown in Figure 2.7(a), for a load of 400 MPa at 623 K. The responses for the cooled and equilibrated structures are very similar, exhibiting almost instantaneously a constant steady-state strain rate. On the other hand, the unequilibrated structure exhibits a significant transient region, during which the structure is developing the beginnings of a steady-state internal stress distribution that permits more rapid deformation; the first few STZ operations are large perturbations in the unequilibrated system, and require longer times to occur. After the conclusion of the transient, however, the steady-state strain rate is essentially the same as that seen in the other two structures. The deformation in all the structures is also uniform, or homogeneous in nature, as expected. An illustration of the observed deformation is provided for the unequilibrated structure at a time intermediate to the final deformation, with the magnitude of the STZ strains shaded, which can be seen in the inset of Figure 2.7(a). All the high temperature deformation tests showed a similar uniform distribution of STZ strains and homogeneous deformation.

The steady-state strain rates of all three structures are plotted as a function of the applied load in Figure 2.7(b), for a variety of test temperatures. As expected based on our above discussion, we see that all three structures exhibit similar rheology in the steady-state condition. What is more, the shape of the datasets in Figure 2.7(b) is typical of homogeneous glass flow, exhibiting weakly rate-dependent near-Newtonian flow at low stresses, and a gradual increase in rate sensitivity with increasing stress. The predictions of Equations 1.2 and 2.17 are also plotted in Figure 2.7(b), both of which agree closely with the simulation results without the use of any adjustable parameters; this close agreement suggests that the assumption of independent STZ operation is well-founded at these temperatures near the glass transition. We also observe that

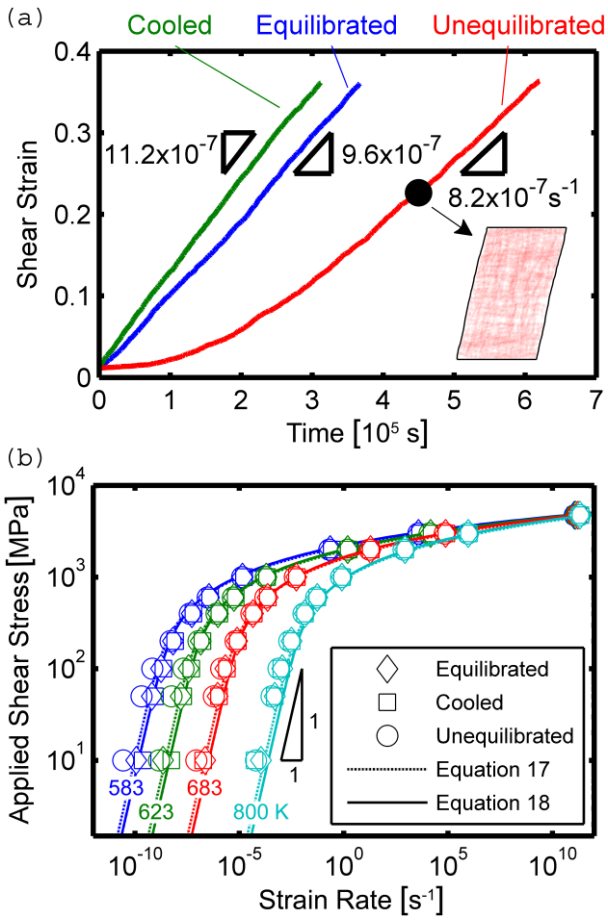

Figure 2.7 High temperature rheological response of simulations

(a) Typical strain-time data for the three different structures deformed at high temperatures (in this case 400 MPa and 623 K), which exhibit similar steady-state strain rates and overall shear strain. A snapshot is provided for the unequilibrated structure at the marked point, where the inset shows the physical deformation along with the magnitude of the plastic STZ strains, which are shaded. (b) Steady-state homogeneous flow data for several high temperature simulations of the three structures, plotted along with the predicted strain rates of Equations 1.2 and 2.17.

while the two-dimensional model of Equation 2.17 does provide somewhat improved predictions in some cases, the simpler one-dimensional model of Equation 1.2, with its classical hyperbolic-sine stress dependence, provides surprisingly accurate results with an error on average ~5% smaller than Equation 2.17.

2.3.3. Low Temperature Deformation

We now consider deformation of the same three structures at two temperatures, 300 and 400 K, well below the nominal glass transition temperature of Vitreloy 1 at 623 K. Typical strain-time data are shown in Figure 2.8(a) for the three different structures loaded at 1 GPa and 300 K,

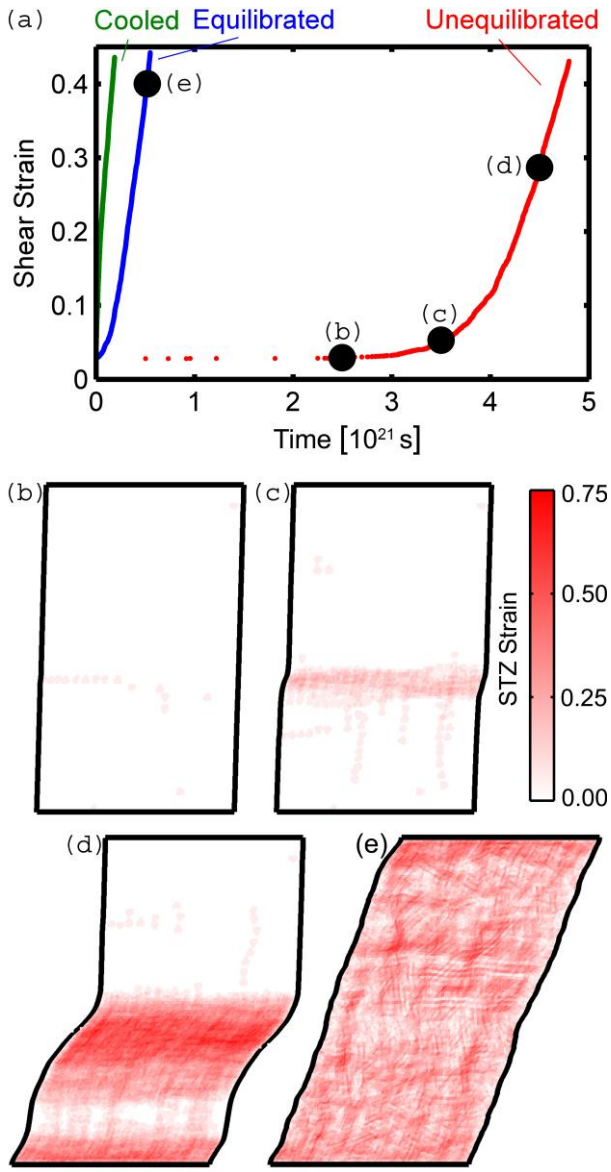

Figure 2.8 Low temperature response of simulations

(a) Typical strain-time data for the three different structures deformed at low temperatures (in this case 1 GPa and 300 K), which exhibit similar steady-state strain rates and overall shear strain, although they exhibit different transients. Markers (b), (c) and (d) correspond to snapshots of the unequilibrated structure at different times during deformation, illustrating the localization that proceeds formation of an elementary shear band. Marker (e) corresponds to a single snapshot of the equilibrated structure near the end of loading illustrating the homogeneous nature of the deformation.

where it can be seen that once a certain strain level is achieved, all three structures exhibit about the same strain rate. However, the three different structures exhibit very different initial responses to the applied load, where the cooled structure shows no transient region, the

equilibrated structure shows a small transient region and the unequilibrated structure once again shows a very significant transient region. The lack of a transient in the cooled structure can be attributed to the higher strain energy density that is frozen into the system, which is ~2.5 times greater than the strain energy density in the equilibrated structure. Thus in comparing the cooled and equilibrated structures, the higher stresses in the cooled structure make it more readily able to deform than the equilibrated structure which requires a transient region to initiate rapid deformation.

The significant transient region in the unequilibrated structure can again be attributed to the development of an internal stress distribution that facilitates deformation, where the first STZ operations represent large perturbations to the system that require a long time to occur. What is more, these first few STZs are spatially clustered, as shown in Figure 2.8(b), and ultimately assemble into the nucleus of a shear band as in Figure 2.8(c). Once this assemblage of STZs spans the specimen as in Figure 2.8(c), the stress state of the system is sufficiently perturbed to permit rapid shearing on this plane, which accumulates strain quickly as in Figure 2.8(d).

At low temperatures and high loads (large λ), a glass generally deforms inhomogeneously with the majority of plastic strain confined to very localized volumes, exactly as seen in the example of Figure 2.8(b)-(d). However, while this behavior was observed in the unequilibrated structure, the equilibrated and cooled structures deformed in a homogeneous fashion with no sign of localization in over 40 unique simulations, despite identical loading conditions. This homogeneity (or lack of inhomogeneity) in the equilibrated and cooled structures can, we believe, be attributed to the system size; the small physical size of the simulation cell falls in the reported range of the width of a fully developed shear band at $10^{-8} – 10^{-7}$ m [5, 29]. This may simply be too small to allow a shear band to develop in the complex stress field of an amorphous solid. The localization of the stress and strain distributions which give rise to shear banding requires a perturbation of sufficient size. In the unequilibrated structure, the perturbation is provided by thermal activation of the first few STZs, which generate stress and strain distributions of a large magnitude in an otherwise stress free mesh. Subsequent STZs are strongly biased by the perturbation, leading to the autocatalytic assembly of a shear band as in Figure 2.8(b)-(d). However, in the systems with pre-existing structural noise, a single STZ operation does not provide a sufficient perturbation to trigger shear banding, because stresses of similar magnitude are already distributed through the system; a larger perturbation is apparently

required, involving multiple STZ operations. In a small system such as ours, the probability for observing a perturbation of sufficient size is reduced. The role of large stress fluctuations inhibiting inhomogeneous deformation has been explored previously in Ref. [71] with a different model, and similar physics may be at work here.

In future work we will explore in more detail the conditions required to cause localization in these simulations. In addition to issues of scale, we also intend to incorporate local state variables, including structural parameters (such as free volume) and local temperature; these will permit additional perturbations in the local state and are known to generally lead to (or influence) localization [21].

2.3.4. Deformation Map

As a final illustration of the general capabilities of this model, we assemble in Figure 2.9 a deformation map derived from simulations on the unequilibrated structure. The map includes:

Contours of steady-state strain rate as a function of temperature and stress, for rates ranging from 10^{-10} to 1 s^{-1}. The material response at strain rate values much slower than 10^{-10} s^{-1} are assigned as nominally "elastic"; these data points are marked by an x rather than a square.

Local values of the strain rate sensitivity, *m*, defined as

$$m = \frac{d \ln \tau}{d \ln \dot{\gamma}}. \tag{2.18}$$

As the stress is increased, the value of *m* decreases from unity (Newtonian flow), and trends toward zero, which is associated with non-Newtonian flow and instabilities [83].

Regions to denote which samples deformed in a homogeneous manner and which samples deformed in an inhomogeneous manner.

The general features of the deformation map match well with expectations for metallic glasses [7, 10]. With the ability to reproduce the basic features of deformation of glass, we anticipate that the present STZ-dynamics model will be able shed new light on more obscure details of deformation that are not captured on the deformation map.

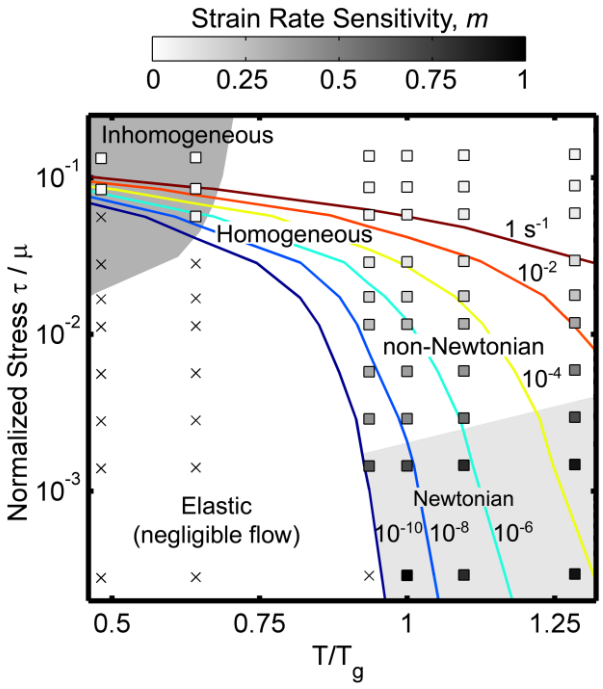

Figure 2.9 Deformation map constructed from simulated material response

The deformation map represents the material response of Vitreloy 1 constructed from the data obtained through loading the unequilibrated structure over a range of stresses and temperatures. The colored lines represent contours of different steady-state strain rates, where strain rates slower than 10^{-10} s^{-1} are considered to be elastic and are marked with an 'x'. Other data points are shaded according to their respective strain rate sensitivity, *m*, as indicated by the color bar above the map. Further regions marked as Newtonian (lightly shaded) and non-Newtonian are differentiated. Samples which deformed inhomogeneously are marked in a darkly shaded region while the rest of the samples deformed homogeneously.

2.4. Conclusions

In this chapter, we have developed a new meso-scale modeling technique for the mechanical behavior of metallic glasses, based on shear transformation zone dynamics. The important features of this modeling framework include the following:

- A model material is coarse-grained and mapped onto a mesh to form an ensemble of shear transformation zones (STZs), which are the fundamental units of plastic deformation.
- Finite element analysis and a kinetic Monte Carlo algorithm are used together in this model, the former to permit STZs to interact via their stress and strain fields, and the latter to permit time evolution of the ensemble.

The result is a model that can access significantly larger time and length scales than those typically available via atomistic modeling, with complex geometries and boundary conditions. These larger time and length scales are necessary to understand how microscopic deformation leads to macroscopically and experimentally observed behaviors.

We have presented a specific implementation of the modeling technique in two dimensions, to model a metallic glass over a range of thermal conditions and mechanical loads. Salient results from this exercise include the following:

- In equilibrium, there is a linear relationship between the stored elastic strain energy density and temperature. Cooling the system at a finite rate leads to a deviation from equilibrium and the entrapment of a kinetically metastable state with higher stored elastic strain energy density.
- Deformation of the system at high temperatures and at a constant load leads to steady-state strain rates regardless of the processing history (pre-existing internal stress distributions), although the processing history can affect the transient approach to steady-state. The steady-state rheology conforms well to simple analytical models that assume independence of STZs from one another. Both Newtonian and non-Newtonian flow are observed, in line with expectations.
- While deformation at high temperatures is observed to be homogeneous, at low temperatures inhomogeneous flow (i.e., shear banding) is observed in initially noise-free (unequilibrated) structures. In such systems, the first STZs that operate provide a perturbation that leads to autocatalytic shear band assembly. In contrast, systems with a thermal/processing history with significant pre-existing internal stress distributions deform in a homogeneous manner.

With the results obtained from numerous simulations, we assembled a deformation map for metallic glasses that is in line with expectations from the literature. As will be shown in the following chapters, the STZ dynamics model can be applied to understand more subtle details of glass deformation under complex boundary conditions.

3. Activated States and Correlated STZ Activity[2]

3.1. Introduction

The effort to answer questions surrounding the mesoscopic details of deformation in amorphous metals, as discussed in section 1.5, is facilitated through the use of mesoscale models because these models bridge the microscopic and macroscopic scales, both in terms of space and time. The purpose of this chapter is to revisit the results obtained in Chapter 2 with a goal of better understanding the conditions surrounding the selection and activation of STZs through additional analysis. Of particular emphasis is the way in which STZs communicate with one another via the redistribution of stress fields, which leads to spatial and temporal correlations between activated STZs. Although spatio-temporal correlations have been studied at the atomic [8, 41, 42, 85] and continuum [86] scale, this is the first study to explicitly explore such correlations among STZs in a mesoscale model of a deforming glassy system.

The analysis in this chapter is focused on the results obtained from the unquilibrated structure, described in sections 2.3.1 – 2.3.3, which is a model glass free from any pre-existing stresses and strains. The evolution of the system, containing more than 16,000 potential STZs, was followed over the course of more than 5,000 STZ activations for 60 combinations of applied stress, in the range of 10 MPa to 4.75 GPa, and temperature, in the range of 300 to 800 K. In what follows we analyze the STZ activity in these 60 simulations.

3.2. The Activated State

3.2.1. Calculating the Activated State

The KMC algorithm requires a model with which to calculate the activation energy, ΔG, of a transition or activated state. For an STZ Dynamics model, the activation event corresponds to a local traversal between STZ configurations, as shown schematically in Figure 3.1(a). The model of ΔG for such a process must satisfy detailed balance [78, 79, 87], and the calculations should also be efficient. Bulatov and Argon [13] proposed a model for ΔG that satisfies both these requirements for the case of STZ activation. This model was given implicitly in chapter 2 but is presented explicitly here as

$$\Delta G = \Delta F - \tfrac{1}{2}\tau \cdot \gamma_o \cdot \Omega_o \qquad (3.2)$$

[2] The contents of this chapter have been published previously as Ref. [84]

where, again, the intrinsic barrier height for the reaction, ΔF, is biased by the local shear stress τ, which is obtained by volume averaging the stress over the elements which comprise each potential STZ. This model is not immediately intuitive, so we provide some details here, along with points of contrast with respect to more traditional approaches used in KMC.

Consider an elementary reaction, the simple shearing of an STZ through a defined increment of strain γ_o, as shown in Figure 3.1(a). The value of the local plastic strain γ_p (defined parallel to a given shear plane) is incremented as

$$\gamma_p^F = \gamma_p^I + \gamma_o \tag{3.4}$$

where the superscripts *I* and *F* represent the initial and final values, respectively. There is a corresponding variation in elastic energy from the energy in the initial state, E^I, to the energy in the final state, E^F. This variation in elastic energy, which is a quadratic function of γ_p [88], can be calculated analytically for an idealized STZ using the Eshelby solution for an elastic inclusion [18], or can be evaluated numerically by visiting the final state following the transition.

A traditional KMC model uses the energy change to model the activation energy, ΔG, by adding a barrier of fixed height, ΔF, to the average of E^I and E^F, as illustrated in Figure 3.1(b). This approach satisfies detailed balance for the reaction because a forward transition traverses the same activated state as the reverse transition:

$$E^I + \Delta G_{I\to F} = E^F + \Delta G_{F\to I}. \tag{3.5}$$

with $\Delta G_{I\to F} = \left(E^F - E^I\right)/2 + \Delta F$ and $\Delta G_{F\to I} = \left(E^I - E^F\right)/2 + \Delta F$. However, this conventional approach of calculating ΔG is not well suited to an STZ Dynamics model; it requires calculation of the energy in the final state, which is both computationally expensive for a large number of possible transitions, and essentially impossible for continuously distributed shearing angles as used in the present model. Bulatov and Argon [13] exploited the property that the elastic energy, and therefore the total energy as well, is a quadratic function of γ_p to provide an alternate formulation for ΔG. This quadratic variation in energy is shown in both Figure 3.1(b) and Figure 3.1(c), illustrating that the system evolution is independent of the model for the activated state.

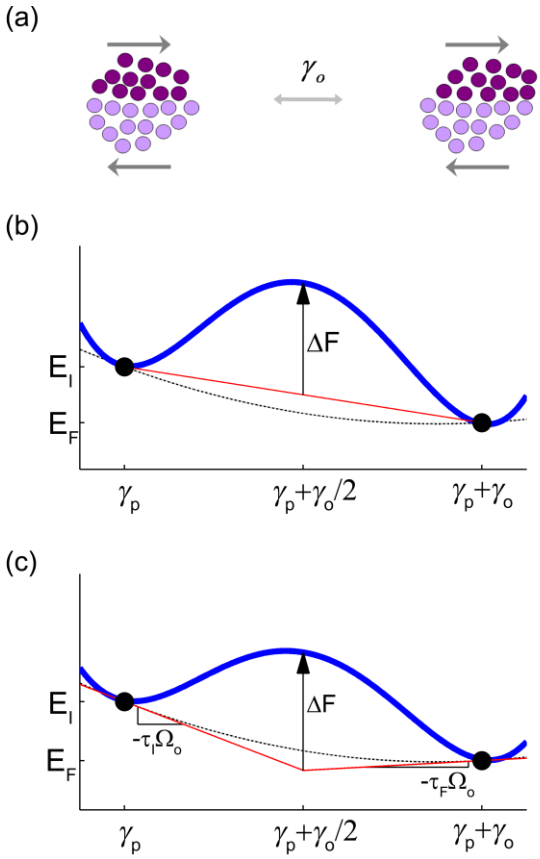

Figure 3.1 Potential energy landscape models for STZ activation

(a) Representation of the two states before and after the activation of an STZ. Illustration of the energy landscape and the method of identifying the activated state of an STZ in a (b) traditional KMC model where the activation energy, ΔG, is obtained by adding the fixed energy barrier ΔF to the average of the initial and final states, and (c) the energy landscape for the model proposed by Bulatov and Argon [13] where ΔG is obtained by adding ΔF to the projection of the slope (equal to the local shear stress) at the initial and final states. The variation in energy between the two states is given by the dashed line and is the same in both (b) and (c).

It can be shown that the local shear stress resolved in the shear plane of γ_p is given by the slope of the variation in energy,

$$\tau = -\frac{1}{\Omega_o}\frac{\partial E}{\partial \gamma_p} = -\frac{E'(\gamma_p)}{\Omega_o}. \qquad (3.6)$$

Given Equation 3.6, ΔG for the transition, as defined in Equation 3.2 and illustrated in Figure 3.1(c), is determined by projecting with the slope, τ^I, from the energy of the initial state to the

midpoint of the reaction, $\frac{1}{2}\gamma_o$ (energy variation $-\frac{1}{2}\tau^I\Omega_0\gamma_0$), and then adding the fixed barrier height, ΔF. Detailed balance for this model of ΔG is satisfied because

$$E^I + \left(\Delta F - \tfrac{1}{2}\tau^I\Omega_o\gamma_o\right) = E^F + \left(\Delta F - \tfrac{1}{2}\tau^F\Omega_o\left(-\gamma_o\right)\right), \tag{3.7}$$

which follows a property of quadratic functions that $E\left(\gamma^I\right) + E'\left(\gamma^I\right)\cdot\left(\gamma^F - \gamma^I\right)/2 = E\left(\gamma^F\right) - E'\left(\gamma^F\right)\cdot\left(\gamma^F - \gamma^I\right)/2$. This is illustrated in Figure 3.1(c) by the fact that the tangents to the variation in energy at the initial and final states, τ^I and τ^F respectively, cross exactly at $\frac{1}{2}\gamma_o$.

This model for ΔG is efficient because it only requires knowledge of the initial condition, and the contribution of continuously distributed shear planes to the STZ activation rate can be considered in a mathematically convenient form (Equation 2.5).

3.2.2. Statistics of the Activated State

At each of the KMC steps in the simulation, the algorithm has more than 16,000 potential STZs from which to choose to evolve the system. The statistics of these potential transitions are available in the density of potential activation energies, $\rho(\Delta G)$, and the corresponding probability density distribution, $p(\Delta G)$, defined as

$$p\left(\Delta G\right) = \frac{1}{Z}\,\rho\left(\Delta G\right)\cdot\exp\left(-\frac{\Delta G}{kT}\right) \tag{3.8}$$

where Z is the partition function. Both $\rho(\Delta G)$ and $p(\Delta G)$ are averaged over all the KMC steps to smooth out the effects of individual transitions that might be more abundant at different steps. We will also consider $\rho_S(\Delta G)$, the energy distribution of the transitions selected in the course of simulations. Figure 3.2 presents the measured distributions of $\rho(\Delta G)$ and $\rho_S(\Delta G)$ along with $p(\Delta G)$ calculated according to Equation 3.8 for four simulations which cover two temperatures, 300 and 623 K, and two applied shear stresses, 100 MPa and 1 GPa.

It is important to recall that our KMC algorithm allows each STZ to shear in any direction, thus creating a continuum of transition states for each potential STZ. This is incorporated into the rate equation by calculating the maximum in-plane shear stress, $\tau_{\max}$, and then modulating that

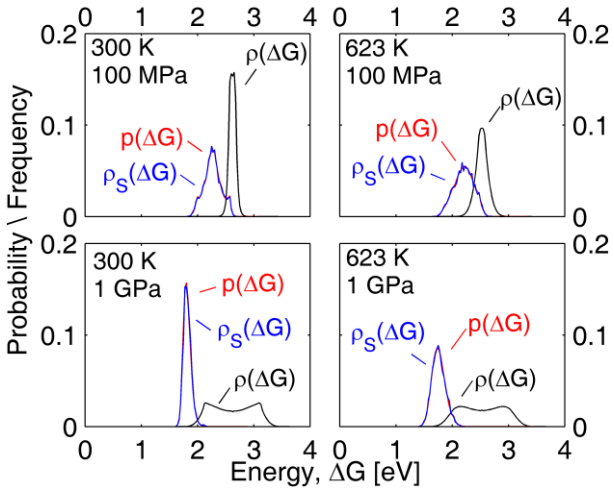

Figure 3.2 Statistics of the activated states for STZ transitions

Statistics of the density of activation energies, $\rho(\Delta G)$, and the corresponding probability density distribution, $p(\Delta G)$, alongside the density of selected activation energies, $\rho_S(\Delta G)$, for four different simulations carried out under a combination of temperatures, 300 and 623 K, and applied stresses, 100 MPa and 1 GPa

value by the sine of the angle relative to the direction of $\tau_{\max}$ as defined by

$$\Delta G = \Delta F - \tfrac{1}{2}\tau_{\max} \cdot \sin\theta \cdot \gamma_o \cdot \Omega_o . \qquad (3.9)$$

It follows that the distributions of $\rho(\Delta G)$ are symmetric about the intrinsic barrier height, ΔF, and the contribution of each potential STZ is limited to $\pm\tfrac{1}{2}\tau_{\max} \cdot \gamma_o \cdot \Omega_o$, where energies below ΔF are for transitions in the direction of the local $\tau_{\max}$, and those above ΔF are opposed to it.

In calculating the distributions of $\rho(\Delta G)$ in Figure 3.2, we have used 360 uniform increments of θ on the interval $[-\pi, \pi)$, and a bin size on ΔG of 0.025 eV. Therefore, at the lower applied stress of 100 MPa, the range of $\Delta F \pm \tfrac{1}{2}\tau_{\max} \cdot \gamma_o \cdot \Omega_o$ is small and the distributions of $\rho(\Delta G)$ at both temperatures, 300 and 623 K, are narrow and appear unimodal, obscuring the tendency to see an increased number of states at the limits. For the higher applied stresses of 1 GPa however, $\rho(\Delta G)$ appears bimodal on account of the increased magnitudes of $\tau_{\max}$ which result in a spread of the data, accentuating the increased number of transitions with energy close to the limiting values of $\Delta F \pm \tfrac{1}{2}\tau_{\max} \cdot \gamma_o \cdot \Omega_o$.

While the temperature dependence of ΔF, defined in Figure 3.2, can be seen by the slight decrease in ΔF at higher temperatures, the temperature effects are more noticeable in the broadening of $\rho(\Delta G)$ at higher temperatures. The greater thermal energy available at these higher temperatures allows more transitions to take place, creating different states and more potential transitions of varying energies during the course of the simulation.

While $\rho(\Delta G)$ gives the distribution of all potential transitions that are enumerated in the KMC algorithm, the probability, $p(\Delta G)$, for picking a transition with energy ΔG is a competition between the number of transitions at that energy, $\rho(\Delta G)$, and the available thermal energy, *kT*, as in Equation 3.8. In these simulations, the available thermal energy is small in comparison with the energy of the transitions, in the range of ~ 0.02 – 0.07 eV, making the lowest energy transitions the most likely to be selected. And indeed, in Figure 3.2 it can be seen that although $\rho(\Delta G)$ spans a large range of energies, only the transitions corresponding to the lower portion of this range are probabilistically relevant. At 100 MPa and at both temperatures, $p(\Delta G)$ is only relevant over the lower half of the range of $\rho(\Delta G)$, which corresponds to shearing an STZ in the general direction of $\tau_{\max}$. At 1 GPa, however, only the transitions very close to the direction of $\tau_{\max}$ are likely to be selected. In all cases, the probability for picking an STZ opposed to the direction of $\tau_{\max}$ (where $\Delta G > \Delta F$) is near zero, because the thermal energy required to activate these 'backward' processes is too large.

As expected, the transitions selected, $\rho_S(\Delta G)$, closely match the expectations based on $p(\Delta G)$, as shown by the virtually perfect overlap of these curves for all conditions in Figure 3.2.

3.3. STZ Correlations

Having detailed the activated state and the conditions that lead to the probabilistic selection of STZs, we turn our attention to an analysis of the correlations between the STZ activations in both space and time.

An irregular triangular mesh with several potential STZs highlighted; each is centered on an element and includes all surrounding elements. Overlap between STZs is denoted by the darker shading, and circles with radii equal to 1, 2.5 and 5 times the STZ radius are centered on STZ 'D' to indicate the distance between potential STZs.

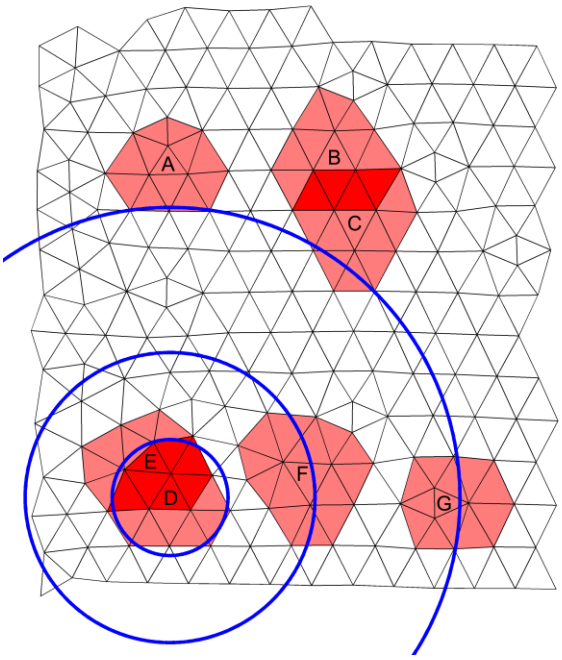

Figure 3.3 Illustration of distance between STZ activations

From the highlighted STZs defined on an irregular triangular mesh and activated in alphabetical order, one can gauge the distance of correlations between activations. The circles defined in blue have radii equal to 1, 2.5 and 5 times the STZ radius from the STZ centered on STZ 'D'.

An illustration of our approach can be seen in Figure 3.3, where the highlighted STZs can be thought of as being activated or sheared in alphabetical order. We analyze the distance, r, between the center of each selected STZ and the following j^{th} subsequent STZ activation. Our unit of distance is the average radius of an STZ, and a reference for gauging the distance r between STZ 'D' and the j^{th} activation (i.e., E, F, G…) that follows is given by the circles centered on 'D' with radii of 1, 2.5 and 5 times the average STZ radius.

In some cases it is instructive to use the time and distance between activations to simply calculate the number fraction of sequential STZ events that occur within a given radius of a previous STZ activation. In other cases a richer view is offered by inspecting the time-dependent radial distribution function (TRDF) of STZ activations. The TRDF is given by

$$g(r,j)=\frac{n(r,j)}{q(r)} \tag{3.10}$$

where $n(r,j)$ is constructed by binning the number of sequential activations as a function of r and j, and $q(r)$ is defined as

$$q(r) = \begin{cases} 1 & \text{if } r \le \dfrac{1}{2\pi \cdot dr \cdot \rho_{STZ}} \\ 2\pi \cdot r \cdot dr \cdot \rho_{STZ} & \text{if } r > \dfrac{1}{2\pi \cdot dr \cdot \rho_{STZ}} \end{cases} \tag{3.11}$$

where ρ_{STZ} represents the overall density of STZ activations., i.e., the total number of STZ activations per unit area. The normalization quantity $q(r)$ represents a uniform STZ activation density and the piecewise form of Equation 3.11 is introduced to prevent the divergence of $g(r, j)$ as r → 0 for discrete systems such as ours. The size of the bins, *dr*, for the TRDFs analyzed here is approximately equal to half of the STZ radius.

3.3.1. General STZ Correlation Behaviors

An analysis of the 60 different simulations reveals three basic types of behavior that manifest under different combinations of applied stress and temperature. These behavior types are cataloged in Figure 3.4 by the characteristic form of the TRDF they exhibit, and are described below.

- 'Nearest-Neighbor STZ Activation', which is observed for the simulations deformed at high applied stress and low temperatures, is illustrated in Figure 3.4(a). This behavior is characterized by an early, broad peak spanning roughly r = 1 to 5, centered between about 2 and 3. As shown by the circles in Figure 3.3 (which are located at r = 1, 2.5, and 5), the peak breadth corresponds to activations in the immediate neighborhood of the first STZ, centered on what may be called the nearest-neighbor distance. The peak in the TRDF is generally three to five times the value for a uniform distribution, and persists only for early times from the first STZ activation ($j \approx 1-3$) indicating that the frequency for immediate subsequent activation of a neighboring STZ is higher than that for uniform activation throughout the simulation cell (cf. STZs D, F and G in Figure 3.3). For values of r less than 1, however, $g(r,1) \sim 0$ indicating that the frequency for activating STZs that spatially overlap the original STZ (or for reactivating the original STZ itself) in subsequent steps is nearly zero (cf. STZs D and E in Figure 3.3).
- 'Independent STZ Activation', which occurs under conditions of high applied stress and high temperatures, is illustrated in Figure 3.4(b). In this behavior the TRDF once again shows no preference for re-activation of STZs atop the first one, since again $g(r, j) \sim 0$

at $r < 1$. However, at higher temperatures the tendency for activation of neighboring STZs is lost; there is no longer a discernible peak elsewhere in the TRDF, which is valued near unity for all $r > 1$ and $j \geq 1$. This constant value of the TRDF indicates that all STZs throughout the simulation cell are equally likely to activate; there is no correlation among STZs.

- 'Self STZ Activation', which dominates at low applied stress and any temperature, is illustrated in Figure 3.4(c). Unlike the previous behaviors, Figure 3.4(c) exhibits an extremely pronounced and sharp peak in the TRDF at $r = 0$ and for early times (j < 4). The spatial extent of the peak is limited to $r \leq 1$, indicating a large preference for a second STZ activation atop the first. For all other $r > 1$ and all j, $g(r, j) \sim 1$ indicating zero preference for correlated STZ activity at large distances.

The three behaviors identified in Figure 3.4 coincide with three different types of macroscopic deformation that are easily identifiable on a deformation map. Namely, the 'Nearest-Neighbor STZ Activation' occurs under conditions which lead to inhomogeneous deformation, 'Independent STZ Activation' occurs under conditions which lead to homogeneous deformation, and 'Self STZ Activation' occurs, in general, under conditions which are identified with nominally elastic behavior, of which the macroscopic behaviors are described in chapter 2.

The connection between 'Nearest-Neighbor STZ Activation' and macroscopic inhomogeneous deformation mode is relatively straightforward. At high stresses, the system is most likely to activate all STZs in the direction of the applied stress. Once one STZ is activated, it raises the stress in all neighboring STZs, and where the available thermal energy is low at low temperatures, the frequency for 'Nearest-Neighbor STZ Activation' is increased, leading to localized deformation. For 'Independent STZ Activation', which occurs at high applied stress and high temperature, the available thermal energy is now sufficient to enable STZ activation at other positions even though the stress in the neighboring STZs is high.

'Self STZ Activation' is linked to the elastic regime for two reasons. First, at low temperatures, there is insufficient thermal relaxation to accommodate a single STZ operation, and at low stresses, there is insufficient tendency for a single STZ to trigger nearest-neighbor activations; thus, the most likely response of the system is for each STZ activation to be nearly instantaneously reversed. Second, the activation energy associated with most of these transitions

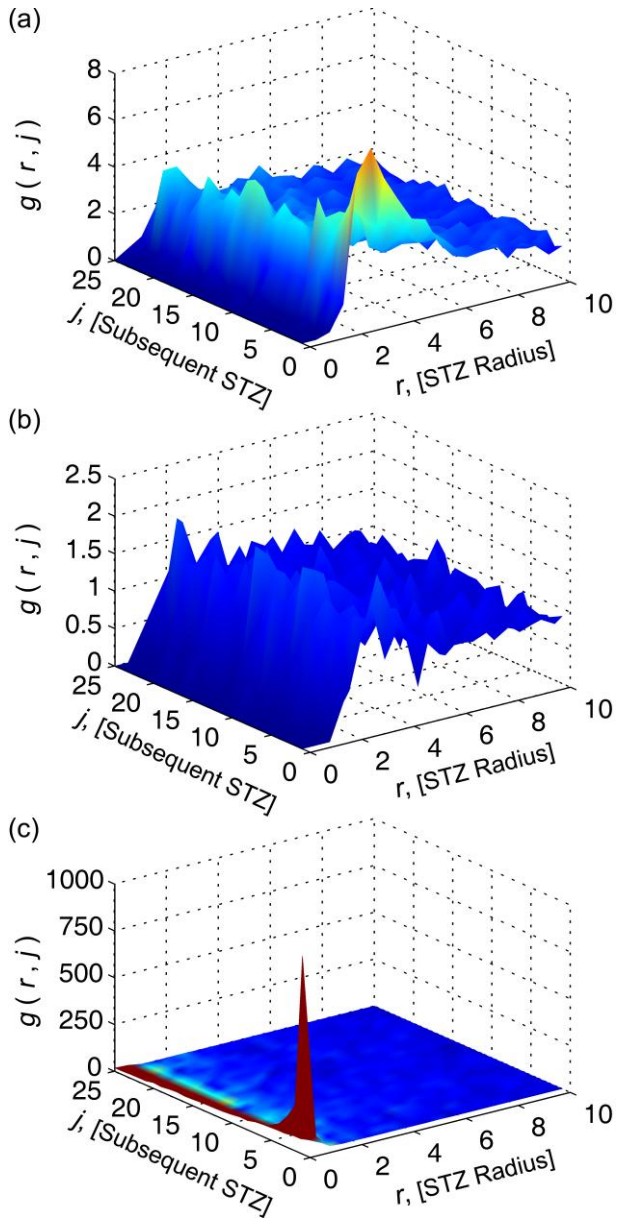

Figure 3.4 General behaviors in the TRDFs of STZ activation

The three behaviors and their corresponding conditions are (a) Nearest-Neighbor STZ Activation: high stress and low temperature, (b) Independent STZ Activation: high stress and high temperature, and (c) Self STZ Activation: low stress and any temperature. The shading of all three surfaces uses the same color scheme, permitting comparison of the magnitudes of the different trends.

is very large, and when little thermal energy is available, this leads to large KMC step times, and thus extremely slow strain rates, which are not experimentally relevant. Thus, when 'Self STZ

Activation' behavior is observed, the system evolves very slowly, and the effect of forward plastic events is quickly diminished by backward ones at essentially the same location, indicating that the system is more likely to remain effectively elastic.

While the general types of STZ activity identified in this section are instructive, neither all of their features nor the transitions between them are well defined as yet. A more detailed analysis follows, in which we find it useful to decompose the observed correlations into the spatial and temporal components.

3.3.2. Spatial Correlation Analysis

To better understand the spatial component of the STZ correlations identified as 'Self STZ Activation' and 'Nearest-Neighbor STZ Activation', the values for the TRDF of STZ activity may be plotted as contours over the range of available temperatures and applied stresses. These contour plots of $g(r, j)$ are presented in Figure 3.5 where Figure 3.5(a) corresponds to the value of the 'Self STZ Activation' peak at $r = 0$ and Figure 3.5(b) corresponds to the value of the 'Nearest-Neighbor STZ Activation' peak at $r = 2.5$. In both cases, we consider only $j = 1$ to focus solely on the first subsequent STZ activation. We observe that the 'Self STZ Activation' behavior is dominant at low stress, and while it extends over the entire temperature range covered in Figure 3.5(a), it is especially important at low temperatures where the magnitudes of the contours are significantly higher. These observations are in good agreement with the proposed connection between this STZ behavior and the elastic range, which is indeed prevalent at low stresses and temperatures. The extension of this behavior to the higher temperatures is somewhat unexpected because in this range creep-like homogeneous flow is expected. This issue can be resolved by examining the number fraction of subsequent STZ activations that can be identified with 'Self STZ Activation'.

The number fraction of subsequent STZ activations that are associated with 'Self STZ Activation' and 'Nearest-Neighbor STZ Activation' are shown in Figure 3.5(c) and Figure 3.5(d), for events which fall in the range $0 \le r \le 1$ and $1 < r \le 5$, respectively. Now, by comparing Figure 3.5(c) and Figure 3.5(a), we observe that although the peak in the TRDF for 'Self STZ Activation' persists to high temperatures at low stresses, the fraction of events contributing to that peak is very low indeed. The reason for the apparent discrepancy is that the

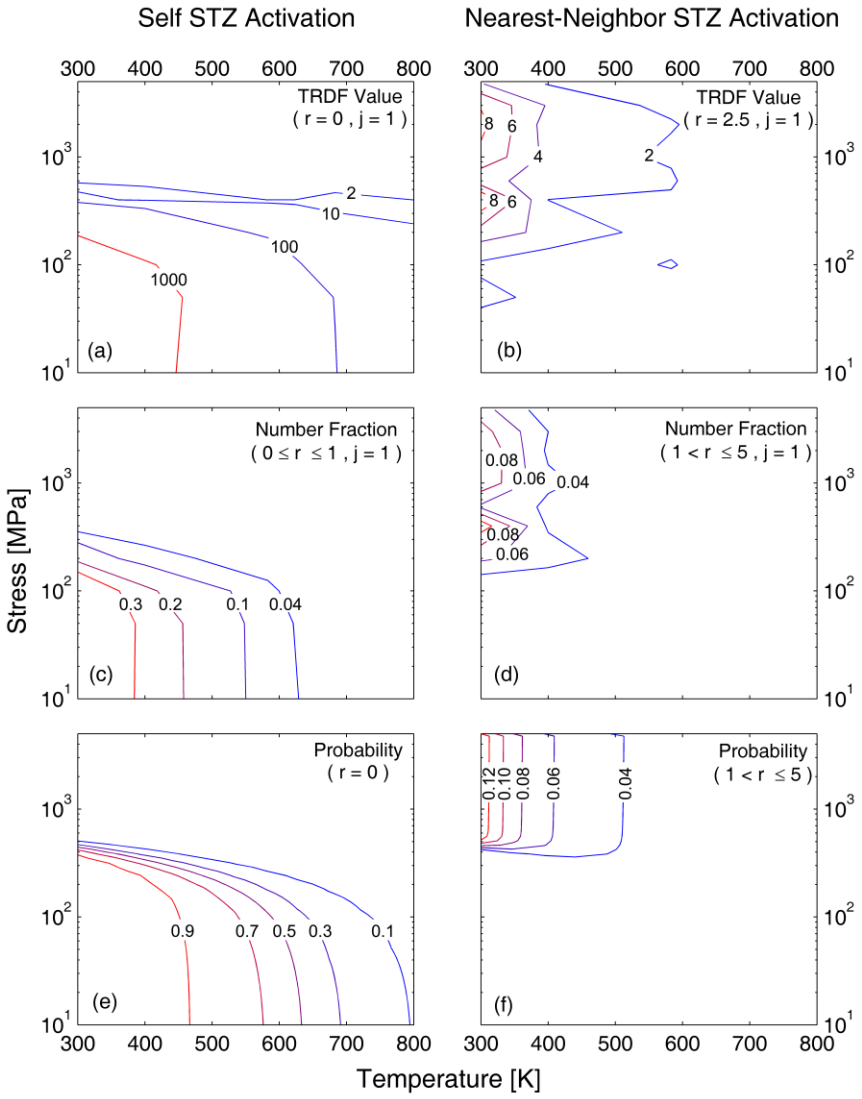

Figure 3.5 Spatial correlations of STZ activation

Contour plots of several different statistical measures that capture STZ correlations over a range of applied stresses and temperatures: (a) the TRDF values of 'Self STZ Activation', $g(r=0,\ j=1)$ **and (b) of 'Nearest-Neighbor STZ Activation'** $g(r=2.5,\ j=1)$ **; (c) number fraction of subsequent,** $j=1$**, 'Self STZ Activation' events within the range** $0 \le r \le 1$**; and (d) number fraction of subsequent 'Nearest-Neighbor STZ Activation' events within the range** $1 < r \le 5$**. Contour plots of the probability of (e) 'Self STZ Activation' and (f) 'Nearest-Neighbor STZ Activation' following the activation of a single STZ in a simulation cell over a range of temperatures and applied stresses.**

TRDF tends to accentuate information near the origin (r = 0), where very few events are needed to cause a peak to emerge. In contrast, Figure 3.5(b) and Figure 3.5(d) for the 'Nearest-Neighbor

STZ Activation' behavior show a closer agreement to one another. In this case, larger values of *r* are of interest, and the TRDF accordingly requires larger numbers of events before a peak emerges.

As an additional point of reference for establishing the regions for the different behaviors of correlated STZ activity, a simple simulation was carried out to calculate the probabilities for 'Self STZ Activation' or 'Nearest-Neighbor STZ Activation' following the activation of a single STZ. In other words, a single STZ was activated in a simulation cell with no internal structure (no stress distribution), and afterwards, the probability for activating that same STZ or a nearest-neighbor STZ was calculated over a range of temperatures and applied stresses. These probabilities can be seen in Figure 3.5(e) and Figure 3.5(f), for the 'Self STZ Activation' and 'Nearest-Neighbor STZ Activation' probabilities. It is noted that the probabilities for these regions are higher than the observed fractions in Figure 3.5(c) and Figure 3.5(d); however, this can be attributed to the fact that the probabilities are calculated for a cell in which there is only one STZ activated. On the other hand, when a distribution of stresses and strains is present due to a prior history of STZ activity, the competing probabilities of many other possible events decreases the relative probability for correlated STZ activity; it does not, however, remove it altogether.

One final point of interest in Figure 3.5(b), Figure 3.5(d) and Figure 3.5(f) is that the probability/frequency for 'Nearest-Neighbor STZ Activation' drops off at very high stresses. This results from the fact that the magnitude of the stresses resulting from individual STZs is small in comparison to the very high applied stress, removing the preference for 'Nearest-Neighbor STZ Activation'.

3.3.3. Temporal Correlation Analysis

In examining the general behaviors of correlated STZ activity in Figure 3.4, it can be seen that where there is a significant peak, $g(r, j) > 2$, in the TRDF, there is also a time dependence to the peak. These peaks appear to exhibit a general first-order decay, and as such, the time dependence of the correlations can be quantified with a first-order time constant. The time constant δ is measured in KMC steps, *j*, and gives the number of subsequent STZ activations over which the likelihood of correlated STZ activity decays by $1\text{-}e^{-1}$.

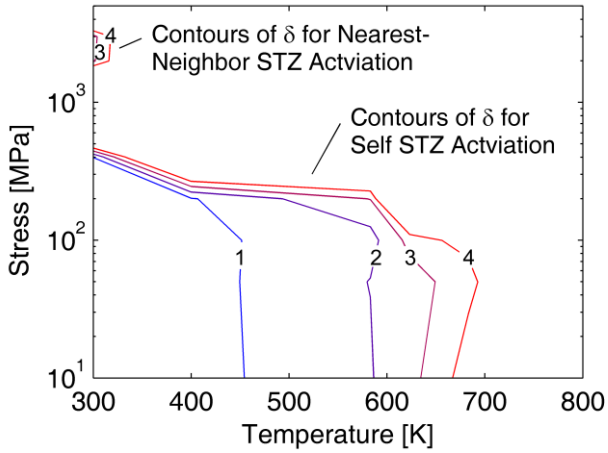

Figure 3.6 Temporal correlation of STZ activations

Contour plot of the time constant, δ, which measures the time decay of the TRDF correlation peaks at $r = 0$ for the 'Self STZ Activation' correlation and at $r = 2.5$ for the 'Nearest-Neighbor STZ Activation' correlation. Regions not enclosed by the contours did not provide a satisfactory fit for δ.

Because temporal correlations only exist when a peak is evident in the TRDF, we focus our measurements of δ on two values of *r*, 0 and 2.5, which correspond to the 'Self STZ Activation' and 'Nearest-Neighbor STZ Activation' behaviors, respectively. In order to find the best fit for δ, an exponential function is set to match the initial peak height at $j = 1$ and the average peak height at $j = 20 - 25$ and then a least-squares method is used to determine an appropriate value for δ. Those values of δ obtained from reasonable exponential fits ($R^2 > 0.8$) are presented in Figure 3.6, and labeled with the behavior corresponding to the position of the fitted peak, 'Self STZ Activation' (r = 0) and 'Nearest-Neighbor STZ Activation'(r = 2.5). As expected, the regions enclosed by the two different behaviors shown in Figure 3.6 match reasonably with those shown in Figure 3.5. In all cases, the value of δ is always less than five STZ activations, indicating that the lifetime for correlations between STZ activations is very short-lived.

Physically this short life span of correlated STZ activity implies that the probability of observing a large string of correlated events is negligible. Indeed in all of the 60 simulations, a string of more than two sequential nearest-neighbor STZ activations was rarely observed. The reason for this lies in the fractions and probabilities for 'Nearest-Neighbor STZ Activation' shown in Figure 3.5(d) and Figure 3.5(f), respectively, where the probability for activating a nearest-

neighbor STZ is systematically less than 10%. This means that the probability to observe a string of three correlated events is approximately 1% or less.

3.3.4. STZ Correlation Map

An STZ correlation map can be compiled from the above analysis to illustrate how the general STZ correlation behaviors are governed by the externally imposed applied stress and temperature. This map can be seen in Figure 3.7, where the different regions denote the conditions under which 'Self STZ Activation', 'Nearest-Neighbor STZ Activation' and 'Independent STZ Activation' are most likely to occur. As can be seen in Figure 3.5 and Figure 3.6, none of the regions corresponding to the different STZ correlations match exactly, so qualitative boundaries for these regions have been identified in Figure 3.7. Furthermore, Figure 3.7 is provided in normalized units for comparison to a wider range of metallic glasses, with the stress normalized by the temperature-dependent shear modulus, $\mu(T)$, and the temperature

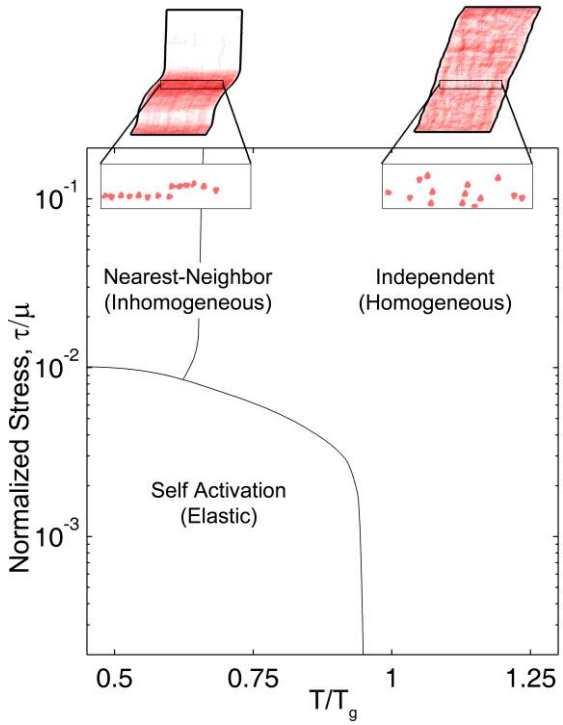

Figure 3.7 STZ correlation map

The different regions delineating the 'Nearest-Neighbor STZ Activation', 'Independent STZ Activation' and 'Self STZ Activation' correlation behaviors are matched with the corresponding macroscopic modes of deformation, named in parentheses.

normalized by $T_g = 623$ K, a glass transition temperature close to that of many Zr-based BMGs [80]. As mentioned previously, these regions coincide well with the different modes of macroscopic deformation that were observed in chapter 2, and are commonly observed in experiments of metallic glasses, namely elastic, inhomogeneous and homogeneous, respectively. Of course, the boundaries between these regions are not rigid, and there are occasional correlated events that occur outside the defined regions of correlated STZ activity. However, in general the regions delineated in Figure 3.7 accurately capture the microscopic STZ correlations (and align with the macroscopic modes of deformation) observed in the simulations.

3.4. Macroscopic Inhomogeneity

The macroscopic nature of deformation in an amorphous metal is typically easy to discern in the limiting cases of localized shear and perfectly homogeneous deformation. However, not all cases of deformation fall cleanly into one of these two categories, and an objective measure to assess the degree of localization would be helpful. To do so here, we adapt an analysis approach useful for quantifying the size of deformation and relaxation events in atomistic simulations, called the participation ratio, which gives the fraction of atoms that participate in any given process [75, 89]. We introduce a quantitative measure termed the 'localization index', which while inspired from and similar in form to the atomistic participation ratio, can be used to quantify localization on a macroscopic level:

$$\Gamma = 1 - \frac{\left(\sum_n \gamma_n^2\right)^2}{N \sum_n \gamma_n^4} \tag{3.12}$$

where γ_n is the plastic strain accumulated through STZ activity in each of the N mesh elements of the simulation cell following deformation. The localization index, Γ, identifies the fraction of the cell that participates in the overall deformation, thus giving an objective measure for the degree of localization or inhomogeneity. The value of Γ will range from unity if all the strain is concentrated on an infinitely thin shear band to zero for deformation that is perfectly uniformly distributed across the entire simulation cell. We find that values below about 0.5 correspond to very homogeneous flow, with a superimposed background of noise (as expected in a disordered solid).

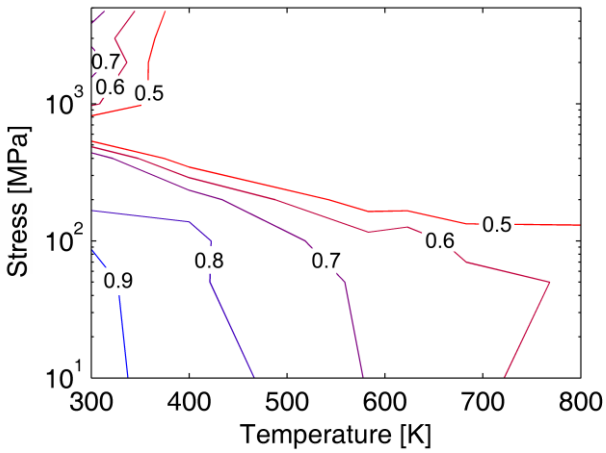

Figure 3.8 Contour plot of the localization index

The localization index, Γ, is plotted in contours for samples deformed at different combinations of applied stress and temperature. The region enclosed at high temperature and low applied stress corresponds to localization in large visible bands of concentrated shear, while the region enclosed at low applied stress is exhibited by small pockets of large strain in an otherwise uniformly deformed sample.

The value of Γ obtained by analyzing the 60 simulations is plotted in contours for fractions of Γ greater than 0.5 in Figure 3.8. The value of γ_n in this case is the effective plastic strain [90] (in 2-D) in each element, defined as

$$\varepsilon_{eff} = \sqrt{\tfrac{2}{3}\cdot\left(\varepsilon_{11}^2 + \varepsilon_{22}^2 + \tfrac{1}{2}\gamma_{12}^2\right)}, \tag{3.13}$$

where ε_{11}, ε_{22} and γ_{12} represent the plastic strain in the x and y directions and the plastic shear strain, respectively. (Since the former two strains are small, using only the component γ_{12} in the direction of the applied stress yields nearly identical results.) As expected, the region of correlated 'Nearest-Neighbor STZ Activation' (cf. Figure 3.5, Figure 3.6 and Figure 3.7) is enclosed in a region of high Γ. This confirms that local correlations in STZ activity lead to localization on larger scales where visible regions of inhomogeneous deformation can be identified, even if no large chain of sequential events is ever observed. On the other hand, the region of high Γ at low stresses and temperatures may seem unexpected since it corresponds to the elastic response of the material. The reason for this apparent discrepancy is that the nature of the inhomogeneity at low stresses is different than that at high stresses. At low stresses, the high value of Γ is due to small pockets of high strain in a sample that is otherwise uniformly

deformed; these pockets are also the result of STZ activations that occur on unreasonable time scales, leading to apparently elastic deformation. Furthermore, it is noted that the high value of Γ at low stresses may be due to the fact that the magnitude of overall shear strain that has accumulated during the simulations is small, and a nominally homogeneous sample may look heterogeneous when observed on short timescales.

3.5. Effects of pre-existing structure

In the above discussion, all of the simulations began from a homogeneous, undeformed simulation cell (which we called 'unequilibrated' in chapter 2). We now consider the effects of pre-existing structure, by analyzing the same set of conditions on model glasses subjected to the simulated thermal processing prior to loading discussed in chapter 2. These structures were formed by either (a) cooling at a rate of 10 K/s from an initial temperature of 1000 K, or (b) equilibrating the system at the same temperature as the simulated mechanical test, as described in chapter 2. Both these treatments have the effect of freezing in a distribution of stresses, with the 'cooled' structure having the highest magnitude of residual stresses, and the 'equilibrated' structure having a lower magnitude of residual stresses.

These two thermally processed structures were subjected to the same 60 combinations of pure shear stress and temperature as the 'unequilibrated' structure discussed above and followed over the course of 5,000 STZ activations. In the analysis in chapter 2, the 'cooled' and 'equilibrated' structures exhibited roughly the same overall strain rates as the 'unequilibrated' structure, but the 'cooled' and 'equilibrated' structures never showed any macroscopically inhomogeneous deformation like the 'unequilibrated' structure did. We performed the same analysis as provided in sections 3.2-3.4 on the 'cooled' and 'equilibrated' structures. This analysis led to almost identical results for the two, so here we discuss only the results for the 'cooled' structure.

The distribution of pre-existing stresses in the 'cooled' structure has the effect of broadening the distributions of $\rho(\Delta G)$ for the combinations of applied stress and temperature shown in Figure 3.9. The distribution of $p(\Delta G)$, however, seems to be narrower for the 'cooled' structure at lower energies when compared with the 'unequilibrated' structure, which results from the long non-zero tails in the $\rho(\Delta G)$ distribution where the thermal energy dominates the probability for activating these lower energy transitions. Once again $\rho_S(\Delta G)$ matches $p(\Delta G)$ almost exactly. However, the most important note to be made about the activation energies shown in Figure 3.9

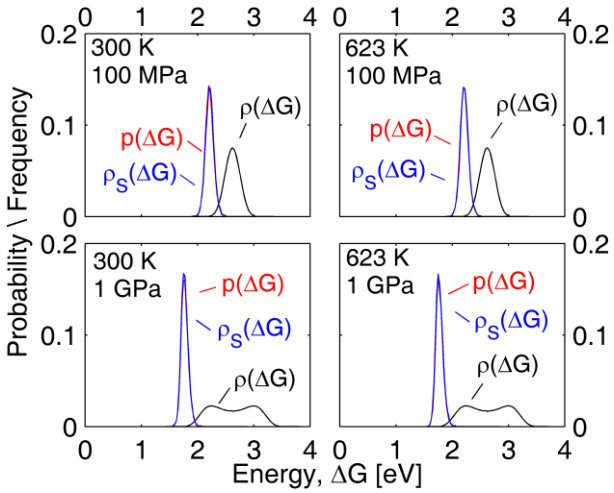

Figure 3.9 Activation energy statistics for a thermally processed glass

Statistics of the density of activation energies, $\rho(\Delta G)$, and the corresponding probability density distribution, $p(\Delta G)$, alongside the density of selected activation energies, $\rho_S(\Delta G)$, for four different simulations with pre-existing stresses (from a 'cooled' structure), carried out under a combination of temperatures, 300 and 623 K, and applied stresses, 100 MPa and 1 GPa.

is that there is almost no change in the distributions from 623 to 300 K at the same applied stress. This means that the distribution of pre-existing stresses swamps out any low energy transitions that might be created after the activation of a previous STZ, which would manifest more prominently in $p(\Delta G)$ at 300 K. In comparing these distributions at the two temperatures, there is little indication that the two simulations should behave differently as a result of the change in temperature.

The correlations in STZ activity for the 'cooled' structure follow the same general trends that were seen in Figure 3.4 for the 'unequilibrated' structure. Figure 3.10(a) and Figure 3.10(b) show the magnitude of $g(r, j)$ in an analogous manner to Figure 3.5; comparison of these figures shows that the magnitudes for the peaks of the TRDFs of the 'cooled' structure are much smaller than the peaks of the 'unequilibrated' structure, although the same general regimes of behavior exist. The fraction of subsequent 'Self STZ Activations', $j = 1$, that occur within one STZ radius can be seen in Figure 3.10(c), where it is noted that the region enclosed by the contours is much smaller than in Figure 3.10(c); the distribution of pre-existing stresses (which are of a similar magnitude to those resulting from any single STZ activation) suppresses local self-

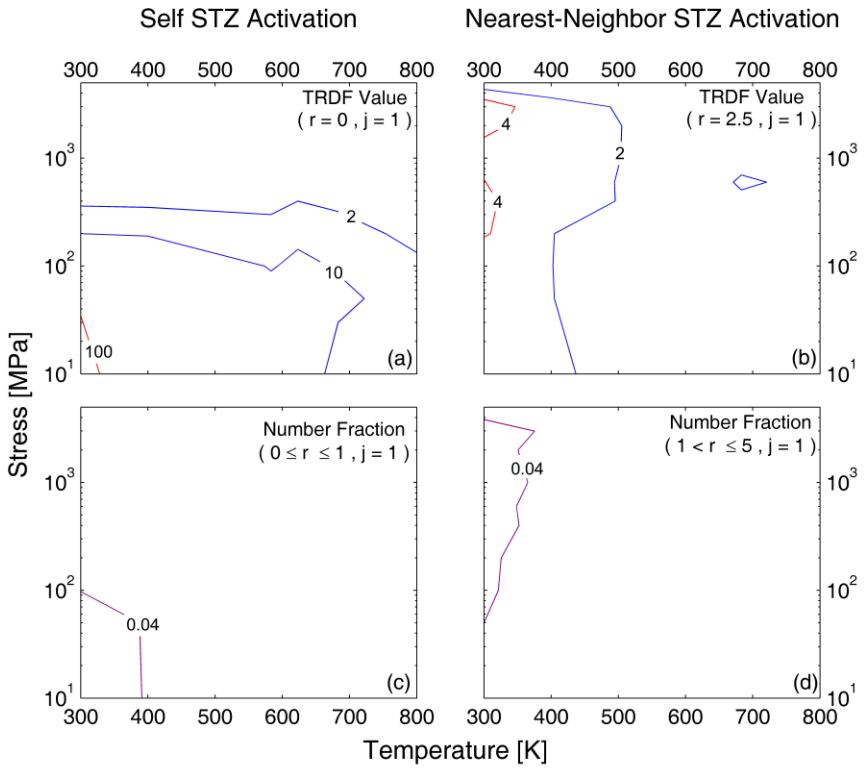

Figure 3.10 Spatial correlation of STZs in a thermally processed glass
Contour plots of several different statistics of STZ correlations over a range of applied stresses and temperatures for a 'cooled' structure with pre-existing stresses: (a) the TRDF values, $g(r, j)$, of 'Self STZ Activation' ($r = 0, j = 1$); (b) $g(r, j)$ of 'Nearest-Neighbor STZ Activation' ($r = 2.5, j = 1$) ; (c) number fraction of subsequent, $j = 1$, 'Self STZ Activation' events within the range $0 \le r \le 1$; and (d) number fraction of subsequent 'Nearest-Neighbor STZ Activation' events within the range $1 < r \le 5$.

activations. Similarly, the fraction of subsequent 'Nearest-Neighbor STZ Activation' events in the range of r = 1 to 5, shown in Figure 3.10(d), reflect a suppressed likelihood of observing correlated STZ activity in the presence of pre-existing stresses. Nevertheless, these correlations do exist at low temperatures in spite of the fact that the activation energy distributions suggest that the simulations should behave identically when deformed at the same stresses, no matter the temperature.

Perhaps the most interesting effect of the pre-existing stresses in the 'cooled' structure is the lack of any macroscopic shear localization or inhomogeneous deformation, as mentioned previously and discussed in chapter 2. There are small pockets of large strain throughout the structure

following deformation, but nothing that would indicate a large degree of localization. In examining the value of the localization index, Γ, over the range of applied stresses and temperatures, it is nearly constant around 0.6, which is why it is not shown here. This lack of inhomogeneous response is consistent with the suppression of correlated STZ activity detailed in Figure 3.10 for the 'cooled' structure; we are now able to conclude that a significant internal stress distribution has a homogenizing influence on deformation at the level of individual STZs, and consequently can suppress the formation of shear bands at larger scales. These results confirm the speculations proposed in chapter 2 for the homogenizing effects of pre-existing stresses which make it difficult to observe perturbations of sufficient size that lead to localization. Similar effects are observed in atomistic simulations where differing pre-existing stress distributions can lead to or inhibit shear localization [55]. The results also rule out another possibility suggested in chapter 2 that the small system size used in these simulations might in and of itself tend to suppress localization in a system with pre-existing perturbations. We believe that in order to observe localization in STZ Dynamics simulations with realistic internal stress distributions, a local structural state variable, such as the free volume, is likely required. Recent results from atomistic simulations also suggest the need for a state-variable beyond the stress state to more accurately account for the localized motion in metallic glasses [91]. This approach is frequently employed in mechanical models of amorphous systems [66], and provides a memory of the state (activation barriers) beyond the redistribution of stresses as is considered here. The development of such a model is left for future work.

3.6. Conclusion

An analysis was performed on STZ Dynamics simulation results from chapter 2 for deformation of a model amorphous metal. The goal of this analysis was to understand how shear transformation zones (STZs) interact with one another at a microscopic level, and how their collective operation combines to effect deformation on a macroscopic level. A statistical analysis of the activation energies of the ensemble of potential STZs and their corresponding probabilities illustrates the influence of applied stress and temperature on the transitions that are most likely to be activated. Specifically, a trend from allowing STZs to shear in a number of directions at high temperatures and low stresses transitions to a trend for STZs to shear in only one direction at low temperature and high applied stress. Finally, a comparison of the

probabilities of the potential transitions with the transitions which were selected during the simulations shows excellent agreement.

An analysis of the distance and time between STZ activations elucidates three general behaviors, identified as 'Nearest-Neighbor', 'Independent' and 'Self' STZ activation. The 'Nearest-Neighbor STZ Activation' behavior occurs at low temperature and high applied stress and indicates that a subsequent STZ activation is likely to occur in the immediate neighborhood of the first. The 'Independent STZ Activation' behavior occurs at high temperatures and any applied stress and indicates that the preference for activating any one of the potential STZs is independent of its location relative to previous activations. Finally, the 'Self STZ Activation' behavior occurs at low temperatures and low stresses and predicts that a subsequent STZ will have to activate in very close proximity to (i.e., atop) the previous STZ to relax the system locally. The temporal components of the STZ correlations are found to be short-lived, always falling off after about five STZ activations.

These three behaviors have been mapped onto an STZ correlation map and matched with their corresponding macroscopic mode of deformation, which are inhomogeneous, homogeneous and elastic, respectively. These regions are also corroborated by macroscopic observations of the degree of homogeneity in the deformation, which we quantify with a 'localization index'. Interestingly, we find that having pre-existing structure in the simulation cell, in the form of a distribution of internal stresses and strains such as are expected for amorphous materials, diminishes the ability of the STZs to communicate with one another through stress redistribution. As a result, both microscopic and macroscopic localization are suppressed in such systems, and true localization (i.e., shear banding) only occurs in systems without pre-existing structure.

4. Insight into Nanoscale Cyclic Strengthening of Metallic Glasses[3]

4.1. Introduction

Thus far, the modeling framework has demonstrated its ability to capture the general mechanical behaviors expected of a metallic glass as well as its ability to resolve the microscopic correlations which lead to macroscopic deformation. Having demonstrated these abilities, the model can now be employed to gain insight into experimentally observed behaviors which lack a clear mechanistic understanding. For example, in the observed nanoscale strengthening of a metallic glass, which was mentioned in section 1.3, certain mechanisms (termed 'microplasticity') were speculated to lead to the nanoscale strengthening, yet no specific evidence was given to confirm their existence [36]. As such, the STZ Dynamics framework is employed to gain insight into the microscopic mechanisms and conditions behind this strengthening. However, a more thorough discussion of the strengthening phenomenon is helpful before getting into an investigation of the details behind this strengthening.

During nanoindentation of a metallic glass the first measurable plastic event reveals itself as a pop-in or rapid excursion into the sample, as discussed in section 1.3. This is illustrated in the inset of Figure 4.2 where the load-displacement curve shows a sudden deviation from the

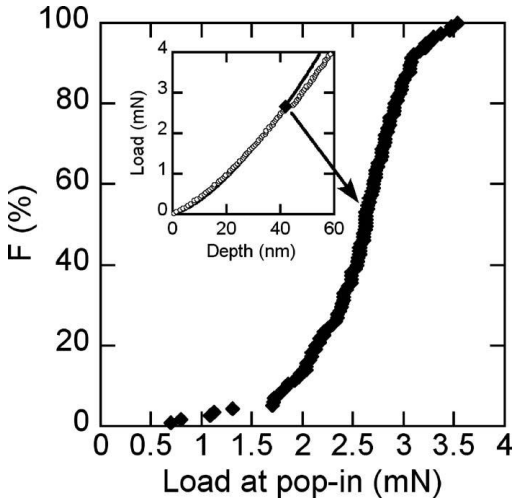

Figure 4.1 Nanoscale strength distribution of a metallic glass
Explain more here Figure taken from Ref. [36].

[3] The contents of this chapter have been published previously as Ref. [92]

Hertzian contact prediction, which is plotted as the solid black line. By performing a large number of nanoindentation tests, and determining the load for the first pop-in of each test, one can generate a nanoscale strength distribution. A distribution of this type is plotted in a cumulative fashion for an iron-based metallic glass, $Fe_{41}Co_7Cr_{15}Mo_{14}C_{15}B_6Y_2$, in Figure 4.2, for tests using a loading rate of 2.5 mN/s and a spherical indenter with a radius of ~1100 nm [36].

To strengthen a glass at the nanoscale, Packard et al. discovered that one can use a load function of the type illustrated in the inset of Figure 4.2(a) [36]. In this load function, the indenter is cycled to a specific load in the elastic regime a number of times before indenting to a load high enough to induce a pop-in or plastic deformation. The resulting load-displacement curve for this load function is illustrated in the Figure 4.2(a). The apparent strengthening can be observed in Figure 4.2(b) where the cumulative distribution of loads for the first pop-in events shifts to higher values with increased numbers of cycles in the elastic regime prior to inducing a pop-in at a higher load. While it can be seen that one cycle seems to sharpen the distribution, no

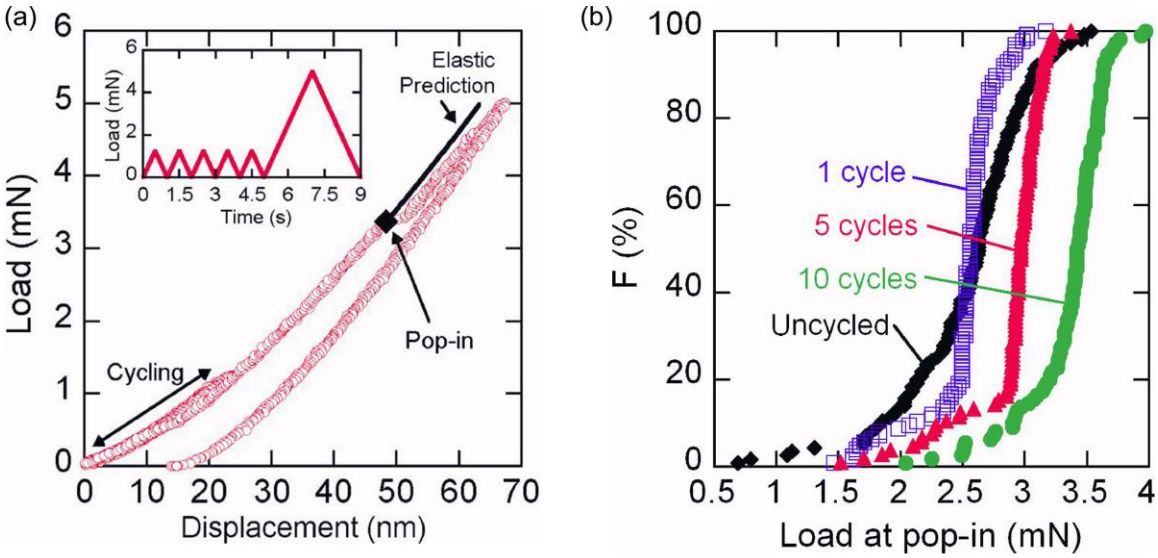

Figure 4.2 Nanoscale strengthening of a metallic glass

(a) Representative load-displacement curve for nanoindentation of a metallic glass when a load function of the type illustrated in the inset to (a) is used. The cyclic loading at low loads nearly perfectly tracks the Hertzian elastic prediction and the first pop-in is observed in the deviation from the Hertzian curve. (b) Cumulative distributions illustrating the loads for the first pop-in event of different types of nanoindentation tests. The uncycled distribution represents the strength distribution for monotonic loading while the cycled distributions represent a load function with the corresponding number of cycles in the elastic regime prior to the first pop-in. The shift in the distributions to higher loads shows the trend of nanoscale strengthening. Figures taken from [36].

significant shift in the distribution to higher loads is detected. However, for five and ten cycles, it can be seen that the increased number of cycles represents a definite shift in the distribution.

Following the discovery of this nanoscale strengthening, a possible origin for the hardening was proposed involving Packard and Schuh's slip-line theory for propagation of a shear band [93]. In this theory, shear bands do not form in the area of the highest shear stress, rather they form along a trajectory where the entire shear band path exceeds the macroscopic yield stress. As such, the area of maximum shear stress can be well in excess of the macroscopic yield stress before any pop-ins are observed. Thus, Packard et al. concluded that this area of high stress during the cycling could induce structural rearrangements, which accumulate over time through to-and-fro STZ activity leading to hardening of a glass, in such a subtle way that it is not observable within the resolution of the instrumentation [36].

Additional nanoindentation tests involving three different glasses, $Pd_{40}Ni_{40}P_{20}$, $Fe_{41}Co_7Cr_{15}Mo_{14}C_{15}B_6Y_2$ and $Pd_{40}Cu_{30}Ni_{10}P_{20}$, confirm the generality of the strengthening phenomenon for metallic glasses while also providing insight into the requirements and characteristics of the strengthening [92]. Specifically, these additional tests indicate that it is the act of cycling, and not just the presence of a stress, which leads to this strengthening. Furthermore, the amplitude of the cycling load must be above a threshold value in order to induce the strengthening. Finally, these tests reveal an apparent saturation in the strengthening of the glass, beyond which further cycling does not provide additional strengthening.

These effects generally align with the mechanism used to described the strengthening observed by Packard et al. [36]. Hardening is indeed caused by cycling, and accumulates gradually, which is in line with local to-and-fro STZ activation that is kinematically irreversible. Assuming a natural bias for STZ activation at the weakest sites in the stressed volume, a back-and-forth cycle would be expected to ratchet local regions of material into lower energy states, so cyclic loading can lead to exhaustion of fertile sites for microplasticity. The saturation of hardening can then be interpreted as the system gradually shaking down to an "ideal glass" configuration of higher structural order than the as-cast material. This may or may not be similar to the configurational state of lower free volume and higher chemical order achieved in well-annealed glasses. It is possible that cycling may cause the glass to reach configurational states inaccessible by thermal relaxation alone (including, possibly, nanocrystallization) and may include anisotropic changes

in the local resistance to plastic flow, delaying shear band formation along the slip lines required by the indenter geometry. Finally, the observation of an apparent threshold cycling amplitude is intuitively reasonable, since sufficiently low applied loads would be unable to trigger STZ activity at all, or at least unable to restructure the glass in the vicinity of the eventual yield shear band.

Thus, all of the experimental observations described above at least qualitatively conform to the proposed mechanism of cyclic microplasticity. However, the above arguments are strictly qualitative. It remains to be established that, in the complex stress field beneath the contact:

(i) Microplasticity, i.e., confined STZ activity (which would tend to redistribute stresses), is energetically plausible,

(ii) Such local STZ activity can occur in a significant volume of material without being globally perceptible in the P-h curve,

(iii) The low-temperature kinetics of STZ activation are commensurate with the timescales of cycling experiments (which span several seconds), and

(iv) To-and-fro STZ activity can lead to hardening.

Resolving these issues requires a model that captures both the complex stress field created by the test geometry (which evolves when local STZ activity accommodates strain and restructures the stress field), and the corresponding global load-displacement response of the indenter tip. To establish the kinetic plausibility of the mechanism requires a model incorporating stress-biased thermal activation of STZs. In the following section, the STZ Dynamics modeling framework developed in chapter 2 is used to simulate indentation in metallic glasses, and applied, specifically, to the case of cyclic loading. Although we cannot make direct predictions pertaining to point (iv), we verify points (i)-(iii) above.

4.2. Nanoindentation model details

The simulated nanoindentation problem addressed here is carried out on a two-dimensional simulation cell comprised of plane-strain elements, with approximate width and height of 100 and 35 nm, along the x- and y-axes respectively. The indenter is modeled as a rigid surface with a tip radius of 40 nm and in all cases the indentation displacement rate is set at 1 nm/s along the

y-direction[4]. The bottom edge of the cell (along x) is fixed, rendering the geometry equivalent to that of a film atop a substrate of infinite stiffness. Periodic boundary conditions are applied at the lateral edges (along y). The top surface (along x) is free, but subject to the constraint of frictionless hard contact with the indenter. Similar boundary conditions and test geometries have been employed for simulated nanoindentation by molecular dynamics [53]. The material and geometric STZ properties employed for these simulations are the same as those used in chapters 2 and 3, as taken from Table 1.

The KMC algorithm of section 2.2.2 has been slightly adapted to more efficiently simulate nanoindentation, during which the stress state (and thus the STZ activation rate) varies quite dramatically. Specifically, we enforce here a maximum elapsed time per KMC step of 5 ms. If during that time the KMC algorithm predicts a transition, it is allowed; otherwise the STZ activation is suppressed and the system evolves by 5 ms. In either case the indenter tip is moved by an appropriate distance to effect a constant displacement rate.

For purposes of comparison with experiment, it is important to note that the indentation rate used here (1 nm/s) is closely matched to that in the experiments (~5-40 nm/s), and many orders of magnitude slower than typically used in atomistic simulations of indentation (~5.4×10^8 nm/s [53]). In terms of micromechanics and kinetics of STZ activity, we can therefore expect to make reasonable qualitative comparisons with the experiments. However, we emphasize that a quantitative comparison between model and experiment is not possible or appropriate. The simulations employ a model glass and test conditions that are somewhat different from the experiments (displacement- vs. load-controlled, plane strain vs. axisymmetric). More importantly, the present STZ Dynamics model does not specifically incorporate a structural state variable (such as free volume or an order parameter). As such, the model cannot explore the complex reaction pathways that lead to intrinsic structural hardening or softening, such as those apparently sampled in the experiments. Thus, the model is not capable of directly modeling cyclic hardening, but it may be used to validate the concept of microplasticity upon cyclic loading. We limit our attention in what follows to focus on the latter aspects of the problem (surrounding the potential for microplasticity) that are accessible with the present model.

[4] The system size and tip radius were found to have a negligible effect on the overall nature of deformation by running a monotonic loading test using an indenter radius of 100 nm and a system size of 250 by 100 nm (data not shown).

4.3. Monotonic loading

To begin, we consider conventional monotonic nanoindentation tests. As a baseline for our subsequent analysis, we first conduct an ideal elastic indentation, i.e., one in which the energy barrier for STZ activation was increased to infinity, and thus plasticity was suppressed. The P-h curve resulting from this simulation is shown in Figure 4.3, as a solid black line. This curve also matches the expectations of the Hertzian contact solution (which, for the plane-strain cylinder-on-plate geometry, does not have a closed analytical form [94]). When the same simulation is conducted with STZs allowed to activate, the result is shown in Figure 4.3 as the blue data points; the response initially follows the elastic curve exactly, but at a depth of about 2 nm begins to noticeably depart from the elastic curve as plastic flow sets in.

Snapshots showing a portion of the simulation cell during the indentation are provided in the bottom panel of Figure 4.3, corresponding to the marks 'A', 'B' and 'C' on the P-h curve. In each of these snapshots, a red solid line denotes the outer envelope of material in which the local deviatoric (von Mises) stress exceeds the nominal yield stress of the model glass (taken as 3.27 GPa from pure shear simulations at 10^{-3} s^{-1} in chapter 2). Similarly, the load at which the yield

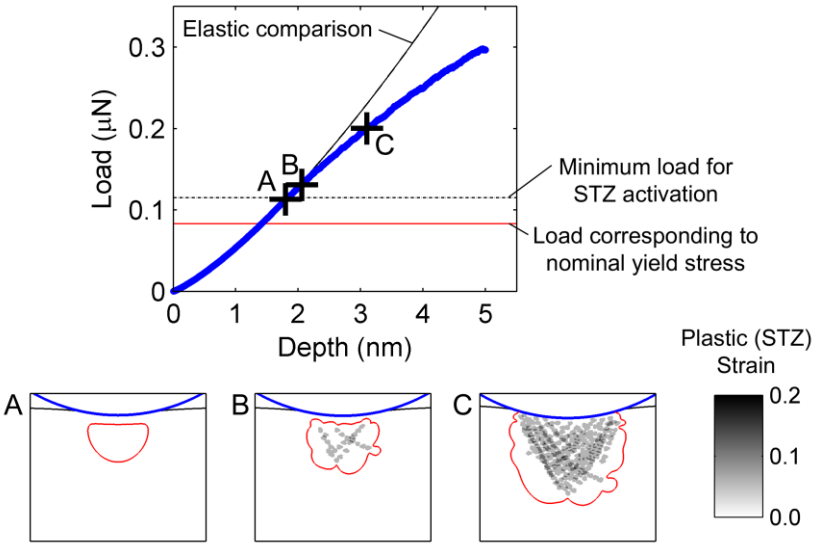

Figure 4.3 Simulated monotonic nanoindentation of a metallic glass

The graph shows the load-displacement curve for a single monotonic indentation test, in comparison with results for a purely elastic contact for comparison. Snapshots of the system during the simulation are provided below the graph as marked by 'A', 'B' and 'C'. The red contour on the snapshots shows the region of material that has exceeded the yield stress, while the gray regions denote the operation of STZs.

stress is first reached at any point beneath the contact is marked by the solid horizontal red line on the P-h curve. It is interesting to observe that high deviatoric stress is not necessarily correlated to the activation of STZs, as there is a significant regime at loads where some portion of the material reaches the yield stress, but before the first STZ activity is observed. In this regime, the stress field still matches the Hertzian elastic prediction exactly and therefore the yield envelope is symmetric as in panel 'A'. It is only at a somewhat higher load that STZs activate, with local spatial correlations along slip lines (panel 'B'). At this point, the stress and strain field is no longer simple, being perturbed and redistributed by virtue of the STZ activity, and the envelope in which the nominal yield stress is exceeded is asymmetric and irregular as a result. An important point to note, however, is that at 'B', despite the activity of numerous STZs and the appreciable volume of material above the nominal yield stress, the global P-h curve is still in excellent agreement with the elastic curve. Significantly beyond point 'B', the departure of the response from the ideal elastic curve is unambiguous, and the extent of plastic deformation is large (panel 'C'). In this regime the distribution of plastic strain beneath the point of contact is quite reminiscent of that expected from slip-line field theory, as also seen in experiments on metallic glasses [28, 95].

4.4. Cyclic loading

We now turn our attention to cyclic indentation simulations, which were conducted at displacement amplitudes of 1.2, 1.6, 2.0, 2.4, and 2.8 nm. The P-h curves from these simulations are shown in Figure 4.4. As expected based on the above discussion, at low amplitudes of 1.2 and 1.6 nm, the stress levels achieved are below that necessary to trigger STZ activity on the time scales of the test, and the response is perfectly elastic. On the other hand, for the largest amplitude of 2.8 nm, copious STZ activity occurs below the indenter, and measurable dissipation occurs after the first cycle. Obvious plastic (residual) displacement is accumulated after the first cycle, with subsequent cycles appearing essentially perfectly elastic. At intermediate displacement amplitudes of 2.0 and 2.4 nm, we see the interesting behavior of most direct relevance to this work: in this range we see significant STZ activity beneath the indenter, but relatively little permanent deflection in the P-h curves. If we assign a displacement resolution similar to that in nanoindentation (~0.2 nm, twice the width of the data points in Figure 4.4), these simulations appear in the P-h curves as essentially perfectly elastic. In fact, for the 2.0 nm displacement amplitude, with a resolution (and data point size) of 0.1 nm, we can detect no

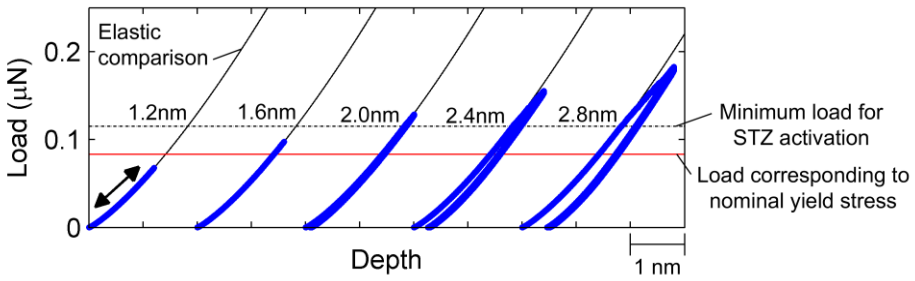

Figure 4.4 Load-depth curves for simulated cyclic nanoindentation

The limiting amplitude of the cycling depth is marked by each curve, ranging from 1.2 – 2.8 nm. The elastic reference is plotted with each cycling simulation for comparison. Cycling at depths where the load does not reach the minimum load for STZ activation, 1.2 and 1.6 nm, results in a perfectly elastic material response. Cycling above the minimum load for STZ activation leads to plasticity through STZ activity in all cases, 2.0 – 2.8 nm, although the hysteresis in the load-depth curve is not immediately apparent in all cases.

hysteresis or dissipation in the P-h curve in Figure 4.4. However, despite the appearance of elastic conditions, Figure 4.5 shows that in these two cases, there is significant STZ activity beneath the indenter.

The behavior captured in Figure 4.4 and Figure 4.5, for displacement amplitudes of ~2.0 nm, corresponds to the speculative "microplasticity" that is believed to occur during cyclic indentation experiments, as originally proposed in Ref. [36]. These simulations confirm that under the mechanical load of an indenter, and at time scales relevant to the experiments, it is plausible that the applied stress field significantly exceeds the yield stress of the material in local regions beneath the indenter, and leads to local microplastic events sufficiently small and localized so as to be transparent to the global P-h measurement. What is more, these simulations reveal that this STZ activity can occur progressively over the course of several load cycles; close inspection of Figure 4.5 reveals that at 2.0 nm amplitude, new STZ activity occurs on cycles 1, 3, and 5, while at 2.4 nm amplitude there is evolution on each and every cycle. In addition, STZ activations are observed on both the downward indentation into the sample as well as during the retraction of the tip from the sample in response to the local and evolving stress landscape.

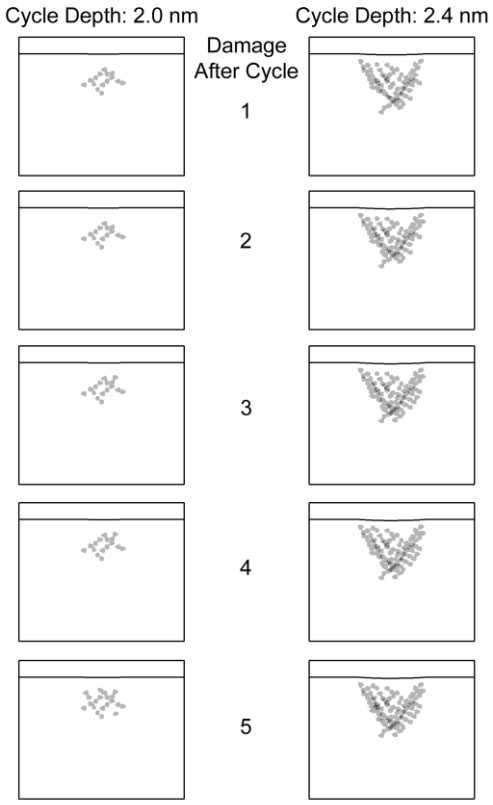

Figure 4.5 Snapshots of the indentation damage during cycling of a glass

The snapshots show a portion of the 2.0 and 2.4 nm cycled systems below the surface after each of the five cycles, illustrating the progressive nature of the structural change. The gray regions show the local plastic strains accumulated by STZ activation. In addition, it can be seen that the sample surface remains relatively smooth in spite of the fact that significant plastic structural change has occurred below the surface.

4.5. Conclusion

At least qualitatively, the observations from our simulations line up well with those from the experimental work, and most importantly, they validate the plausibility of microplastic structural rearrangements. Cycling can indeed cause undetected microplasticity, and structural change via STZ activation can occur progressively over the course of several load cycles. As already noted earlier, the present model does not include a mechanism for hardening in the region affected by microplasticity. However, we note that the amount of material deformed on cycling is fairly significant, and is located in the regions that experience high stresses. If this material has been locally "aged", "annealed", or otherwise restructured by virtue of local STZ activity, then this affected volume could be stiffer or stronger than the surrounding material. Upon further loading,

it could preferentially bear load, shedding it from the virgin glass, or directly impede the formation of a shear band attempting to traverse it. While many details of this cyclic hardening phenomenon remain to be clarified, the present simulations support the notion of microplastic structural rearrangement as a root cause of it.

The ability of the STZ Dynamics framework to provide this level of insight into the behavior of a metallic glass signifies its utility as a modeling tool. Specifically, the simulations were able to provide detailed information about the structure of the glass during deformation, while preserving the fundamental physics of microscopic deformation. Furthermore, the simulations were able to capture the behavior at experimentally relevant time and length-scales.

5. Development and validation of 3D STZ Dynamics framework

5.1. Introduction

While the utility of the STZ Dynamics method has been illustrated in the previous chapters, all the implementations discussed above have been limited to 2D in-plane simulations. However, the complexities of real experiments cannot always be captured by 2D models. This chapter extends the STZ Dynamics modeling framework to 3D to provide insight into the mechanical behavior of an amorphous metal on under fully three-dimensional, experimentally relevant conditions.

In what follows, we detail the development of the 3D model and present results of simulated tensile creep tests over a range of stresses and temperatures. The results are compared against the high temperature rheology and low temperature shear localization expected of a metallic glass and the general response of the modeling framework is compiled into a deformation map. A detailed study of the localization for a model in tension provides insight into the nucleation, propagation and growth of a shear band at low temperatures. Finally, a simulated nanoindentation test in 3D is presented to show the flexibility of the modeling framework.

5.2. Modeling Framework

The three-dimensional STZ Dynamics framework is comprised of four essential parts: the STZ representation, the STZ activation rate, the KMC algorithm and the model parameters. The following sections detail each of these four components and their incorporation into the overall framework.

5.2.1. Shear Transformation Zone Representation

Similar to the 2D framework, the 3D framework models the mechanical behavior of an amorphous metal as a linear elastic continuum with the STZ acting as the sole mechanism for plasticity. In 3D, we coarse-grain the system and replace a collection of atoms, such as that represented in Figure 5.1(a), with a finite-element mesh, an illustration of which is shown in Figure 5.1(b). To properly define an STZ based on features of a 3D mesh we insist on the same requirements as those listed in section 2.2.1, which are (i) conformity to the generally equiaxed shape of an STZ, (ii) accurate resolution of the stress and strain distributions associated with the STZ shearing behavior and (iii) overlapping of STZs to mimic atomistic behavior.

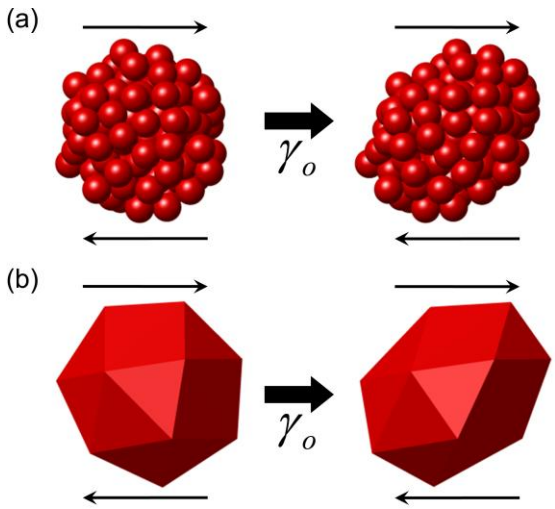

Figure 5.1 Representation of STZ in three dimensions
(a) Atomistic and (b) finite element representations of a 3D STZ before and after an increment of strain, γ_o.

From among the common finite-element mesh types used in 3D (quadrilateral, tetrahedral and wedge-shaped elements or combinations thereof), we find that a collection of 20-30 tetrahedral elements that all share one common node provides a consistent approximately spherical STZ representation (see Figure 5.1(b)) when an exclusively tetrahedral mesh is used (and is free from large distortions). We note that in this definition, STZs may overlap, which is consistent with individual atoms having the ability to shear with numerous potential STZs.

To assess the accuracy of resolving the stress and strain distributions, just as in section 2.2.3 we examine the convergence of the strain energy associated with the shearing of an STZ represented by tetrahedral elements which share a common node. We again compare to the Eshelby inclusion problem [9, 18] and in FEA solutions, it is found that the elastic strain energy of the linear and quadratic tetrahedral element-based STZs, with one and four integration points per element, respectively have 30% and 2% error, when compared with the Eshelby solution. As a result of the higher accuracy provided by the quadratic solution, we employ quadratic tetrahedral elements which share a common node to represent potential STZs in 3D.

5.2.2. STZ Activation Rate

Generalization of the activation rate given in Equation 2.2 to 3D requires the identification and description of all possible shear planes and directions, or shear states, by which an STZ may

evolve and which may contribute to the overall STZ activation rate. This results in the following generalized 3D STZ activation rate

$$\dot{s} = \nu_o \cdot \exp\left(-\frac{\Delta F}{kT}\right) \iiint_{g \in G} \exp\left(-\frac{\tau(\sigma, g) \cdot \gamma_o \cdot \Omega_o}{2kT}\right) dg . \tag{5.1}$$

where σ represents the local stress state and $\tau(\sigma, g)$ represents the shear stress for the shear state labeled *g*, belonging to the set of all possible shear states, *G*. Equation 5.1 is similar in form to the STZ activation rate given by Equation 2.5 for shearing an STZ in 2D, with the exception that the integral includes the additional degrees of freedom for the third dimension. For the purposes of these simulations, the evaluation of the integral in Equation 5.1 must be computationally efficient; we take the approach of tabulating it. The following paragraphs describe our procedure for the accurate and efficient evaluation and tabulation of Equation 5.1.

First, we identify the symmetry present in the space of shear states to ensure that no particular shear state *g* is double-counted, missed or given unequal weight in the evaluation of Equation 5.1. This is accomplished by defining a representative volume element with a non-zero component of the shear stress, corresponding to a stress state associated with the shearing of an STZ. For the purposes of this derivation we arbitrarily select τ_{12} for our shearing stress (without loss of generality) and illustrate this stress state in Figure 5.2. To the right of the stress state in Figure 5.2, we show all symmetrically equivalent coordinate systems for this shear stress, of which there are four (i.e., the representation of the τ_{12} shear stress in any of these coordinate

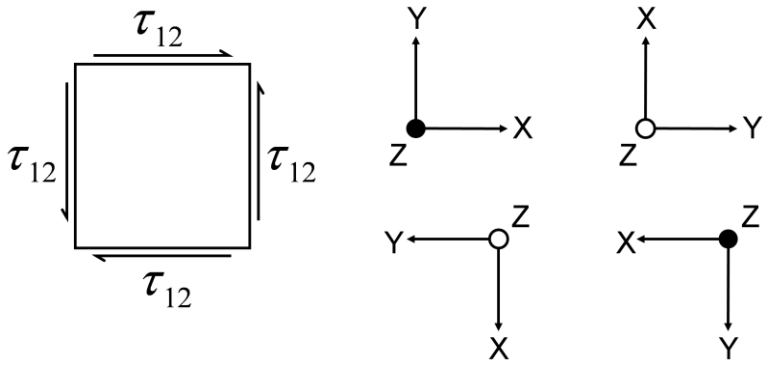

Figure 5.2 Symmetry of representative three-dimensional STZ shear state
A representative stress state from which the STZ activation rate can be calculated is shown alongside all coordinate systems for which the shear stress, τ_{12}, is mathematically identical.

systems is mathematically identical). The symmetry operators, or point operators, relating these four coordinate systems are

$$S = \{E, C_{2z}, C_{2a}, C_{2b}\}. \tag{5.2}$$

In this set, *E* represents the identity operator, and the other three point operators are given by rotations of π about the $[001]$, $[110]$ and $[1\bar{1}0]$ axes, respectively.

The different shear states identified by the variable *g* represent the coordinate transformation of a given stress state σ, into another coordinate frame where the shear stress τ_{12} can be calculated for its contribution to the overall STZ activation rate. For reasons of simplicity and efficiency, we set the initial stress state, σ, to be given only by the principal values, $(\sigma_1, \sigma_2, \sigma_3)$, in the principal frame and calculate τ_{12} in the transformed coordinate system.

The coordinate transformations identified by *g* can be effected using any of several common rotation parameterizations, including Euler angles, quaternions, axis-angle parameters and Rodrigues vectors [96, 97]. In 2D, a single Euler angle can be used easily (see section 2.2.2), but in 3D we find it more convenient to work in Rodrigues vectors, which are scaled vector representations of an axis-angle coordinate transformation. The vector components are defined as

$$r_i = \tan\left(\frac{\omega}{2}\right) \cdot n_i \tag{5.3}$$

for a rotation of ω about an axis with vector components n_i, as illustrated in Figure 5.3(a). Because of the divergence of the tangent, rotation space as represented by a Rodrigues vector is infinite in all three dimensions. However, the application of the symmetry operators in Equation 5.2 gives a reduced set of coordinate transformations, *G*, that identify the unique shear states for τ_{12}; these fall within a rotated cube in Rodrigues space, as illustrated in Figure 5.3(b). This cube is centered on the origin, has an edge length of 2 and is rotated by *π/4* about the r_3-axis.

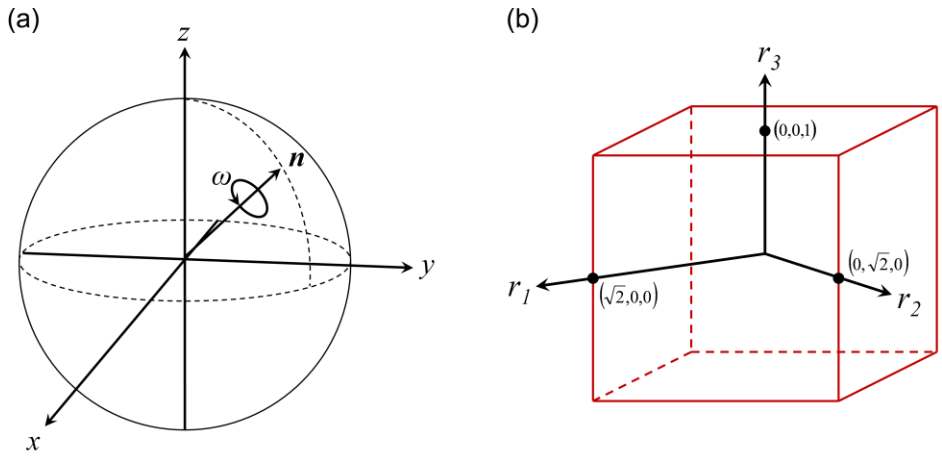

Figure 5.3 Parameterization tools for three-dimensional STZ activation rate (a) Representation of an axis-angle rotation, on which the scaled Rodrigues vector is based. (b) Representation of the reduced Rodrigues space representing all unique shear states, *G*, contributing to the STZ activation rate.

The integral in Equation 5.1 for coordinate transformations, *g*, represented by Rodrigues vectors becomes

$$\dot{s} = \nu_o \exp\left(-\frac{\Delta F}{kT}\right)\iiint_G \exp\left(\frac{\tau(\sigma, r_1, r_2, r_3)\cdot\gamma_o\Omega_o}{2kT}\right)\left[\frac{4}{\pi^2\left(1+r_1^2+r_2^2+r_3^2\right)^2}\right]dr_1 dr_2 dr_3 \qquad (5.4)$$

where τ is the shear stress for the shear state transformed by the Rodrigues vector r_i and the bracketed term in the integral which follows the exponential is the required integration factor for the Rodrigues parameterization [98]. For simplicity, τ is given as a function of the axis-angle parameters, (ω, n_i), of the Rodrigues vector

$$\begin{aligned}\tau(\sigma,\omega,n_i) = {} & \sigma_1\cdot\left[n_1^2\cdot(1-\cos\omega)+\cos\omega\right]\cdot\left[n_1n_2\cdot(1-\cos\omega)-n_3\cdot\sin\omega\right] \\ & +\sigma_2\cdot\left[n_2^2\cdot(1-\cos\omega)+\cos\omega\right]\cdot\left[n_1n_2\cdot(1-\cos\omega)+n_3\cdot\sin\omega\right] \\ & +\sigma_3\cdot\left[n_2n_3\cdot(1-\cos\omega)+n_1\cdot\sin\omega\right]\cdot\left[n_1n_3\cdot(1-\cos\omega)-n_2\cdot\sin\omega\right]\end{aligned} \qquad (5.5)$$

Together, Eqs. 5.4 and 5.5 give the STZ activation rate for shearing an STZ in 3D.

The integral in Equation 5.4 can be shown to be a function of only two independent variables, $\dot{s}\left(\frac{\sigma_1\cdot\gamma_o\Omega_o}{T}, \frac{\sigma_2\cdot\gamma_o\Omega_o}{T}\right)$, by scaling the stress as shown and taking advantage of the fact that the activation rate is only dependent upon the deviatoric component of the stress where

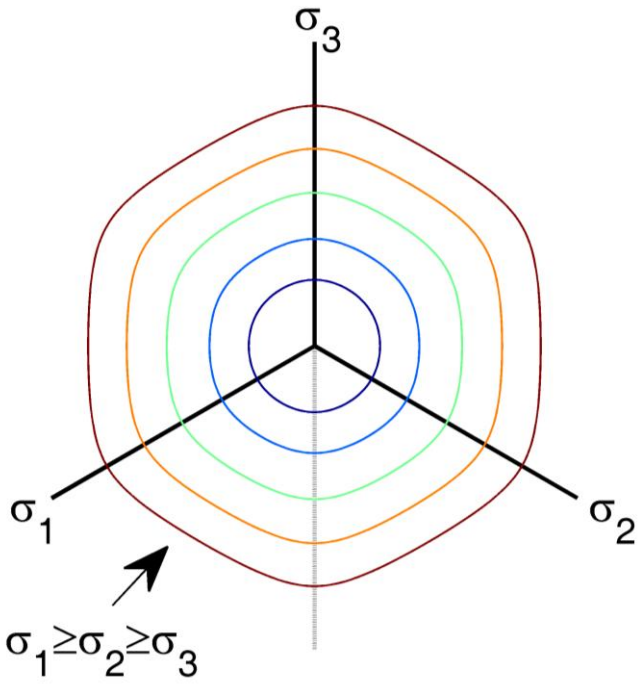

Figure 5.4 Contour of constant STZ Activation rate
The contours are viewed down the 111-axis in the principal stress space. The region between the σ_1 axis and the shaded line represent the ordered principal values, $\sigma_1 \geq \sigma_2 \geq \sigma_3$, where the STZ activation rate is tabulated.

$\sigma_3 = f(\sigma_1, \sigma_2)$. This is illustrated in Figure 5.4, where contours of constant STZ activation rate are plotted in the π-plane, $\sigma_3 = -\sigma_1 - \sigma_2$, as viewed down the 111-axis. As is immediately obvious in Figure 5.4, six-fold symmetry is present in the contours of $\dot{s}$ because of the symmetry in the deviatoric stress as a function of the principal stress values, further reducing the region for tabulation of $\dot{s}$ to where $\sigma_1 \geq \sigma_2 \geq \sigma_3$.

The shapes of the contours in Figure 5.4 provide insight into the behavior of the STZ activation rate as a function of the applied stress. The smaller contours take the shape of a circle, indicating that at low scaled stresses, the different shear states contribute equally to the activation rate (analogous to von Mises yielding, which considers the contribution of all shear stresses and gives a circular shape to the yield criterion in the π-plane). At larger scaled stresses the contours transition from circular to hexagonally-symmetric, and eventually (not shown) to a nearly perfect regular hexagon. This suggests that at a higher scaled stresses activity on a single shear plane

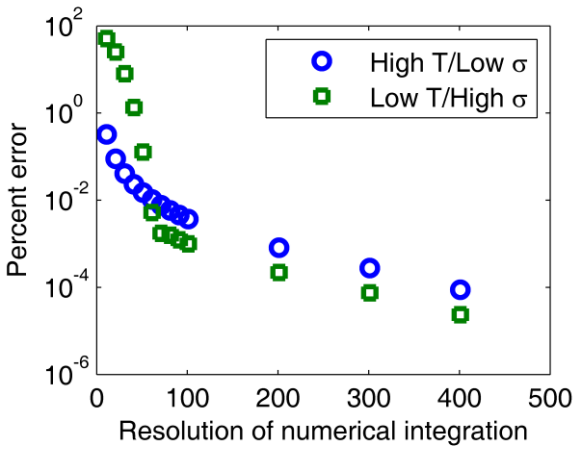

Figure 5.5 Convergence of numerical integration of STZ activation rate

The convergence of the STZ activation rate is shown by the reduced error with increased resolution along the edge of *G* for numerical integration of Equation 5.4.

dominates the activation rate (more akin to Tresca yielding). For the simulations in this work, the conditions are such that the activation rate is usually calculated at larger scaled stresses where the activation rate is dominated by specific shear planes.

As we are not aware of an analytical solution for the integral in Equation 5.4, we ensure convergence and accuracy of numerical integration by increasing the number of evaluations within *G*. Figure 5.5 plots the percent error relative to the converged value as a function of the number of evaluations along each edge of *G* in Rodrigues space for the two extreme cases of high temperature/low stress and low temperature/high stress. In both cases, the error quickly falls below 0.01%, showing that extreme refinement of the numerical integration is not required. For efficiency, a resolution of 101 x 101 x 101 (just more than one million equal volume partitions) is used in our evaluation of the integral in Equation 5.4.

The STZ activation rate has been tabulated over the two independent variables in the π-plane where $\sigma_1 \geq \sigma_2 \geq \sigma_3$ for 512 by 4096 entries. During the simulations, the STZ activation rate can be interpolated from the tabulated data with less than 20 queries on the table. For any given value obtained from the table, the error is consistently less than 0.1% when compared with the value obtained by high resolution numerical integration.

Because Rodrigues space is non-uniformly populated with rotations (see the integration factor in Equation 5.4), our approach actually represents a linear partition scheme for a non-linear space.

While the integral is calculated accurately, a scheme for equal probability and equal volume partitions is not immediately obvious. However, with the 101^3 partitioning scheme the maximum and minimum misorientation angles between any two coordinate transformations are 2.27° and 0.81°, respectively. Given this small degree of misorientation between possible coordinate transformations and the fact that the integration factor in Equation 5.4 accounts for the non-linearity of the space, we judge that the system is not significantly limited by the manner of partitioning and integration of the STZ activation rate evaluated in Rodrigues space.

5.2.3. Kinetic Monte Carlo Algorithm

To employ the KMC algorithm in the 3D framework, we adhere to the same steps as those laid out in section 2.2.2, except that specific adaptations must be made for the selection and application of the shear state to the selected STZ based on the STZ activation rate in 3D. For the selection of the shear state, it must be recalled from section 2.2.2 that one must define the overlap or residual of the random number used to select a given STZ, given here as η'. The activation rate is then integrated for the selected STZ until the following equality is true

$$\eta' = \frac{1}{\dot{s}_k} \cdot \nu_o \exp\left(-\frac{\Delta F}{kT}\right) \iiint \exp\left(\frac{\tau(\sigma, r_1, r_2, r_3) \cdot \gamma_o \Omega_o}{2kT}\right) \left[\frac{4}{\pi^2\left(1 + r_1^2 + r_2^2 + r_3^2\right)^2}\right] dr_1 dr_2 dr_3 \tag{5.6}$$

where $\dot{s}_k$ is the total activation rate for the selected STZ. The limits of the integral in Rodrigues space which satisfy the equality in Equation 5.6 can then be used to determine the shear state for the selected STZ. For the numerical integration of Equation 5.6, this is analogous to summing the Rodrigues partitions of *G* with the appropriate integration factor until the equality becomes true; the partition at which this occurs represents the shear state for the transition of the selected STZ.

The final adaptation of the KMC steps outlined in section 2.2.2 involves the calculation of the actual strains to be applied to the selected STZ, which must be given in the sample coordinate frame. Therefore, the strain state in the coordinate frame of the selected shear state corresponding to the τ_{12} shear stress used to calculate the STZ activation rate,

$$e'' = \begin{bmatrix} 0 & \frac{1}{2}\gamma_o & 0 \\ \frac{1}{2}\gamma_o & 0 & 0 \\ 0 & 0 & 0 \end{bmatrix}, \tag{5.7}$$

must be transformed. However, the strain in Equation 5.7 must first be transformed into the intermediate coordinate system of the principal stress state, from which the STZ activation rate was calculated, after which it can be transformed into the sample coordinate frame where it will be applied. Using the coordinate transformation for the selected shear state, *g*, and the Eigenvectors of the principal stress state, *V*, the strain to be applied to the selected STZ can be given in the sample coordinate frame as

$$e = Vg^T e'' g V^T . \tag{5.8}$$

Similar to the 2D framework, the stochastic nature of the KMC algorithm is manifested by the probabilities for the different events, where STZs with higher stress will have a higher STZ activation rate resulting in a higher probability of being selected. The same principle applies to the different potential shear states, where different shear states will have varying magnitudes of shear stress; shear states with higher shear stress will have a larger contribution to the STZ activation rate and therefore a higher probability of being selected.

To illustrate the selection of a shear state, we examine an STZ within a material under a large uniaxial tensile stress along the x-axis. While all possible shear states have a finite probability of being selected, we focus our attention on a representative set of shear states with the highest probabilities of being selected. Figure 5.6 plots the STZ strain components in the sample coordinate frame which would result if any of these highest probability shear states were to be selected. It can be seen that the ε_{11} strain component is nearly constant at 0.05, indicating that the high probability shear states will achieve the maximum extension in the direction of the tensile stress for the strain increment of $\gamma_o = 0.1$. The ε_{22} strain component varies between 0 and -0.025 while the ε_{33} component varies between -0.025 and -0.05; these are out of phase with each other by π radians while the ε_{23} component is out of phase by $\pm\pi$ radians and varies between 0.025 and -0.025. This results from the fact that the applied shear states are volume preserving shear distortions, such that an expansion in one direction requires a contraction in a

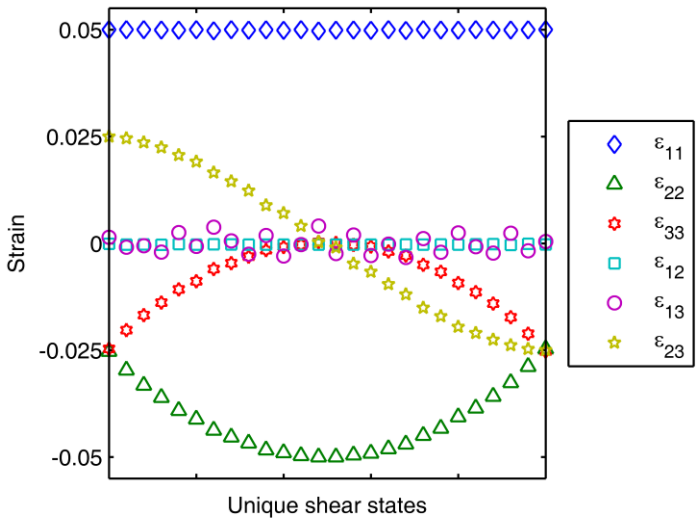

Figure 5.6 Possible strain states of an STZ activated in uniaxial tension
The plastic STZ strain components are associated with a representative set of high probability transitions for an STZ under uniaxial tension.

perpendicular direction. The last two shear components of the strain, ε_{12} and ε_{13}, both vary around zero with values that also satisfy the volume-preserving shear-distortion requirement.

We note that the representative set of transitions examined here does not include all shear states which allow maximum extension in the direction of the uniaxial stress; specifically it is missing the states where ε_{22} varies between -0.025 and -0.05 and ε_{33} varies between 0 and -0.025. The reason these states do not show up in the representative set of highest probability shear states is that their individual probability of being selected is much lower. This lower probability results from the nonlinearity of Rodrigues space, where shear state partitions of G closer to the origin represent a larger population of shear states and therefore have higher activation rates than shear state partitions at a large distance from the origin. However, what the shear state partitions at a large distance from the origin lack in local activation rates, they make up for in their numbers. In fact, it can be shown that the other population of shear states ($-0.025 \le \varepsilon_{22} \le -0.05$ and $0 \le \varepsilon_{33} \le -0.025$), not shown in Figure 5.6, have an equal net probability of being selected as do the set of shear states shown in Figure 5.6.

Therefore the STZs that maximize the extension in the direction of the tensile stress are preferred, while, in the absence of any other stresses, contraction can occur in any direction

normal to the tensile stress. This is exactly what is expected from an STZ embedded in a material under uniaxial tension, and illustrates that the KMC algorithm is capable of appropriately selecting the shear states for activating an STZ in 3D.

5.2.4. Model Parameters

In general, the same material parameters for Vitreloy 1 used in the 2D STZ Dynamics simulations are used here (see Table 1). However, the intrinsic barrier height, ΔF, and STZ volume, Ω_o, have been refitted from experimental data of Vitreloy 1 [22, 99] using a least-squares fit of Equation 1.2, but which has been adapted for uniaxial tension, the mathematical definition of which will be given in the following section. From the fit of the experimental data, these values are obtained as $\Delta F(T) = 0.822 \times 10^{-29}[\text{J/Pa}] * \mu(T)$ and $\Omega_o = 2.0[\text{nm}^3]$.

5.3. General STZ Dynamics Response

To test the general response of the 3D STZ Dynamics framework, we perform a number of simulated uniaxial constant-stress tensile creep tests on cylindrical simulation cells with a diameter of 10 nm and a height of 20 nm. We consider 6 equally spaced temperatures in the range of 300 – 800 K and 7 magnitudes of the tensile stress in the range of 100 MPa – 4 GPa. The boundary conditions for these tests include fixing the bottom surface in the loading direction (z-axis) and allowing the top surface to move vertically as a plane. All the nodes on the top and bottom surfaces are allowed to move radially in the r-θ plane.

5.3.1. High temperature model response

Two datasets, representative of the high temperature tensile test simulations, are shown in Figure 5.7 for one simulation at 700 K and 600 MPa and another at 800 K and 300 MPa. Figure 5.7 shows the evolution of the simulations under the constant applied tensile stress by presenting the uniaxial strain as a function of the elapsed time, along with snapshots of the systems at specific intervals during the simulation. The upper row of snapshots show a perspective view of the outside of the cells with the plastic strains accumulated through STZ activity shaded in red according to the legend, while the lower row shows a semi-transparent profile view of the cells such that STZ activity can be seen through the thickness. The transient response typical of the 2D STZ Dynamics simulations can be seen in the strain-time graph in Figure 5.7(a), where this transient response is common for STZ Dynamics model systems without any pre-existing stress

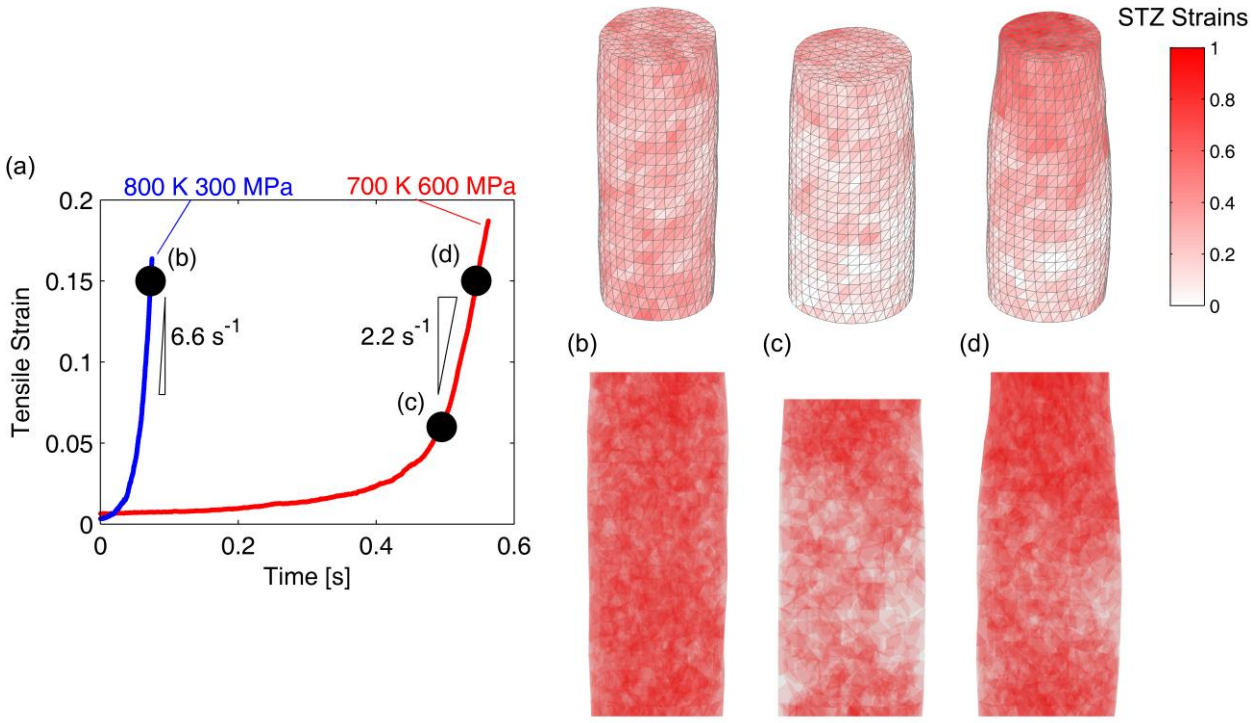

Figure 5.7 Representative high temperature model response

This high temperature response is presented for two simulations, both under a constant tensile stress; one at 700 K and 600 MPa and another at 800 K 300 MPa. (a) Strain-time evolution during the course of the simulations with the strain rate measured in the steady state. A snapshots of the 800 K and 300 MPa system at 15% strain is provided in (b) while snapshots of the 700 K and 600 MPa system are provided at 5 and 15% in (c) and (d), respectively. The upper row of snapshots gives a perspective view of the outside of the simulation cells with the plastic STZ strains shaded according to the legend. The lower row of snapshots provides a semi-transparent profile view of the cells for viewing through the thickness.

distributions. In this transient region, the stress distribution is developed to the point where more steady-state accumulation of strain can be observed.

A snapshot of the simulation at 800 K and 300 MPa at a strain of 15% is plotted in Figure 5.7(b) where it can be seen that in the steady-state regime, the model exhibits stable homogeneous flow with a strain rate of 6.6 s^{-1}. In this case, the homogeneous flow is due to a fairly uniform distribution of STZ activity as can be seen in the semi-transparent view of Figure 5.7(b). For the simulation at 700 K and 600 MPa, however, it can be seen that after the transient region the sample begins to neck, the beginnings of which can be seen in Figure 5.7(c) at 5% strain in the semi-transparent profile view. The faster accumulation of strain in this case, steady at about 2.2 s^{-1}, is due to unstable inhomogeneous flow, exhibited through necking. This necking becomes

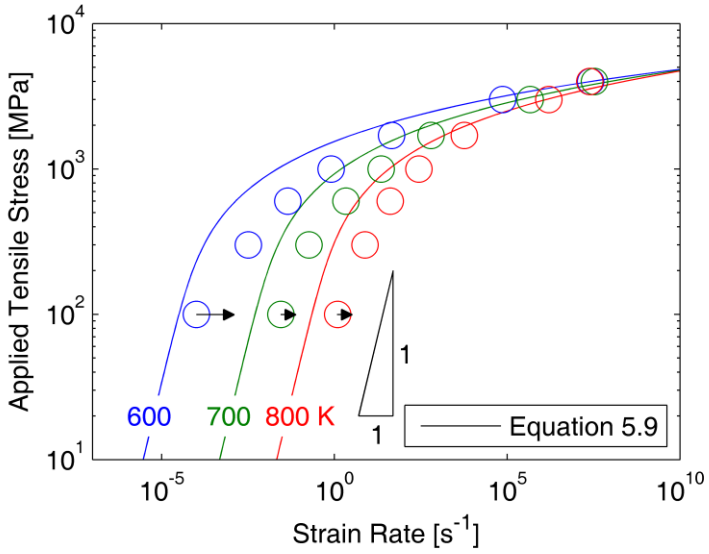

Figure 5.8 High temperature rheological response

The rheological response illustrates the trends in the steady-state strain rates measured from the different simulations. Simulations which did not yet reach a steady state include arrows to illustrate the shift to the expected steady state strain rate. The data are plotted alongside the predicted rates for the classic constitutive model (Equation 5.9) commonly used to describe experimental data.

more pronounced as the simulation evolves, a snapshot of which is provided at 15% in Figure 5.7(d), and is due to more localized STZ activity, which can be seen in the semi-transparent profile view.

The measured strain rates for each of the high temperature simulations (≥600 K) are plotted against the applied tensile stress and labeled according to the temperature of the simulation in Figure 5.8. While it is obvious that there are some very clear trends in the data, not all the simulations at low stress reached a convincing steady state, even after extended runs. In Figure 5.8, we therefore collect the most recently measured strain rate for each of these simulations, and include arrows indicating an expected shift to higher strain rates for simulations that did not reach a convincing steady-state condition.

For high temperature experimental tests of a metallic glass, the steady-state data is frequently fitted and described using the classic one-dimensional model given in Equation 1.2, but which has been adapted here for uniaxial test conditions [7]. This model is given as

$$\dot{\varepsilon} = \gamma_o \cdot \nu_o \exp\left(-\frac{\Delta F}{kT}\right) \cdot \sinh\left(\frac{\sigma \cdot \gamma_o \Omega_o}{2\sqrt{3}kT}\right) \tag{5.9}$$

and predicts the uniaxial steady-state strain rate, $\dot{\varepsilon}$, for a sample under a uniaxial stress, σ. As seen in Figure 5.8, the strain rates measured from the simulations are faster than that predicted by Equation 5.9 at lower stress but then begin to match the prediction at higher stress.

The 2D rheology, discussed in section 2.3.2, matched the constitutive law quite well, and it is therefore somewhat surprising that the 3D simulations do not match the predicted behavior over the entire range of stresses and temperatures shown in Figure 5.8. However, the STZ activations for the 2D simulations were shown to be independent of one another in section 3.3, as expected by the constitutive law. An analysis of the STZ correlations in the 3D simulations shows a trend of nearest-neighbor correlated STZ activity, even in the simulation at 800 K and 300 MPa, which deformed homogeneously. As such, it is not surprising that the measured strain rates for the 3D simulations are faster than that predicted by Equation 5.9. When STZs activate in a more localized fashion, the increased stress from previous activations in the surrounding neighborhood raises the rate for subsequent local STZ activations. This leads to faster overall strain rates than purely independent STZ activations. However, the rate increase from correlated STZ activity is reduced at higher stress because the higher externally imposed stress diminishes the effect from neighboring STZ activity, thereby allowing the measured strain rates to more closely match the predicted rate. It is expected that the correlated STZ activity under these circumstances is due partially to the values used for the intrinsic barrier height, ΔF, and STZ volume, Ω_o. In the 3D simulations the value for ΔF is lowered by about 30% and the value for Ω_o is larger 25%, when compared with the values used in the 2D simulations. The change in ΔF and Ω_o have the combined effect of increasing the STZ activation rate for a given stress when using the 3D values as compared with the 2D values. Therefore, these changed parameters are likely contribute to the deviation of the measured strain rates in the 3D simulations from the expected constitutive law.

As noted above, some of the low stress simulations never reached a steady flow state, or only did so after an exhaustive number of STZ activations. This is due to the fact that the system cannot easily accommodate the large increase in energy from a single STZ activation at low stresses, so subsequent activations are required to relax the system locally. This means that the simulations spend a lot of time trying to accommodate a local increment of strain through many STZ activations. Similar behavior was observed in the 2D simulations discussed in chapters 2 and 3

and this behavior may indicate that, under these conditions, a smaller increment of strain for the STZ activation may be more appropriate. Practically, a material would most likely find the new lower energy state, associated with a small increment of strain, without having to pass through several high energy equilibrium states first, as these simulations are doing.

5.3.2. Low temperature model response

The representative low temperature response of the modeling framework at high stresses (≥ 1GPa) is presented in Figure 5.9 for a simulation at 300 K and 3 GPa. Under these conditions, a metallic glass is expected to exhibit little to no plasticity prior to the rapid emergence of a shear band and subsequent failure of the sample along the shear plane [100]. In Figure 5.9, the expected response of the system is captured reasonably well. The strain-time data in Figure

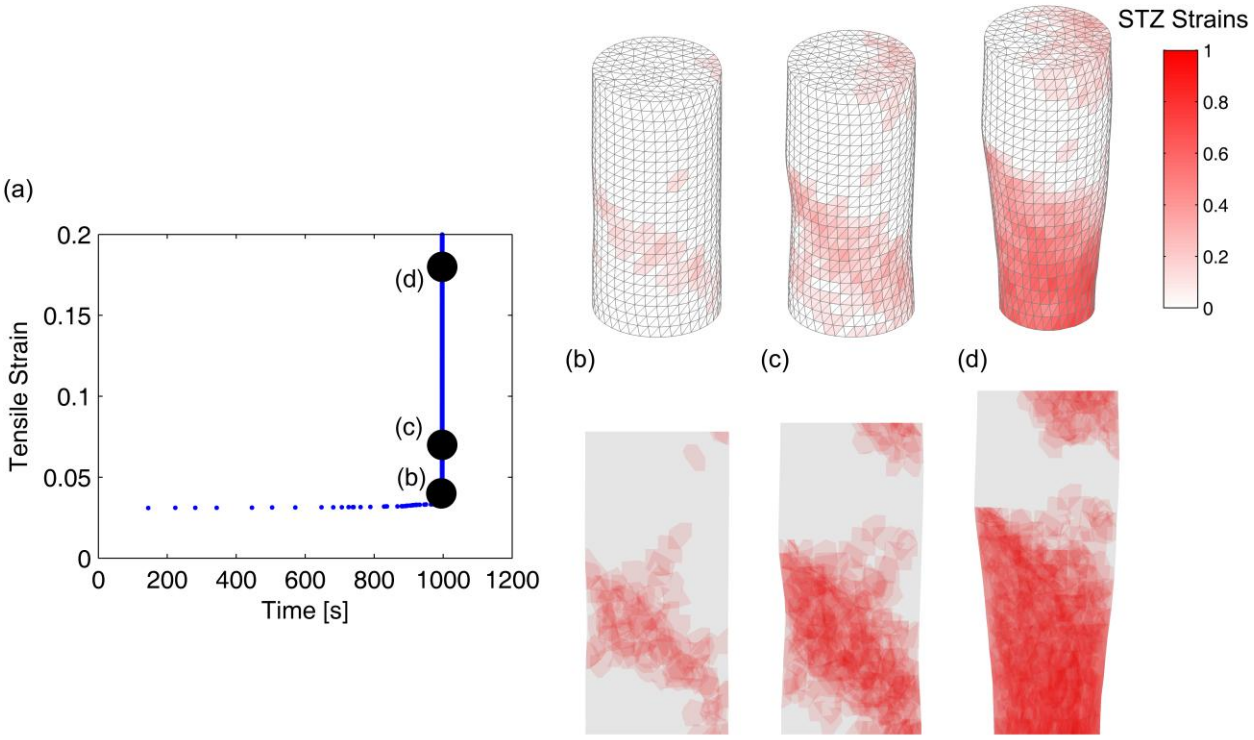

Figure 5.9 Representative low temperature model response

The data shown is for a simulation under a constant tensile stress of 3 GPa at 300 K. (a) Strain-time evolution during the course of the simulation showing the abrupt and nearly instant accumulation of strain. Snapshots of the system at strains of 4, 7 and 18 % are provided in (b), (c) and (d), respectively. The upper row of snapshots gives a perspective view of the outside of the simulation cell with the plastic STZ strains shaded according to the legend. The lower row of snapshots provides a semi-transparent profile view of the cell for viewing through the thickness.

5.9(a) shows that very little STZ activity occurs over a long period of time while a nucleation site for the shear band is developed. Then in the region between Figure 5.9(b), 4% strain, and Figure 5.9(c), 7% strain, the system concentrates nearly all the STZ activity in further developing and thickening the shear band. And interestingly enough, it can be seen in the transparent snapshots of Figure 5.9(b) and Figure 5.9(c) that the system made a failed attempt to initiate a shear band in a plane perpendicular to the propagating shear band through localized STZ activity. Finally, the system rapidly accumulates over 18% strain, shown in Figure 5.9(d), from 7% strain in less than 0.13 seconds. The localization illustrated in Figure 5.9(b) and Figure 5.9(c) pertains to what is expected for the propagation of a shear band and strains in the band exceed 25%.

Figure 5.9(d) illustrates severe necking occurring after the shear band has formed and propagated, which is not expected. In experimental settings, tensile fracture would occur at this point, and in the present case we believe the necking is an artifact due in large part to the boundary conditions of the simulations; eventual slip along the band is restricted by the imposed boundary conditions which only allow radial movement of the nodes on the top and bottom surfaces. The combination of the slip and the boundary conditions leads to unphysical stress concentrations there and thus to the development of an unphysical strain distribution in the form of a neck. This situation is exacerbated in Figure 5.9(d) where the shear band impinges on the bottom surface.

At low temperatures and low stresses (< 1GPa) the simulations actually accumulate very little plastic strain during the course of the simulations; in most cases, much less than 1%. Detailed analysis of these simulations shows the emergence and disappearance of pockets of strain during the course of the simulation. Furthermore, a long time increment is typically seen before a given STZ activation, and then in the next step, the same STZ is nearly instantly and completely reversed, allowing little accumulation of plastic strain. This type of behavior was observed in the 2D simulations in chapters 2 and 3 and was associated with the elastic response of the material because there is so little motivation for the system to evolve, no matter what time scales are involved.

5.3.3. Deformation Map

The insight gained into the general response of the STZ Dynamics framework can be represented well by building a deformation map to capture the important features of the results discussed

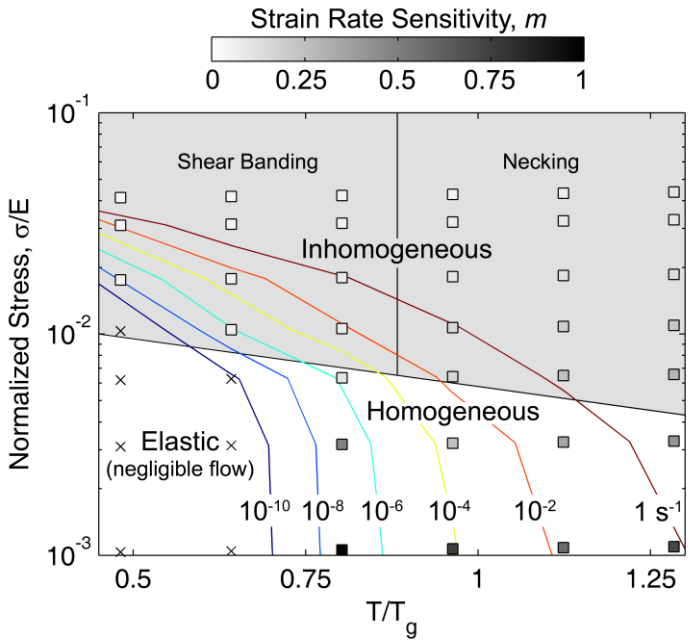

Figure 5.10 Three-dimensional STZ Dynamics deformation map

The deformation map is created from results of tensile creep simulations of a model metallic glass conducted over a range of stresses and temperatures. The colored lines represent contours of steady-state strain rates; simulations with measured rates less than 10^{-10} s^{-1} are deemed as exhibiting negligible flow and identified with the elastic material response. The remaining simulations are marked with squares and shaded with their respective values of the strain rate sensitivity, m, as given in the legend above the map. Shading distinguishes the simulations deemed as homogeneous and inhomogeneous, which is further divided into the samples which exhibited shear banding and necking.

above for testing over a wide range of conditions. This deformation map is provided in Figure 5.10 where the tensile stress is normalized by Young's modulus and the temperature is normalized by the glass transition temperature of Vitreloy 1, T_g = 623 K [22]. The characteristics of the general response captured in this map include: regions to delimit the different macroscopic modes of deformation observed in the simulations, contours of constant strain rate to gauge the timescales involved and values of the strain rate sensitivity to gauge the stability of flow.

The contours of constant strain rate range from 10^{-10} to 1 s^{-1} and simulations with a measured strain rate less than 10^{-10} s^{-1} are said to exhibit negligible flow and lie within the elastic regime. Simulations associated with the elastic response of the material are marked with an 'x' while all other simulations are marked with a square.

The strain rate sensitivity defined in Equation 2.18, and measured from the data in Figure 5.8, is presented by shading the interior of the squares identifying each simulation. The color bar above the deformation map provides the values of the strain rate sensitivity associated with the shading in each square.

Finally, the different regions of the observed macroscopic deformation are clearly delineated. Those samples which deformed in an inhomogeneous manner are clearly marked on the map and are further distinguished between shear localization, in the form of shear banding, and necking. In general, the features of the deformation map match well with what is expected of a metallic glass [7]. This provides confidence that this modeling framework will be able to present a detailed view of the microscopic nature of deformation in a metallic glass on experimentally relevant time and length scales.

5.4. Detailed investigation of shear localization

In an effort to better understand the nature of shear localization in a metallic glass we present here a detailed analysis of localization observed through the STZ Dynamics framework. However, prior to analyzing and discussing these results, we review the current understanding of this phenomenon as presented in the literature.

First of all, we look at the results from modeling of shear localization, with a particular emphasis on atomistic simulations. In early athermal quasistatic simulations, Srolovitz et al. suggested that stress concentrations incite localization [27] although more recent work disputes this [42, 91] and Tsamados et al. suggest that further description of the local state is required to identify instabilities. Maloney and Lemaitre suggest that the onset of an irreversible plastic event is associated with the divergence of the elastic constants [43]. Furthermore, this critical mode is a collective property of the system and not a local quantity, although it can be associated with the motion of a specific cluster of atoms at the onset of plasticity [42]. Once the onset of plasticity has been initiated, two types of events are observed: local STZ-like quadrupolar motions with large displacements and cascade-like displacements which are smaller in magnitude and which span the simulation cell [41, 42]. Finally, these events, whether in a single cascade or in correlated succession of individual events, lead to macroscopically observable deformation [42, 58, 65, 75]. Shi and Falk go on to suggest that localization may be along a percolating path of short range order and detail the breakdown of local short range order in the region of localized

deformation [58]. Therefore, the structure resulting from varied processing of the glass can have a large effect on the nature of localization [55, 58, 59].

In experimental attempts to measure shear localization, a number of approaches have been used. From high speed cinematography [5, 101], to infrared cameras used to measure the heat release of shear bands [102, 103] and even using high-sensitivity strain gauges [104]. In all these cases, the results are analyzed when the sample is deforming in the steady state such that data can be captured from a number of individual serrations in the stress-strain curve. From these experiments, a great deal has been learned about the nature of the serrated flow and a number of estimates have been made for the minimum velocity of shear bands in the steady state.

Thus, we can see that the atomistic simulations provide a great deal of detail about the process of shear banding, but cannot capture this detail on experimentally relevant scales. The experimental techniques actually capture real glass behavior, but the temporal and spatial limitations of the data acquisition frustrate the ability to provide a detailed study of the nucleation and propagation of individual shear bands. As such, the STZ Dynamics framework is an attractive method to study this behavior because of its ability to capture the microscopic behavior on scales which are experimentally relevant.

We study the nucleation and propagation of a shear band during a tensile creep test of a simulation cell with a diameter of 20 nm and a height of 60 nm, under a constant tensile stress of 1.7 GPa and a temperature of 300 K. The boundary conditions for this simulation are identical to those employed for smaller simulation cells presented in section 5.3. Snapshots of the evolution of the model through the course of the simulation are shown in Figure 5.11 where we present only the semi-transparent profile and top views of the cell, which are labeled by the accumulated plastic strain and the number of STZ activations in the simulation up to that point.

As can be seen by the first snapshot after 50 STZ activations, STZs are activated throughout the simulation cell giving little indication as to where localization may initiate. However, in the next two snapshots, after 150 and 200 STZ activations, three regions, labeled ‘a’, ‘b’ and ‘c’, begin to show increased local STZ activity. After 250 STZ activations, it can be seen that the region labeled as ‘b’ in the previous snapshot shows the beginnings of localization along a plane propagating nearly halfway through the width of the simulation cell. This region continues to propagate with little to no STZ activity occurring outside this region, as can be seen in the

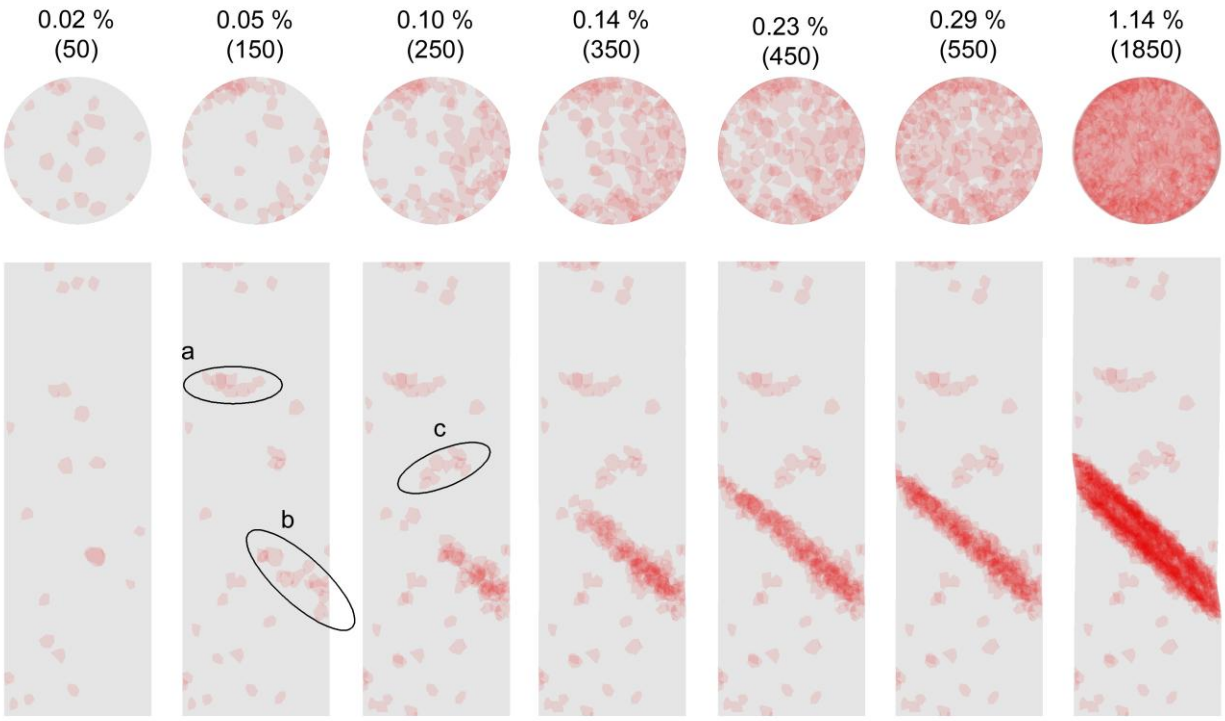

Figure 5.11 Detailed visualization of shear localization

The snapshots of shear localization are shown in semi-transparent images of the plastic (STZ) strains. The accumulated plastic strain is given as a percent above each snapshot, with the number of STZ activations in the simulation up to that point listed in parentheses. Specific regions of STZ activity are encircled and labeled as 'a', 'b' and 'c' for discussion in the text.

snapshot after 350 STZ activations. By the time 450 STZs have been activated, the region of localized shear has propagated across the entire simulation cell, although it can be seen in the top view of the 450 STZ activation snapshot, that the STZ activity does not provide complete coverage of the localized shear plane. With all subsequent STZ activity concentrated along the shear plane, the band thickens and provides uniform coverage across the plane, as can be seen in the snapshot after 550 STZ activations. In subsequent steps the band continues to thicken and the resulting deformation can be seen in the snapshot after 1850 STZ activations, where the simulation was terminated after over 5000 CPU-hours.

The onset of plasticity for these simulations is, of course, the activation of an STZ, whose only bias for activation is the local stress state. However, under these conditions singular STZ activation is insufficient to nucleate any significant shear localization. Rather, a region must incubate and collect sufficient plasticity through STZ activity such that future activations are

biased to be in the immediate surroundings. In the case of these simulations, the incubation sites of localized STZ activity are all on the free surfaces, where they can be accommodated with a reduced energy penalty.

It is not until we see the advancing front of shear localization from one of these sites at the free surface that we can claim nucleation of a shear band. Once the shear band nucleates however, it leads to auto-catalytic activation of STZs for the propagation and thickening of the shear band. While the advancing shear band front is dominated by STZs, a single layer thick, not all STZ activity is focused on advancing the front. Rather, the shear band makes a small advance in a certain region, and then follows up by thickening that region as well as thickening the band behind the front. Thus, the region following the front is thicker and more developed, until the shear localization spans the simulation cell. At this point STZ activity is distributed throughout the band to allow it to thicken and carry more shear, leading to macroscopic slip.

Discussing these results in the context of what is observed in the atomistic simulations, the model does not, at present, attempt to find transitions other than the standard increment of strain for all possible transition states and the model does not account for any description of the state beyond the local stress. As atomistics suggest the importance of these, it is possible to adapt the model accordingly, however, it is desirable that these details be better resolved in atomistic simulations prior to their implementation in this framework. Also, without a state variable to describe the local structure, we cannot comment on the structural dependence of a shear band path. From these simulations we can confirm, however, that the nucleation of a shear band is impossible to identify until is already propagating. And, the propagation of a shear band is not instantaneous; it has an advancing front which precedes the more developed portion of the shear band.

5.5. Simulated nanoindentation

As a demonstration of the flexibility of the STZ Dynamics modeling framework, we examine the simulated response of a model glass to nanoindentation. This simulation examines a cylindrical sample with a diameter of 30 nm and height of 11 nm using a spherical indenter with a radius of 12 nm, tested at a temperature of 300 K. Frictionless hard contact is assumed between the indenter and the surface of the simulation cell and indentation is carried out at a constant displacement rate of 1 nm/s. The nodes on the bottom and sides of the cylinder are fixed in all

three spatial coordinates, allowing only the top surface to move freely. The KMC algorithm is adapted slightly for the simulated nanoindentation on account of the large variation in the applied stresses, leading to large variations in the elapsed time for any given step. Therefore, to ensure that the algorithm only considers events on relevant timescales, a maximum time increment of 5 ms is imposed for each KMC step. Therefore, in a given step, an STZ activation with a time increment less than the maximum allowed time increment is accepted; otherwise, the STZ activation is suppressed for that step and the system time is incremented by the maximum allowed. In either case, the indenter displacement is advanced by the appropriate amount and the KMC algorithm is repeated.

The model response to the simulated nanoindentation is plotted in Figure 5.12 where the graph in the figure shows the load-displacement curve for the indentation, with three snapshots of the system identified by (b), (c) and (d). The snapshots show the semi-transparent view of the model as seen from the side, in the upper row of snapshots, and from above, in the lower row of snapshots. These snapshots also include the surface of the indenter in the side view and the contact periphery in the top view. The snapshot shown in Figure 5.12(b) shows the resulting strains in the system following the first significant load drop. As can be seen in the figure, the principal STZ activity is located at the surface contacting the indenter, however this activity does occur at the location of the maximum shear stress, which is at a depth of half the contact radius for Hertzian contact. Subsequent STZ activity continues to concentrate near the sample surface as the indenter is pushed deeper into the sample, as shown in Figure 5.12(c) and Figure 5.12(d).

Discrete bursts of correlated STZ activity are observed in the simulations, leading to load drops in the load-displacement curve, expected for a displacement controlled indentation test. However, each of these correlated bursts only involve a small number of STZ activations, illustrated by the small magnitude of the load drops, and is therefore insufficient to be associated with any significant shear localization.

The abundance of STZ activity located at the sample surface is not surprising considering the small indenter radius, and corresponding contact radius. Experimental nanoindentation is frequently carried out with tip radii >100 nm, pushing the STZ activity much deeper into the sample, allowing for individual shear band activity to be identified [93, 105]. In fact, Packard et al. developed a slip-line theory for a shear band path in indentation that suggests shear bands

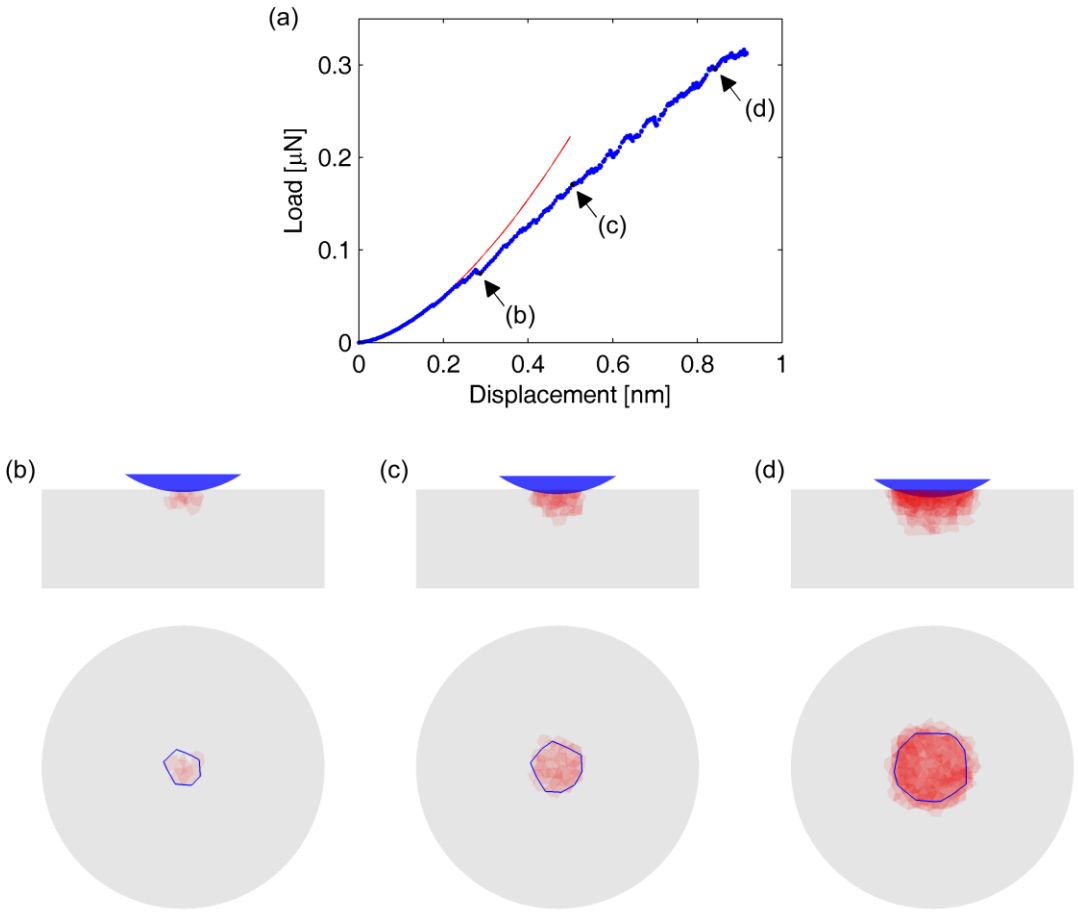

Figure 5.12 Three-dimensional simulated nanoindentation of a model glass
The simulated nanoindentation is carried out at 300 K. The load-displacement curve is provided in (a) with the model response given by the data points. The purely elastic reference curve is also plotted, providing easier identification of the deviation from elasticity. Snapshots showing the semi-transparent view of the plasticity of the system at specific intervals are provided in (b), (c) and (d), at the intervals labeled in (a). The upper row of snapshots shows the side view of the model along with a surface representing the indenter. The lower row of snapshots shows the top view of the model, with the contact area outlined.

may develop below the area of maximum shear [93]. Corroborating this theory, are results from simulated nanoindentation results from atomistics where the shear band passes below, and not through, the area of maximum shear [53].

The simulated nanoindentation carried out in chapter 4 employed a larger tip radius of 40 nm and exhibited clearer slip lines of STZ activity, resulting from the 40 nm tip radius. The success of the 2D work in chapter 4 indicates that a larger radius, and a correspondingly larger

simulation cell, may be all that is required to observe STZ activity more characteristic with that observed experimentally. At present, the current computational capabilities available to the authors are insufficient for the requirements of a significantly larger simulation cell.

5.6. Conclusions

The STZ Dynamics modeling framework, which has proved to be a powerful tool for investigating the mechanical behavior of metallic glasses, has been extended to three dimensions. The framework coarse-grains a model glass into shear transformation zones and considers the stress-biased thermal activation of these zones through the kinetic Monte Carlo algorithm. The derivation of the activation rate for shearing an STZ in three dimensions has been presented alongside a method for coarse-graining the STZs on a finite element mesh.

Salient results from tensile creep tests of the framework over a range of stresses and temperatures include the expected high temperature steady-state accumulation of strain, rheological flow data which conform to the trends of the classic constitutive model for metallic glasses and shear localization evident in the form of a nascent shear band at low temperature followed by an unexpected necking due to boundary conditions. The results from numerous simulations have been used to construct a deformation map for the model response which generally aligns with a deformation map created from experimental testing of a metallic glass.

The utility of the method is demonstrated in two additional applications of modeling framework. First, detailed investigation of shear localization reveals the elusive nature of the nucleation of a shear band and confirms the auto-catalytic and progressive propagation of a shear band. Second, simulated nanoindentation carried out in three dimensions shows STZ activity occurring in the region of maximum shear, although the limited simulation size precludes comparison to experimental results.

6. Closing remarks

The effort to model the mechanical behavior of amorphous metals by various techniques have provided a wealth of information about the microscopic and macroscopic nature of deformation. However, the inability to model certain phenomenon on the appropriate time and length scales has left some very important and puzzling questions regarding the true nature of deformation in these metals. This thesis has focused on the development of a meso-scale model capable of resolving the microscopic nature of deformation in a metallic glass while preserving the efficiency to model the behavior on experimentally relevant conditions. The major results and implications are summarized below.

6.1. Development and validation of STZ Dynamics framework

The new meso-scale modeling technique for the thermo-mechanical behavior of metallic glasses considers the shear transformation zone (STZ) as the fundamental unit of deformation, and coarse-grains an amorphous collection of atoms into an ensemble of STZs on a mesh. By employing finite element analysis and a kinetic Monte Carlo algorithm, the modeling technique is capable of simulating glass processing and deformation on time and length scales greater than those usually attainable by atomistic modeling. The description of framework is presented, along with a specific two-dimensional implementation for a model metallic glass. The model is shown to capture the basic behaviors of metallic glasses, including high-temperature homogeneous flow following the expected constitutive law, and low-temperature strain localization into shear bands. Details of the effects of processing and thermal history on the glass structure and properties are also discussed.

Implication for future work: Given that this framework can capture the basic behavior of a metallic glass on experimentally relevant scales while preserving the fundamental nature of deformation, the technique can now be used to investigate specific phenomena of metallic glasses. Furthermore, the use of FEA in the framework presents possibilities to investigate important phenomena, such as the redistribution of free volume, by tracking state variables, volume, or the effect of adiabatic shear banding, by solving the heat flow from STZ activity.

6.2. Activated States and Correlated STZ Activity

Insight into the collective aspects of the microscopic events underlying deformation in a model metallic glass is studied by analyzing the activated states of STZs in such a model, as well as the

statistics of their activation and how these are affected by imposed conditions of stress and temperature. The analysis sheds light on the spatial and temporal correlations between the individual STZ activations that lead to different macroscopic modes of deformation. Three basic STZ correlation behaviors are observed: uncorrelated activity, nearest-neighbor correlation, and self-reactivating STZs. These three behaviors correspond well with the macroscopic deformation modes of homogeneous flow, inhomogeneous deformation, and elastic behavior, respectively. The effect of pre-existing stresses in the simulation cell is also studied and found to have a homogenizing effect on STZ correlations, suppressing the tendency for localization.

Implication for future work: Experimentally observed behaviors in metallic glasses often lack a detailed picture of the microscopic activity, however, the qualitative and quantitative correlations detailed by this work may prove useful in the future discussions of these phenomena. Furthermore, the tools developed to investigate these behaviors are designed for general statistical analysis of discrete microscopic activity.

6.3. Insight into Nanoscale Cyclic Strengthening of Metallic Glasses

The application of the STZ Dynamics framework to simulated nanoindentation provides insight into the microscopic mechanisms which lead to the experimentally observed nanoscale strengthening under cyclic contact in the elastic regime. The simulations expose the local STZ operations that occur beneath an indenter during cycling and reveal a plausible mechanism for the observed cyclic hardening: local regions of confined microplasticity can develop progressively over several cycles, without being detectable in the global load-displacement response. It is inferred that significant structural change must attend such microplasticity, leading to hardening of the glass.

Implication for future work: The success of the model's ability to investigate specific and unexplained phenomena in a metallic glass bodes well future applications of the framework. Also, as the results from this work confirm the plausibility of the micro-plasticity mechanism leading to hardening, the extension of the model to account for structural relaxation will be invaluable in further establishing this mechanism and the exact nature of the nanoscale hardening in a metallic glass.

6.4. Development and validation of 3D STZ Dynamics Framework

The extension of the modeling framework to three dimensions builds largely upon the 2D STZ Dynamics framework but requires a 3D coarse-grained ensemble of STZs as well as an adapted derivation of the STZ activation rate which allows an STZ to shear in 3D. The description of the updated framework is provided along with validation of the model over a wide range of conditions. The 3D model captures the same general expected behaviors of a metallic glass observed with the 2D model, while also examining the stability of flow at high temperatures. Additionally, the 3D framework is used to perform a detailed investigation of shear localization as well as preliminary examination of the contact testing capabilities.

Implication for future work: The ability of the framework to now account for multi-axial stress states and complex test conditions on the appropriate time and length-scales opens up a wealth of possibilities for study in a metallic glass. In fact, the flexibility of the framework and the level of detail gained from examination of shear localization have inspired new tests, to be completed by the author, to study shear localization under constant strain rate, where the system can identify the yield stress and the corresponding time-scales for localization.

Acknowledgements

I want to acknowledge the magnificent support and guidance of my advisor, Professor Christopher Schuh, for his constant encouragement, suggestions and patience as I worked through this thesis. His support is second only to that of my wife, Sarah, and my twins, Will and Lily, who not only bring me the greatest happiness but the balance and life I love.

I gratefully acknowledge financial support from the Office of Naval Research and from the Department of Defense through the National Defense Science and Engineering Graduate Fellowship program. Both of these sources of funding have provided confidence and freedom in concentrating on the research contained in this thesis.

I am thankful for the opportunity to collaborate with David Rodney on the work contained in chapter 3 of this thesis, as well as the opportunity to collaborate with Corinne E. Packard and Nasser Al-Aqeeli on the work contained in chapter 4. The assistance of Jeremy K. Mason and Srikanth Patala in the derivation of the STZ activation rates in two and three dimensions, respectively, is gratefully acknowledged.

Finally, I wish a thank you to the many past and present members of the Schuh Research Group with whom I have discussed and analyzed this thesis research and for their friendship, which has made my time at MIT an enjoyable experience.

References

[1] Klement W, Willens R, Duwez P. *Non-crystalline structure in solidified gold-silicon alloys.* Nature 1960;187:869.

[2] Egami T. *Universal criterion for metallic glass formation.* Mater. Sci. Eng. A 1997;226:261.

[3] Egami T, Waseda Y. *Atomic Size Effect on the Formability of Metallic Glasses.* J. Non-Cryst. Solids 1984;64:113.

[4] Telford M. *The case for Bulk Metallic Glass.* Mater. Today 2004;7:36.

[5] Neuhauser H. *Rate of Shear Band Formation in Metallic Glasses.* Scr. Metall. 1978;12:471.

[6] Argon AS. *Mechanisms of Inelastic Deformation in Metallic Glasses.* J. Phys. Chem. Solids 1982;43:945.

[7] Schuh CA, Hufnagel TC, Ramamurty U. *Mechanical behavior of amorphous alloys.* Acta Mater. 2007;55:4067.

[8] Barrat JL, de Pablo JJ. *Modeling deformation and flow of disordered materials.* MRS Bull. 2007;32:941.

[9] Argon AS. *Plastic-Deformation in Metallic Glasses.* Acta Metall. 1979;27:47.

[10] Spaepen F. *Microscopic Mechanism for Steady-State Inhomogeneous Flow in Metallic Glasses.* Acta Metall. 1977;25:407.

[11] Argon AS, Kuo HY. *Plastic-Flow in a Disordered Bubble Raft (an Analog of a Metallic Glass).* Mater. Sci. Eng. 1979;39:101.

[12] Argon AS, Shi LT. *Development of Visco-Plastic Deformation in Metallic Glasses.* Acta Metall. 1983;31:499.

[13] Bulatov VV, Argon AS. *A Stochastic-Model for Continuum Elastoplastic Behavior .1. Numerical Approach and Strain Localization.* Model. Simul. Mater. Sci. Eng. 1994;2:167.

[14] Bulatov VV, Argon AS. *A Stochastic-Model for Continuum Elastoplastic Behavior .2. a Study of the Glass-Transition and Structural Relaxation.* Model. Simul. Mater. Sci. Eng. 1994;2:185.

[15] Bulatov VV, Argon AS. *A Stochastic-Model for Continuum Elastoplastic Behavior .3. Plasticity in Ordered Versus Disordered Solids.* Model. Simul. Mater. Sci. Eng. 1994;2:203.

[16] Fu XL, Li Y, Schuh CA. *Homogeneous flow of bulk metallic glass composites with a high volume fraction of reinforcement.* J. Mater. Res. 2007;22:1564.

[17] Zink M, Samwer K, Johnson WL, Mayr SG. *Plastic deformation of metallic glasses: Size of shear transformation zones from molecular dynamics simulations.* Phys. Rev. B 2006;73:172203.

[18] Eshelby JD. *The Determination of the Elastic Field of an Ellipsoidal Inclusion, and Related Problems.* Proc. R. Soc. Lond. A 1957;241:376.

[19] Turnbull D, Cohen M. *Free-Volume Model of the Amorphous Phase: Glass Transition.* J. Chem. Phys. 1961;34:120.

[20] Turnbull D, Cohen M. *On the Free-Volume Model of the Liquid-Glass Transition.* J. Chem. Phys. 1970;52:3038.

[21] Falk ML, Langer JS. *Dynamics of viscoplastic deformation in amorphous solids.* Phys. Rev. E 1998;57:7192.

[22] Lu J, Ravichandran G, Johnson WL. *Deformation behavior of the $Zr_{41.2}Ti_{13.8}Cu_{12.5}Ni_{10}Be_{22.5}$ bulk metallic glass over a wide range of strain-rates and temperatures.* Acta Mater. 2003;51:3429.
[23] Donovan PE, Stobbs WM. *The Structure of Shear Bands in Metallic Glasses.* Acta Metall. 1981;29:1419.
[24] Pekarskaya E, Kim CP, Johnson WL. *In situ transmission electron microscopy studies of shear bands in a bulk metallic glass based composite.* J. Mater. Res. 2001;16:2513.
[25] Conner RD, Li Y, Nix WD, Johnson WL. *Shear band spacing under bending of Zr-based metallic glass plates.* Acta Mater. 2004;52:2429.
[26] Conner RD, Johnson WL, Paton NE, Nix WD. *Shear bands and cracking of metallic glass plates in bending.* J. Appl. Phys. 2003;94:904.
[27] Srolovitz D, Vitek V, Egami T. *An Atomistic Study of Deformation of Amorphous Metals.* Acta Metall. 1983;31:335.
[28] Schuh CA, Nieh TG. *A survey of instrumented indentation studies on metallic glasses.* J. Mater. Res. 2004;19:46.
[29] Hufnagel TC, Jiao T, Li Y, Xing LQ, Ramesh KT. *Deformation and failure of $Zr_{57}Ti_5CU_{20}Ni_8Al_{10}$ bulk metallic glass under quasi-static and dynamic compression.* J. Mater. Res. 2002;17:1441.
[30] Lewandowski JJ, Greer AL. *Temperature rise at shear bands in metallic glasses.* Nat. Mater. 2006;5:15.
[31] Schuh CA, Lund AC, Nieh TG. *New regime of homogeneous flow in the deformation map of metallic glasses: elevated temperature nanoindentation experiments and mechanistic modeling.* Acta Mater. 2004;52:5879.
[32] Schuh CA, Lund AC. *Atomistic basis for the plastic yield criterion of metallic glass.* Nat. Mater. 2003;2:449.
[33] Donovan PE. *Compressive Deformation of Amorphous Pd40ni40p20.* Mater. Sci. Eng. 1988;98:487.
[34] Delhommelle J. *Simulations of shear-induced melting in two dimensions.* Phys. Rev. B 2004;69:144117.
[35] Yang B, Morrison ML, Liaw PK, Buchanan RA, Wang GY, Liu CT, Denda M. *Dynamic evolution of nanoscale shear bands in a bulk-metallic glass.* Appl. Phys. Lett. 2005;86:141904.
[36] Packard CE, Witmer LM, Schuh CA. *Hardening of a metallic glass during cyclic loading in the elastic range.* Appl. Phys. Lett. 2008;92:171911.
[37] Argon AS, Shi LT. *Analysis of Plastic-Flow in an Amorphous Soap Bubble Raft by the Use of an Inter-Bubble Potential.* Philos. Mag. A 1982;46:275.
[38] Deng D, Argon AS, Yip S. *Simulation of Plastic-Deformation in a 2-Dimensional Atomic Glass by Molecular-Dynamics .4.* Philos. Trans. R. Soc. Lond. A 1989;329:613.
[39] Shi YF, Falk ML. *Structural transformation and localization during simulated nanoindentation of a noncrystalline metal film.* Appl. Phys. Lett. 2005;86:011914.
[40] Rottler J, Robbins MO. *Shear yielding of amorphous glassy solids: Effect of temperature and strain rate.* Phys. Rev. E 2003;68:011507.
[41] Tanguy A, Leonforte F, Barrat JL. *Plastic response of a 2D Lennard-Jones amorphous solid: Detailed analysis of the local rearrangements at very slow strain rate.* Eur. Phys. J. E 2006;20:355.

[42] Maloney CE, Lemaitre A. *Amorphous systems in athermal, quasistatic shear.* Phys. Rev. E 2006;74:016118.
[43] Maloney C, Lemaitre A. *Universal breakdown of elasticity at the onset of material failure.* Phys. Rev. Lett. 2004;93:195501.
[44] Rodney D, Schuh C. *Distribution of Thermally Activated Plastic Events in a Flowing Glass.* Phys. Rev. Lett. 2009;102:235503.
[45] Deng D, Argon AS, Yip S. *A Molecular-Dynamics Model of Melting and Glass-Transition in an Idealized 2-Dimensional Material .1.* Philos. Trans. R. Soc. Lond. A 1989;329:549.
[46] Deng D, Argon AS, Yip S. *Topological Features of Structural Relaxations in a 2-Dimensional Model Atomic Glass .2.* Philos. Trans. R. Soc. Lond. A 1989;329:575.
[47] Deng D, Argon AS, Yip S. *Kinetics of Structural Relaxations in a 2-Dimensional Model Atomic Glass .3.* Philos. Trans. R. Soc. Lond. A 1989;329:595.
[48] Egami T, Srolovitz D. *Local Structural Fluctuations in Amorphous and Liquid-Metals - a Simple Theory of the Glass-Transition.* Journal of Physics F-Metal Physics 1982;12:2141.
[49] Srolovitz D, Maeda K, Vitek V, Egami T. *Structural Defects in Amorphous Solids Statistical-Analysis of a Computer-Model.* Philos. Mag. A 1981;44:847.
[50] Chen SP, Egami T, Vitek V. *Local Fluctuations and Ordering in Liquid and Amorphous Metals.* Phys. Rev. B 1988;37:2440.
[51] Vitek V, Egami T. *Atomic Level Stresses in Solids and Liquids.* Phys. Status Solidi B 1987;144:145.
[52] Langer JS. *Microstructural shear localization in plastic deformation of amorphous solids.* Phys. Rev. E 2001;64:011504.
[53] Shi YF, Falk ML. *Stress-induced structural transformation and shear banding during simulated nanoindentation of a metallic glass.* Acta Mater. 2007;55:4317.
[54] Bailey NP, Schiotz J, Jacobsen KW. *Atomistic simulation study of the shear-band deformation mechanism in Mg-Cu metallic glasses.* Phys. Rev. B 2006;73:064108.
[55] Shi YF, Falk ML. *Strain localization and percolation of stable structure in amorphous solids.* Phys. Rev. Lett. 2005;95:095502.
[56] Shi YF, Falk ML. *Atomic-scale simulations of strain localization in three-dimensional model amorphous solids.* Phys. Rev. B 2006;73:214201.
[57] Falk ML. *Molecular-dynamics study of ductile and brittle fracture in model noncrystalline solids.* Phys. Rev. B 1999;60:7062.
[58] Shi Y, Falk ML. *Does metallic glass have a backbone? The role of percolating short range order in strength and failure.* Scr. Mater. 2006;54:381.
[59] Albano F, Falk ML. *Shear softening and structure in a simulated three-dimensional binary glass.* J. Chem. Phys. 2005;122:8.
[60] Lund AC, Schuh CA. *Yield surface of a simulated metallic glass.* Acta Mater. 2003;51:5399.
[61] Su C, Anand L. *Plane strain indentation of a Zr-based metallic glass: Experiments and numerical simulation.* Acta Mater. 2006;54:179.
[62] Anand L, Su C. *A theory for amorphous viscoplastic materials undergoing finite deformations, with application to metallic glasses.* J. Mech. Phys. Solids 2005;53:1362.
[63] Anand L, Su C. *A constitutive theory for metallic glasses at high homologous temperatures.* Acta Mater. 2007;55:3735.

[64] Henann D, Anand L. *A constitutive theory for the mechanical response of amorphous metals at high temperatures spanning the glass transition temperature: Application to microscale thermoplastic forming.* Acta Mater. 2008;56:3290.
[65] Picard G, Ajdari A, Lequeux F, Bocquet L. *Slow flows of yield stress fluids: Complex spatiotemporal behavior within a simple elastoplastic model.* Phys. Rev. E 2005;71:010501.
[66] Lemaitre A. *Rearrangements and dilatancy for sheared dense materials.* Phys. Rev. Lett. 2002;89:195503.
[67] Pawellek R, Fahnle M. *Continuum Theory of Internal-Stresses in Amorphous Metals.* J. Phys.-Condes. Matter 1989;1:7257.
[68] Eastgate LO, Langer JS, Pechenik L. *Dynamics of large-scale plastic deformation and the necking instability in amorphous solids.* Phys. Rev. Lett. 2003;90:045506.
[69] Falk ML, Langer JS, Pechenik L. *Thermal effects in the shear-transformation-zone theory of amorphous plasticity: Comparisons to metallic glass data.* Phys. Rev. E 2004;70:011507.
[70] Bocquet L, Colin A, Ajdari A. *Kinetic Theory of Plastic Flow in Soft Glassy Materials.* Phys. Rev. Lett. 2009;103:036001.
[71] Jagla EA. *Strain localization driven by structural relaxation in sheared amorphous solids.* Phys. Rev. E 2007;76:046119.
[72] Thamburaja P, Ekambaram R. *Coupled thermo-mechanical modelling of bulk-metallic glasses: Theory, finite-element simulations and experimental verification.* J. Mech. Phys. Solids 2007;55:1236.
[73] Johnson WL, Demetriou MD, Harmon JS, Lind ML, Samwer K. *Rheology and ultrasonic properties of metallic glass-forming liquids: A potential energy landscape perspective.* MRS Bull. 2007;32:644.
[74] Demetriou MD, Harmon JS, Tao M, Duan G, Samwer K, Johnson WL. *Cooperative shear model for the rheology of glass-forming metallic liquids.* Phys. Rev. Lett. 2006;97:065502.
[75] Leonforte F, Boissiere R, Tanguy A, Wittmer JP, Barrat JL. *Continuum limit of amorphous elastic bodies. III. Three-dimensional systems.* Phys. Rev. B 2005;72:224206.
[76] Vaidyanathan R, Dao M, Ravichandran G, Suresh S. *Study of mechanical deformation in bulk metallic glass through instrumented indentation.* Acta Mater. 2001;49:3781.
[77] Homer ER, Schuh CA. *Mesoscale modeling of amorphous metals by shear transformation zone dynamics.* Acta Mater. 2009;57:2823.
[78] Voter A. Radiation Effects in Solids: Kinetic Monte Carlo. In: Sickafus KK, EA; Uberuaga, BP editor. Proceedings of the NATO Advanced Study Institute on Radiation Effects in Solids, vol. 235. Erice, Sicily, Italy: Springer Berlin 2004.
[79] Amar JG. *The Monte Carlo method in science and engineering.* Comput. Sci. Eng. 2006;8:9.
[80] Johnson WL, Samwer K. *A universal criterion for plastic yielding of metallic glasses with a* $(T/T_g)^{2/3}$ *temperature dependence.* Phys. Rev. Lett. 2005;95:195501.
[81] Wang Q, Pelletier JM, Blandin JJ, Suery M. *Mechanical properties over the glass transition of* $Zr_{41.2}Ti_{13.8}Cu_{12.5}Ni_{10}Be_{22.5}$ *bulk metallic glass.* J. Non-Cryst. Solids 2005;351:2224.
[82] Vitek V, Chen SP, Egami T. *Molecular-Dynamics Study of Atomic-Level Structural Parameters in Liquid and Amorphous Metals.* J. Non-Cryst. Solids 1984;61-2:583.

[83] Burke MA, Nix WD. *Plastic Instabilities in Tension Creep.* Acta Metall. 1975;23:793.
[84] Homer ER, Rodney D, Schuh CA. *Kinetic Monte Carlo study of activated states and correlated shear-transformation-zone activity during the deformation of an amorphous metal.* Phys. Rev. B 2010;81:064204.
[85] Lerner E, Procaccia I. *Locality and nonlocality in elastoplastic responses of amorphous solids.* Phys. Rev. E 2009;79:066109.
[86] Baret JC, Vandembroucq D, Roux S. *Extremal model for amorphous media plasticity.* Phys. Rev. Lett. 2002;89:195506.
[87] Tolman RC. The Principles of Statistical Mechanics. Oxford: Oxford University Press, 1938.
[88] Mura T. Micromechanics of defects in solids. Dordrecht: Nijhoff, 1987.
[89] Mukhopadhyay AB, Oligschleger C, Dolg M. *Molecular dynamics investigation of relaxations in zeolite ZSM-5 based amorphous material.* J. Phys. Chem. B 2004;108:16085.
[90] Fung YC, Tong P. Classical and Computational Solid Mechanics. Singapore: World Scientific, 2001.
[91] Tsamados M, Tanguy A, Leonforte F, Barrat JL. *On the study of local-stress rearrangements during quasi-static plastic shear of a model glass: Do local-stress components contain enough information?* Eur. Phys. J. E 2008;26:283.
[92] Packard CE, Homer ER, Al-Aqeeli N, Schuh CA. *Cyclic hardening of metallic glasses under Hertzian contacts: Experiments and STZ dynamics simulations.* Philos. Mag. 2010;90:1373
[93] Packard CE, Schuh CA. *Initiation of shear bands near a stress concentration in metallic glass.* Acta Mater. 2007;55:5348.
[94] Johnson KL. Contact mechanics. Cambridge: Cambridge University Press, 1985.
[95] Antoniou A, Bastawros A, Biner B. *Experimental observations of deformation behavior of bulk metallic glasses during wedge-like cylindrical indentation.* J. Mater. Res. 2007;22:514.
[96] Mason JK, Schuh CA. *Hyperspherical harmonics for the representation of crystallographic texture.* Acta Mater. 2008;56:6141.
[97] Frank FC. *Orientation Mapping.* Metall. Mater. Trans. A 1988;19:403.
[98] Morawiec A, Field DP. *Rodrigues parameterization for orientation and misorientation distributions.* Philos. Mag. A 1996;73:1113.
[99] Bruck HA, Christman T, Rosakis AJ, Johnson WL. *Quasi-Static Constitutive Behavior of* $Zr_{41.25}Ti_{13.75}Ni_{10}Cu_{12.5}Be_{22.5}$ *Bulk Amorphous-Alloys.* Scr. Metall. Mater. 1994;30:429.
[100] Mukai T, Nieh TG, Kawamura Y, Inoue A, Higashi K. *Dynamic response of a Pd40Ni40P20 bulk metallic glass in tension.* Scr. Mater. 2002;46:43.
[101] Song SX, Wang XL, Nieh TG. *Capturing shear band propagation in a Zr-based metallic glass using a high-speed camera.* Scr. Mater. 2010;62:847.
[102] Jiang WH, Fan GJ, Liu FX, Wang GY, Choo H, Liaw PK. *Spatiotemporally inhomogeneous plastic flow of a bulk-metallic glass.* Int. J. Plast. 2008;24:1.
[103] Jiang WH, Fan GJ, Liu FX, Wang GY, Choo H, Liaw PK. *Rate dependence of shear banding and serrated flows in a bulk metallic glass.* J. Mater. Res. 2006;21:2164.
[104] Chen HM, Huang JC, Song SX, Nieh TG, Jang JSC. *Flow serration and shear-band propagation in bulk metallic glasses.* Appl. Phys. Lett. 2009;94:141914.

[105] Moser B, Loffler JF, Michler J. *Discrete deformation in amorphous metals: an in situ SEM indentation study*. Philos. Mag. 2006;86:5715.